Technische Universität München

Fakultät für Elektrotechnik und Informationstechnik

Lehrstuhl fur Biologische Bildgebung

Image Reconstruction in Clinical Hybrid Optoacoustic and Ultrasound Imaging

Hong Yang

Vollstandiger Abdruck der von der Fakultät für Elektrotechnik und Informationstechnik der Technischen Universität München zur Erlangung des akademischen Grades eines Doktor-Ingenieurs genehmigten Dissertation.

Vorsitzender:	Prof. Dr.-Ing. Werner Hemmert
Prufer:	1. Prof. Dr. Vasilis Ntziachristos
	2. Prof. Dr.-Ing. Bernhard U. Seeber

Die Dissertation wurde am 04.05.2020 bei der Technischen Universität München eingereicht und durch die Fakultät für Elektrotechnik und Informationstechnik am 17.06.2021 angenommen.

Abstract

Multispectral optoacoustic tomography (MSOT), also termed spectroscopic photoacoustic tomography, enables high resolution imaging through the visualization of absorbing molecular absorbers deep within tissue. It emerges as a non-ionizing, non-invasive, label-free biomedical imaging technique that combines exquisite optical contrast of molecules with low scattering of ultrasound waves (not limited by optical diffusion) thus promising superior resolution/imaging depth over conventional methods for accurate diagnostics and assessment of diseases. In contrast to conventional optical methods, optoacoustic imaging utilizes the scattered photons, detects the consequential ultrasound wave generation due to optical absorption by biological tissue, and therefore provides high resolution and optical visualization across a wider range of depths, from a few hundred micrometers to several centimeter. Being able to provide valuable functional information by spectroscopic identification of absorbing chromophores, MSOT has demonstrated its potentials in both preclinical and clinical studies with and without extrinsic contrast agents.

This dissertation aims to further improve the value of MSOT imaging, especially in clinical studies. As a steppingstone to justify and guide clinical MSOT research, the imaging chain of preclinical MSOT is studied and a synthetic data framework is developed for better experimental designs. Based on the understanding gained from preclinical MSOT, this dissertation extends the scope to clinical MSOT imaging. Due to the essential changes in hardware design (i.e. limited-view illumination and detection) to enable the portability of the scanner, clinical MSOT imaging put forward a lot of challenges for achieving good image quality and accuracy. As one of the major solutions, the hybrid MSOT and ultrasound imaging is the focus of this dissertation. In order to integrate the hybrid information provided by optoacoustic and ultrasound images, the image reconstruction for both modalities are studied and optimized. With each single modality working properly, the information unfolded in ultrasound

images are used as priors for optoacoustic reconstruction to improve the optoacoustic image quality. With the methods developed in this dissertation, more information is recovered in optoacoustic and ultrasound images, which facilitates the clinical studies and potentially increases the clinical value of MSOT imaging.

Zusammenfassung

Multispektrale optoakustische Tomographie (MSOT), auch spektroskopische photoakustische Tomographie genannt, ermöglicht die hoch aufgelöste Bildgebung von absorbierenden Molekülen im Gewebeinneren. MSOT ist eine nicht-ionisierende, nichtinvasive, kontrastmittelfreie biomedizinische Bildgebungstechnik, die optischen molekularen Kontrast mit streuungsarmen Ultraschall (nicht limitiert durch optische Streuung) kombiniert. Diese Kombination erlaubt eine verbesserte Auflösung und Bildeindringtiefe im Vergleich zu konventionellen Methoden, z.B. um medizinische Diagnosen zu erstellen oder Krankheiten zu erkennen. Im Gegenteil zu klassischen optischen Methoden beruht das Prinzip der optoakustischen Bildgebung auf gestreuten Photonen, wobei es die im Gewebe durch optische Absorption generierten akustische Wellen auflöst. Diesbezüglich erlaubt diese Technik eine hochauflösende optische Darstellung in verschiedenen Tiefenbereichen, die von ein paar hundertstel Mikrometer bis zu mehreren Zentimetern reichen. Durch die Identifikation von Chromophoren mittels ihrer Absorptionspektren zeigt MSOT großes Potential für präklinische und klinische Studien mit oder ohne zusätzliche Kontrastmittel.

Diese Dissertation will die Qualität der Bildgebung mittels MSOT verbessern, besonders im Rahmen klinischer Studien. Als Grundlage für weitere Forschung wird für die präklinische MSOT-Bildgebung eine synthetische Daten-Plattform entwickelt, welche insbesondere ein Werkzeug für ein verbessertes Studiendesign darstellt. Basierend auf den Erkenntnissen aus präklinischen Studien, erweitert diese Dissertation das Anwendungsfeld der MSOT-Technologie. Um die Umsetzung eines handgeführten MSOT-Scanners zu ermöglichen, mussten in Sachen Design viele Herausforderungen in Bezug auf Bildqualität und Präzision überwunden werden (z.B. begrenzter Öffnungswinkel sowohl bei der Beleuchtung als auch bei der Erfassung). Als eine der zentralen Lösungen steht hier ein hybrides MSOT- und Ultraschallsystem im Fokus dieser Dissertation. Um die komplementäre Information von MSOT- und

Ultraschallbildgebung zu vereinen, wurden beide Modalitäten studiert und optimiert. Auf dieser Grundlage wurden schließlich die Ultraschallbilder als A-priori-Information für die optoakustische Rekonstruktion benutzt, um die Bildqualität zu verbessern. Mit der in dieser Dissertation präsentierten Methoden können wir mehr Information aus MSOT- und Ultraschall-Bildern extrahieren und ermöglichen damit potenziell eine Erweiterung der Einsätzmöglichkeiten der MSOT-Technologie im klinischen Bereich.

List of abbreviations

MSOT	multispectral optoacoustic tomography
OA	optoacoustic
US	ultrasound
OPUS	optoacoustic and ultrasound
CT	computed tomography
PET	positron emission tomography
SPECT	single-photon emission computed tomography
MRI	magnetic resonance imaging
UTT	ultrasound transmission tomography
DOT	diffuse optical tomography
OPO	optical parametric oscillator
CW	continuous wave
NIR	near infrared
DAQ	data acquisition
A-mode	amplitude-mode
B-mode	brightness-mode
2D	2-dimensional
3D	3-dimensional
SoS	speed of sound
ToF	time of flight
sO2	oxygen saturation
ROI	region of interest
FOV	field of view
SDF	synthetic data framework

FEM	finite element method
LSQR	least squares minimization algorithm
IMMI	interpolated-matrix-model inversion
SNR	signal-to-noise ratio
CNR	contrast noise ratio
SIR	spatial impulse response
EIR	electrical impulse response
SSIM	structural similarity
AMF	adaptive matched filter
PCA	principal component analysis
AIP	average intensity projection
MIP	maximum intensity projection
MRA	magnetic resonance angiography
I/Q	in-phase/quadrature
SAU	synthetic aperture ultrasound
SRA	synthetic receive aperture
STA	synthetic transmit aperture
FMM	fast marching method
MSFM	multi-stencils fast marching method
ICG	indocyanine green
AF750	Alexafluor750
GNRs	gold nanorods

List of figures

Figure 1.1. Schematic of the major components in MSOT systems. 3

Figure 3.1. Schematic presentation of the SDF-based molecular sensitivity study. 16

Figure 3.2. Workflow of the generation process of optoacoustic signals of an absorber. 17

Figure 3.3. Estimation of the light fluence within tissue background. 19

Figure 3.4. Schematic of target implantation. 21

Figure 3.5. Schematic of the determination of MSOT molecular sensitivity. 21

Figure 3.6. Comparison of the image intensity within the agent area between experimental and synthetic images. 23

Figure 3.7. The minimum detectable concentration of AF750 after spectral unmixing in experimental and synthetic datasets. **Error! Bookmark not defined.**

Figure 3.8. Molecular sensitivity curves of AF750 and GNRs as a function of depth with agents showing disk-like distributions with diameters of 1, 2 or 3 mm. 26

Figure 3.9. Molecular sensitivity curve of AF750 in the liver region as a function of depth with agents showing disk-like distributions with a diameter of 2 mm. 27

Figure 4.1. The hybrid OPUS imaging system and dual-modality operating procedure. 35

Figure 5.1. Comparison of phantom reconstruction assuming uniform SoS or dual-SoS. 39

Figure 5.2. Comparison of image reconstruction of human forearm assuming uniform SoS or dual-SoS. 40

Figure 5.3. Comparison of image reconstruction of human neck region assuming uniform SoS or dual-SoS. 41

Figure 6.1. Generic synthetic aperture ultrasound imaging. 45

Figure 6.2. Synthetic receive aperture (SRA) ultrasound imaging. 46

Figure 6.3. Synthetic transmit aperture (STA) ultrasound imaging. 46

Figure 6.4. The STA in the Acuity256 system. 47

Figure 6.5. Schematic of the spatial relationship among all variables in in the image reconstruction described in this chapter. 48

Figure 6.6. Reconstructed ultrasound images with three different Z-projection methods. 50

Figure 6.7. Signal preprocessing results with Hilbert transform-based envelope detection method and spiking deconvolution. 52

Figure 6.8. Reconstruction of a commercially available acoustic phantom using three signal preprocessing strategies. 54

Figure 6.9. Three different transmitting and receiving schemes and their ability to reconstruct the phantom described in Figure 6.8. 55

Figure 7.1. Block diagram of prior-integrated reconstruction, the related imaging setup and numerical phantom used for simulation. 64

Figure 7.2. Integrating US priors into the OA reconstruction enhances the contrast and reduces limited-view artifacts..... 67

Figure 7.3. Effects of segmentation accuracy and the number of ROIs on prior-integrated reconstruction..... 68

Figure 7.4. Effects of ROI labelling on prior-integrated reconstruction. 69

Figure 7.5. The prior mask affects the choice of appropriate regularization parameter. 70

Figure 7.6. Prior-integrated reconstruction improves the contrast of the radial artery (yellow arrow) deep in tissue. 71

Figure 7.7. Prior-integrated reconstruction improves the contrast of the carotid and the detectability of a plaque inside the carotid..... 72

Figure 7.8. Statistical analysis of carotid images from atherosclerosis patients and healthy volunteers. 73

Figure 8.1. Ultrasound-image-driven high-quality reconstruction scheme..... 78

Figure 8.2. Framework of iterative US-image-driven SoS reconstruction. 79

Figure 8.3. Linear regression of tissue density and SoS. 80

Figure 8.4. Workflow of ultrasound image simulation. 81

Figure 8.5. multispectral OA data-driven clustering to segment and identify different tissue types..... 83

Figure 8.6. Schematic of the multispectral optoacoustic data-driven clustering method..... 85

Figure 8.7. Experimental hybrid OPUS system. 88

Figure 8.8. Spatial-variant SoS and ToF calculation from image region to the whole field. 89

Figure 8.9. Convergence of the framework shown in Figure 8.2. 90

Figure 8.10. Reconstruction of phantom/simulations with dual-SoS and spatial-variant SoS model. 91

Figure 8.11. Reconstruction of an arm dataset with spatial-variant SoS and dual-SoS model. 92

List of tables

Table 3.1 Summary of *in vivo* experiments 22
Table 3.2 Summary of reported molecular sensitivities with nanorods and dyes 29
Table 8.1 Ultrasound-image-driven high-quality reconstruction algorithm 86

Contents

Abstract ..... **i**

Zusammenfassung ..... **iii**

List of abbreviations ..... **v**

List of figures ..... **vii**

List of tables ..... **ix**

Contents ..... **xi**

1. Introduction **1**

1.1 Optoacoustic imaging 1

1.2 Multispectral optoacoustic tomography 1

1.3 Preclinical MSOT imaging 2

1.4 Clinical handheld MSOT imaging 3

1.5 Clinical handheld hybrid optoacoustic and ultrasound (OPUS) imaging 4

1.6 Outline of the thesis 4

2. Technical background of MSOT **7**

2.1 Physics of acoustic wave generation and propagation in optoacoustic imaging 7

2.1.1 The generation of acoustic waves in optoacoustic imaging 7

2.1.2 The propagation of acoustic waves 7

2.2 Technical background of optoacoustic image reconstruction 9

2.2.1 Back-projection reconstruction 9

2.2.2 Model-based reconstruction 10

2.2.3 ***L2*** regularization 10

2.3 Spectral unmixing 10

3. A Synthetic Data Framework (SDF) for prediction of molecular sensitivity of preclinical MSOT **15**

3.1 Motivation 15

3.2 Synthetic Dataset Framework (SDF) 16

3.2.1 Simulation of optoacoustic signals of contrast agents 17

3.2.2 Target implantation 20
3.2.3 Molecular sensitivity calculation 21
3.3 Validation of SDF 22
3.3.1 Intensity validation 23
3.3.2 Molecular sensitivity validation 24
3.4 SDF-based molecular sensitivity study 25
3.5 Discussion and outlook 27
4. Characteristics and operation of the OPUS system 33
4.1 The probe designs of OPUS systems 33
4.2 Operation principles of the experimental OPUS system – Acuity256 34
5. Dual-Speed-of-Sound (SoS) model-based optoacoustic reconstruction 37
5.1 Motivation 37
5.2 Dual-SoS model-based optoacoustic reconstruction 37
5.2.1 Methods 38
5.2.2 Optoacoustic imaging of phantoms and human tissue with Acuity256 39
5.2.3 Results 39
5.3 Discussion and outlook 42
6. Ultrasound imaging and image reconstruction in OPUS systems 43
6.1 Conventional ultrasound imaging in medical applications 43
6.2 Ultrasound imaging with the customized OPUS system 45
6.3 Ultrasound image formation 47
6.3.1 Delay-and-sum reconstruction 47
6.3.2 Advanced signal preprocessing 51
6.4 Variation of default STA 54
6.5 Discussion and outlook 56
7. US structural prior integrated model-based optoacoustic reconstruction 61
7.1 Motivation 61
7.2 Methods to integrate structural ultrasound prior 62
7.2.1 Spatial high-pass filter regularization (standard reconstruction) 63
7.2.2 Regional Laplacian regularization (prior-integrated reconstruction) 63
7.2.3 Numerical simulation 64
7.2.4 Tissue imaging of healthy volunteers and patients 66
7.2.5 Image quality evaluation 66

7.3 Results 66
7.3.1 Simulations 67
7.3.2 Clinical datasets 70
7.4 Discussion and outlook 74
8. Ultrasound SoS prior integrated optoacoustic reconstruction 77
8.1 Motivation 77
8.2 Ultrasound-image-driven SoS reconstruction 78
8.2.1 Iterative ultrasound-image-driven SoS reconstruction 79
8.2.2 Model-based SoS reconstruction 80
8.2.3 Initial SoS guess – multispectral optoacoustic data-driven clustering 84
8.2.4 Bent-ray propagation -- Fast Marching Method (FMM) 85
8.2.5 Experimental settings 87
8.3 Results 88
8.3.1 Ultrasound image model validation 89
8.3.2 Reconstructed SoS in tissue 90
8.3.3 Image reconstruction results with spatial-variant SoS 90
8.4 Discussion and conclusion 92
9. Conclusion and outlook 95
Acknowledgements 99
Appendix A. List of publications 101
Appendix B. Permission to reuse content from publications 102
Bibliography 103

1. Introduction

1.1 Optoacoustic imaging

As an inherently hybrid imaging modality, optoacoustic (photoacoustic) imaging capitalizes on the strengths of optical and acoustic imaging in acquisition of high-resolution images with molecular specificity from depth not accessible to any optical modality [1-4]. The underlying physical phenomenon is the photoacoustic effect, which describes the induction of acoustic pressure waves following the absorption of light [5]. In optoacoustics, tissue is illuminated with modulated light to generate acoustic responses from optical absorbers due to the thermoelastic expansion of tissue [6]. Thus, similar to purely optical imaging methods, optoacoustic imaging illuminates the specimen with light. However, instead of collecting photons for image production, optoacoustic imaging makes use of the conversion of the light energy into ultrasound waves by optical absorbers, with their detection using ultrasonic transducers [7]. As a result, optoacoustic imaging combines the molecular specificity of optical imaging with capabilities of spectral differentiation of molecular absorbers. Since sound waves are scattered orders of magnitude less than light waves as they propagate through tissue, optoacoustic imaging enables to generate high resolution images at depths limited by ultrasound diffraction [2]. Through such merger of the light and sound, optoacoustic gains a great degree of imaging flexibility with fully maintained molecular specificity and spectral flexibility [8].

Optoacoustic imaging as an emerging biomedical imaging modality has been widely used in preclinical and clinical research [9-12]. Optoacoustic imaging is usually implemented in the time domain using high-energy light pulses (>10 mJ/pulse) lasting shorter than approximately 10 ns to induce acoustic responses from optical absorbers. Time domain optoacoustic imaging generates broadband acoustic signals due to the ultrashort excitation profile, ranging from MHz up to hundreds of MHz [13, 14], generated by objects with sizes between 1.5 mm and <15 μm. Optoacoustic imaging can also be implemented in the frequency domain using intensity modulated continuous wave (CW) lasers [15], which offers mainly the advantage of using economic light sources such as diode lasers which are technically simpler and more stable, as opposed to the optical parametric oscillator (OPO) based technology used in time domain optoacoustic imaging [16, 17].

1.2 Multispectral optoacoustic tomography

As a subclass of optoacoustic imaging, multispectral optoacoustic tomography (MSOT) has been developed and applied in biomedical applications, demonstrating the ability to differentiate tissues *in vivo* and *ex vivo* in real time with and without the application of contrast agents several millimeters deep in the biological specimen with numerous research and translational applications for biomedical imaging [8, 18, 19]. Offering much higher resolution than diffuse optical tomography [20], MSOT is able to resolve morphological structures and to accurately quantify tissue biomarkers, which is not possible using diffuse photons [10].

MSOT takes the advantage of multi-wavelength illumination operating in the near-infrared (NIR) spectral region, which allows deep penetration in tissue [19], and tomographic detection, which enables high signal-to-noise ratio (SNR) [1]. The illumination wavelength of MSOT is normally between 650 nm and 950 nm which is known as the first optical window. This spectral range is widely used in tissue studies, since tissue is of minimal absorption and less scattering in the first optical window than that in shorter wavelengths [21], therefore enables the delivery of sufficient optical energy to generate detectable acoustic pressure from 30 – 60 mm depth [9].

Different from single-wavelength optoacoustic imaging, MSOT results in at least 3-dimensional image stacks, i.e. 2 spatial dimensions and another spectral dimension. The spectral dimension is of particular importance for functional analysis in biomedical studies, since spectral information is the foundation to identify different optical absorbers, whether endogenous (oxygenated and deoxygenated hemoglobin, melanin, and lipid) [8, 10, 22] or exogenous (imaging probes, nanoparticles) [8]. For imaging intrinsic absorbers, many tissue physiology studies based on hemoglobin have been carried out. As an important indicator to tissue physiological and pathological conditions, oxygen saturation (sO2) [23], which is the fraction of oxygenated hemoglobin to the total hemoglobin, has been studied non-invasively with MSOT. Matrix metalloproteinase activity, typically associated with atherosclerotic plaque instability, has been resolved in *ex vivo* human carotid plaques [22]. Lipids, absorbing light in the wavelength range of 1210 nm, were clearly identified and characterized in plaques within human aorta and carotid artery samples *ex vivo* [24, 25]. For the biomedical applications based on optoacoustic contrast agents, a number of moieties that absorb light have been resolved with MSOT, including fluorescent proteins [26, 27]; fluorescent dyes such as IRDye800 [28], indocyanine green (ICG) [29-33], and Alexafluor750 (AF750) [18]; carbon nanotubes [34]; polymer nanoparticles [35, 36]; and gold nanorods (GNRs) [33, 37, 38].

In addition, the multispectral illumination with the help of spectral unmixing algorithms can improve the detection sensitivity of the optical absorbers comparing to the single wavelength image [39]. The detection sensitivity of conventional optoacoustic tomography with single wavelength depends purely on the SNR of the target to background, therefore, an absorber of interest can be studied only if its absorbed light energy is higher than that of the background tissue. However, with multi-wavelength illumination, an absorber of interest can be studied based on its spectral signature. Therefore, even its absorbed light energy is lower than the background, it can be differentiated from background by its spectral signature. Moreover, when there exist multiple absorbers with distinct absorption peaks, they can be decomposed using spectral unmixing methods and lower the minimum detectable concentrations than single wavelength optoacoustics.

1.3 Preclinical MSOT imaging

As an important stepping stone to study and guide clinical studies about the progression of human diseases and their corresponding therapies, small animals especially mice are widely used in biomedical researches [6, 19, 40], which are classified as preclinical studies while the studies based on human are classified as clinical studies. For preclinical optoacoustic imaging, *in vivo* whole-body small animal MSOT is of particular interest since it allows longitudinal studies to follow the disease and therapy progression in a large time scale and enables the

development of different human disease models in different organs or tissues on mice [19, 40]. There are several commercial preclinical MSOT systems, including inVision256 (iThera Medical), Vevo Lazr (Visual Sonics), LOIS-3D (TomoWave Laboratories), Nexus (Endra) and a number of laboratory system designs that have been reported in the literature for imaging small animals. Herein, we take the inVision256 system, which is used for all preclinical studies in this dissertation, as an example to demonstrate the experimental orientations of MSOT imaging.

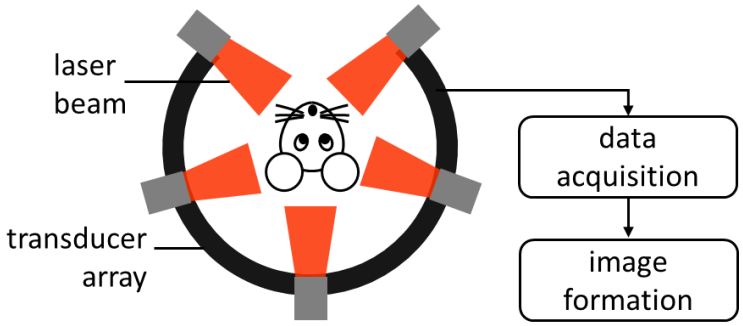

Figure 1.1. Schematic of the major components in MSOT systems.

As Figure 1.1 shows, preclinical MSOT (e.g. inVision256) comprises mainly three parts: illumination and detection system, data acquisition system, and image formation [41]. The detection system features a spherically concave array spanning 270° in the xy-plane with a radius of 40 mm. [42]. Each single element of the array is manufactured from the same piezocomposite material to cover central frequency 5MHz with -6dB of >50% frequency band [42]. For the illumination, a wavelength tunable pulsed laser with a pulse duration of <10ns, repetition rate of 10 Hz and peak pulse energy of 90 mJ at 750 nm is applied for multispectral measurements from 680nm to 950nm [42]. The laser beam was coupled into 10-arm fiber bundles next to the transducer array to establish ring illumination at the imaging plane. A custom-made data acquisition (DAQ) system digitized up to 256 channels in parallel at 10 Hz repetition rate and 40 MegaSamples/second. During *in vivo* measurements, the animal is anesthetized and positioned in an animal holder in the center of the imaging plane.

1.4 Clinical handheld MSOT imaging

Clinical MSOT has recently demonstrated potent clinical imaging abilities in cancer detection [43-46], label-free assessment of tissue inflammation [47, 48], tissue metabolism [49] or imaging of vascularization [50-52]. Comparing to the preclinical MSOT imaging demonstrated in Figure 1.1, clinical MSOT imaging has four major changes from hardware design to imaged specimen, i.e. illumination, detection, acquisition and specimen size. The first change is the hardware design of the transducer array and illumination. In order to bring MSOT into the clinics, a handheld device which is small and portable to allow clinicians scan patients conveniently like the case in ultrasound imaging is needed, which leads to the implementation of illumination and detection in a handheld probe. Such design results in the sample to be illuminated on only one side and only part of the resulting acoustic signal to be collected, which makes clinical optoacoustic image reconstruction a very ill-posed problem and results in limited-view artifacts. The second change occurs in the data acquisition stage. In preclinical MSOT imaging, 10 averages or more are normally used during data acquisition to assure a good SNR of the acquired signals. However, in clinical MSOT, normally no signal

averaging is done during data acquisition at each wavelength in order to achieve real-time-imaging and avoid motion artifacts introduced during measurements, which results in a lower SNR of optoacoustic signals than that in preclinical MSOT imaging. The third change is the size of the specimen. In clinical optoacoustic imaging, the specimen is human or the tissue or lesion inside human body which is of much larger size and require deeper imaging depth than in preclinical small-animal studies.

1.5 Clinical handheld hybrid optoacoustic and ultrasound (OPUS) imaging

In order to bypass the challenges imposed in clinical MSOT imaging, handheld MSOT is combined with complementary imaging modalities such as magnetic resonance imaging (MRI) and ultrasound (US) to enhance the capabilities of handheld MSOT and extract a richer range of physiological and pathophysiological information [53-55]. Among all hybrid imaging systems, integrating optoacoustic and ultrasound is particularly straightforward, since the two modalities rely on the same signal detection mechanism. This has given rise to handheld hybrid OPUS that have already shown promise for clinical use [46, 56-58]. Handheld OPUS system was used to noninvasively detect sentinel lymph node based on increased contrast from methylene blue in breast cancer patients [46]. Inflammation in arthritis patients' joints was identified and characterized based on the detection of hemodynamic changes with a handheld OPUS device [56]. Malignant and benign nodules in the thyroid were differentiated with a hybrid OPUS system [57]. Liver fibrosis was investigated and the capability of imaging heterogeneous liver structures with handheld OPUS system was demonstrated in [58].

In above mentioned studies, ultrasound images generally provided anatomical images of imaged tissue and were employed post-hoc to aid the interpretation of optoacoustic images. Besides providing post-hoc for optoacoustic image interpretation, the information carried in ultrasound images such as structural information and acoustic properties of tissue can be treated as priors for optoacoustic image reconstruction to improve image quality. Because of the potential and feasibility in clinical applications of handheld OPUS systems, it is worthwhile to optimize the image reconstruction for both imaging modalities in OPUS and develop methodology to fuse the hybrid information to maximize the value of OPUS systems.

1.6 Outline of the thesis

This dissertation is mainly about image reconstruction in clinical hybrid MSOT and ultrasound imaging. As the foundation of understanding, a general introduction of the optoacoustic imaging from preclinical to clinical is given in Chapter 1. Then more specific technical background about optoacoustic image reconstruction is introduced in Chapter 2. The rest of the dissertation is divided into three parts: "A study of molecular sensitivity of preclinical MSOT with synthetic data framework", "Studies of image reconstruction in handheld OPUS imaging" and "Studies of integrating hybrid information from handheld OPUS". In the first part, the imaging chain of MSOT from an optical absorber to multispectral images is introduced and a synthetic data framework is developed to study the molecular sensitivity of preclinical MSOT systems (Chapter 3). In the second part, the major challenges in clinical MSOT imaging and the customized reconstruction for each imaging modality in OPUS system are introduced. The hardware design and working scheme of hybrid OPUS imaging is introduced in detail based on a specific OPUS system in Chapter 4. To consider the

Speed of Sound (SoS) mismatch between coupling medium and tissue in clinical applications, an advanced dual-SoS reconstruction model is presented in Chapter 5. The adapted synthetic aperture technique and its corresponding ultrasound image reconstruction under the concave design of the transducer array are described in Chapter 6. After the single mode optoacoustic/ultrasound reconstruction being optimized, the efforts to integrate the hybrid information from OPUS imaging is presented in the third part. The structural information unfolded in ultrasound images are used as prior for optoacoustic image reconstruction to improve image quality and compensate for the limited-view artifacts (Chapter 7). Moreover, ultrasound images are used to derive the acoustic properties, such as SoS of imaged tissue, then the derived spatial-variant SoS is used along with bent-ray propagation model to improve optoacoustic image quality and accuracy (Chapter 8).

The dissertation is organized as follows:

Chapter 1 provides a brief introduction about optoacoustic imaging, multispectral optoacoustic tomography, and the preclinical and clinical MSOT systems.

Chapter 2 introduces the technical background about image reconstruction including wave equation, back-projection, model-based reconstruction, and spectral unmixing.

Chapter 3 introduces the imaging chain of preclinical MSOT, which enables the realistic simulation of optoacoustic signal from an optical absorber and the development of a synthetic data framework to allow estimation of the molecular sensitivity of various contrast agents under different tissue conditions without extensive animal experiments.

Chapter 4 indicts the major changes from preclinical to clinical MSOT in detection, illumination, and application requirements. Result from those changes, the challenges in clinical MSOT imaging are highlighted. As the foundation of the following four chapters, a specific OPUS system, i.e. Acuity256, is introduced in detail.

Chapter 5 presents a dual-SoS model-based reconstruction method for clinical MSOT imaging. The dual-SoS model is described and the comparison between single-SoS model and dual-SoS model is presented.

Chapter 6 introduces the synthetic aperture technique and the reconstruction of ultrasound images in hybrid OPUS, referring to conventional ultrasound imaging. Three signal processing methods and three image formation methods commonly used in ultrasound imaging are analyzed based on their influence on ultrasound image quality.

Chapter 7 describes a new method to incorporate ultrasound structural information into optoacoustic reconstruction to reduce the limited-view artifacts and improve contrast of clinical optoacoustic images. Phantoms and data from OPUS scans of human radial and carotid arteries are reconstructed with the proposed method and compared with conventional reconstruction without ultrasound prior to demonstrate the improvement in optoacoustic image quality.

Chapter 8 presents another new method to derive the spatial-variant SoS distribution from ultrasound images, then use the derived SoS to facilitate the optoacoustic image

reconstruction. Together with the spatial-variant SoS, the bent-ray propagation model is implemented using fast marching method. The improvement in image quality introduced by the new reconstruction scheme is demonstrated with simulation and experimental data.

Chapter 9 gives a brief summary and conclusion of the work presented in this dissertation and an outlook about the future development.

2. Technical background of MSOT

2.1 Physics of acoustic wave generation and propagation in optoacoustic imaging

2.1.1 The generation of acoustic waves in optoacoustic imaging

As mentioned in Chapter 1, the ultrasound pressure wave in optoacoustic imaging is formed due to the absorption of light, which is described as photoacoustic effect [5] and comprise three phases, i.e. the absorption of light, the localized pressure perturbation introduced by thermalization of absorbed energy, and the propagation of the localized pressure perturbation [59].

In most optoacoustic imaging applications, a laser beam in NIR range is used to illuminate samples with part of the photons being absorbed by the chromophores inside the sample. Then the absorbed light energy is converted into heat via vibrational relaxation, which gives a rise in local temperature and pressure. In thermal confinement [20] and stress confinement [20], the generated local pressure perturbation p_0 can be written as [59]

$$p_0 = \Gamma \cdot H, \qquad (2.1)$$

where Γ is the Grüneisen parameter demonstrating the photoacoustic efficiency of an absorbing chromophore and H is the deposited heat per unit volume which is the product of light fluence Φ and the optical absorption coefficient μ_a, i.e. $H = \mu_a \Phi$. Because of the elastic nature of tissue, the local pressure perturbation p_0 propagates outwards in all directions and referred as initial acoustic pressure distribution.

2.1.2 The propagation of acoustic waves

The propagation of an acoustic wave is the fluctuation of the pressure field in the medium [60]. In most cases, the propagation of acoustic waves in tissue is approximated with that in fluid [61], therefore can be described with the wave equation in fluid. The derivation of wave equation in fluid is based on the fact that the propagation of a sound wave meets three laws: (1) the conservation of mass; (2) motion equation of fluid; and (3) the pressure-density relations in fluid [60]. The following derivation of wave equation is based on [60, 61].

The law of conservation of mass says that the mass (M) of a closed system must remain constant over time, which can be expressed as $\frac{dM}{dt} = \frac{d}{dt}\iiint_V \rho dV = 0$, where V represents a volume in three-dimensional space which is compact and has a piecewise smooth boundary S. This can be met only if the change of the mass enclosed by a closed surface in time is equal to the mass that traverses the surface, which can be expressed as

$$\frac{d}{dt}\iiint_V \rho dV + \oiint_S \rho \boldsymbol{v} dS = 0, \quad (2.2)$$

where $\boldsymbol{v}$ is the flow velocity field and ρ is the density. $\boldsymbol{v}$ is negative if matter goes in and positive if matter goes out from the surface, which is consistent with the normal vector of the surface. With Gauss theorem, Equation 2.2 can be reformed as

$$\frac{\partial \rho}{\partial t} + \nabla(\rho \boldsymbol{v}) = 0. \qquad (2.3)$$

Motion Equation in fluid is derived by Euler based on Newton's second law of motion which indicts that resulting from a net force, the acceleration of an object is proportional to the magnitude of the force and inversely proportional to the mass of the object, i.e. $F = m\frac{d\boldsymbol{v}}{dt} = \frac{d}{dt}\iiint_V \rho v dV$. In ideal fluid which has no viscosity and body force, last equation can be rewritten as

$$\frac{d}{dt}\iiint_V \rho v dV = -\oiint_S p dS, \qquad (2.4)$$

where p is the pressure on the surface and the minus sign comes from the fact that the force is considered towards the surface, while the normal vector of the surface points outward. With Gauss theorem, Equation 2.4 can be simplified as

$$\rho \frac{d\boldsymbol{v}}{dt} = -\nabla p. \qquad (2.5)$$

The pressure-density relation in fluid is described by Newton-Laplace equations as

$$p = \rho c^2, \qquad (2.6)$$

where c is the SoS in the medium.

Combing Equation 2.3 and 2.6 with the assumption that the medium is acoustically homogeneous gives

$$\frac{1}{c^2}\frac{\partial p}{\partial t} + \rho \nabla \boldsymbol{v} = 0. \qquad (2.7)$$

Differentiating Equation 2.7 with respect to time gives $\frac{1}{c^2}\frac{\partial^2 p}{\partial^2 t} + \rho \nabla \frac{\partial \boldsymbol{v}}{\partial t} = 0$. Substituting Equation 2.5 into Equation 2.7 gives the wave equation with respect to pressure as

$$\nabla^2 p - \frac{1}{c^2}\frac{\partial^2 p}{\partial^2 t} = 0. \qquad (2.8)$$

In optoacoustic imaging, the wave source is the local pressure perturbation due to light energy absorption. In order to model the physical processes of thermalization of absorbed energy following tissue excitation by a light source, the energy conservation law (Equation 2.9 [62]) should be considered.

$$\rho \mathrm{T}\frac{\partial \mathrm{E}}{\partial \mathrm{t}} = \nabla(k \nabla T) + H, \quad (2.9)$$

where E, k, and T denote the entropy, thermal conductivity, and temperature, respectively. Combining Equation 2.9 with Equation 2.3, Equation 2.5, and the thermodynamic relation (i.e. $\rho \mathrm{TE} = \rho c_p T - \gamma \beta T p$, where γ, β, and c_p denote the heat capacity ratio, the volumetric pressure expansion coefficient, and the heat capacity at constant pressure, respectively), the

optoacoustic wave equation.in homogeneous medium and thermal confinement can be written as [62-64]

$$\frac{\partial^2 p}{\partial^2 t} - c^2 \nabla^2 p = \Gamma \frac{\partial H(\boldsymbol{r},\mathrm{t})}{\partial t}. \qquad (2.10)$$

2.2 Technical background of optoacoustic image reconstruction

With the initial acoustic pressure distribution p_0 at $t = 0$ satisfies $p_0(\boldsymbol{r}) \coloneqq p(\boldsymbol{r}, 0) = \Gamma H(\boldsymbol{r})$ with vanishing time derivative $\frac{\partial}{\partial t} p(\boldsymbol{r}, 0) = 0$, the entire optoacoustic effect can be formulated with the source function serves as an initial condition as follows:

$$\nabla^2 p - \frac{1}{c^2}\frac{\partial^2 p}{\partial^2 t} = 0,$$
$$p(\boldsymbol{r}, 0) = \Gamma H(\boldsymbol{r}),$$
$$\frac{\partial}{\partial t} p(\boldsymbol{r}, 0) = 0.$$

This is the optoacoustic wave equation Cauchy problem [62] and can be solved using the Green's function. The pressure distribution at $\boldsymbol{r}$ and t in an acoustic homogeneous medium is then given by [65]:

$$p(\boldsymbol{r}, t) = \frac{\Gamma}{4\pi c}\frac{\partial}{\partial t}\int_{|\boldsymbol{r}-\boldsymbol{r}'|=ct} \frac{H(\boldsymbol{r}')}{|\boldsymbol{r}-\boldsymbol{r}'|} d\boldsymbol{r}'. \qquad (2.11)$$

The integral indicts an integration over a sphere in 3D problem or an integration over a circle in 2D problem with origin in $\boldsymbol{r}$ and radius of ct [65]. All optoacoustic image reconstruction problem is trying to recover the spatial distribution of p_0 or H, given the optoacoustic signal $p(\boldsymbol{r_d}, t)$ at a detector location $\boldsymbol{r_d}$ [64-67]. Back-projection and model-based reconstruction are most commonly used methods to solve the above problem.

2.2.1 Back-projection reconstruction

The back-projection formula in time domain can be written as [64, 68]:

$$p_0(\boldsymbol{r}) = \int_{|\boldsymbol{r}-\boldsymbol{r}'|=\bar{t}} \left[2p(\boldsymbol{r}', \bar{t}) - 2\bar{t}\frac{\partial p(\boldsymbol{r}', \bar{t})}{\partial \bar{t}}\right] \frac{d\Omega(\mathrm{r}\prime)}{\Omega_0}, \qquad (2.12)$$

where $\bar{t} = ct$, $\left[2p(\boldsymbol{r}', \bar{t}) - 2\bar{t}\frac{\partial p(\boldsymbol{r}', \bar{t})}{\partial \bar{t}}\right]$ is the back-projection term, $d\Omega(\mathrm{r}') = \frac{dS_0}{|\boldsymbol{r}-\boldsymbol{r}'|^2} \cdot [\boldsymbol{n}(\boldsymbol{r}') \cdot (\boldsymbol{r} - \boldsymbol{r}')/|\boldsymbol{r} - \boldsymbol{r}'|]$ is the solid angle for a detection element dS_0 with respect to a spatial location $\mathbf{r}$ and $\boldsymbol{n}(\boldsymbol{r}')$ denotes the outward-pointing normal of the integration surface at $\boldsymbol{r}'$. In Equation 2.12, Ω_0 is a solid angle of the whole integration surface, i.e. $\Omega_0 = 2\pi$ for planar geometry and $\Omega_0 = 4\pi$ for spherical and cylindrical geometry. In tomography, several detector elements at different spatial locations along the surface are used for detection, so $d\Omega_0/\Omega_0$ denotes the weighting factor of the contribution of a single detection element to a reconstruction point p at $\mathbf{r'}$**.** The reconstruction is simply projecting the detected signal $p(\boldsymbol{r}', t)$ from each transducer element backward on a spherical surface or a circle with respect to the location of the transducer element $\boldsymbol{r_d}$ [64]**.**

Nevertheless, images reconstructed with back-projection algorithms suffer from approximation errors, leading to less accurate quantitative functional or molecular imaging

[69]. Moreover, back-projection cannot account for the information loss due to limited view detection.

2.2.2 Model-based reconstruction

Model-based reconstruction reconstructs optoacoustic images by minimizing the discrepancy between the measured acoustic signals and the signals theoretically predicted by the forward model. Rosenthal et al. [65] developed a semi-analytical model-based scheme, termed interpolated-matrix-model inversion (IMMI), to achieve real-time reconstruction. Discretizing the linear forward model for acoustic wave propagation in Equation 2.11 leads to

$$\boldsymbol{p} = \boldsymbol{M}\boldsymbol{x}, \qquad (2.13)$$

where $\boldsymbol{p}$ stands for the optoacoustic signal; $\boldsymbol{x}$ is the unknown image, i.e., the spatial distribution of energy absorbed per unit volume of the tissue in the imaging plane, written in a vector representation; and $\boldsymbol{M}$ is the model matrix that computes sound propagation in the imaged medium for the experimental acquisition geometry employed. The inversion of Equation 2.13 is achieved by minimizing the squared error

$$\boldsymbol{x}_{sol} = \arg\min_{\boldsymbol{x}} \|\boldsymbol{p}_{det} - \boldsymbol{M}\boldsymbol{x}\|_2^2, \qquad (2.14)$$

typically using the least squares minimization algorithm (LSQR) algorithm. In Equation 2.14, $\boldsymbol{p}_{det}$ is the experimentally detected optoacoustic signal and $\|\cdot\|_2$ is the L^2-norm.

2.2.3 L^2 regularization

As the minimization problem given in Equation 2.14 is ill-posed for limited-view geometry of handheld probes, regularization is required to achieve a unique and stable reconstruction. In addition, a suitable regularization often reduces the noise level and artifacts [63, 67]. The most common regularization method is L^2 regularization, i.e. regularization with a functional of the form $\boldsymbol{x} \mapsto \|\boldsymbol{L}\boldsymbol{x}\|_2^2$:

$$\boldsymbol{x}_{sol} = \arg\min_{\boldsymbol{x}} \|\boldsymbol{p}_{det} - \boldsymbol{M}\boldsymbol{x}\|_2^2 + \lambda\|\boldsymbol{L}\boldsymbol{x}\|_2^2, \qquad (2.15)$$

where $\boldsymbol{L}$ is the regularization matrix and capable to integrate prior information about the solution and $\lambda > 0$ is the regularization parameter. A suitable regularization parameter can, for example, be selected via the L-curve. The L-curve is a plot of the penalty term ($\|\boldsymbol{L}\boldsymbol{x}\|_2$) against the norm of the residual ($\|\boldsymbol{p}_{det} - \boldsymbol{M}\boldsymbol{x}\|_2$). It is a convenient graphical tool for displaying the trade-off between the regularizing functional and the fit to the given data in dependence of the regularization parameter. Usually, the optimal trade-off is achieved close to the corner of the L-shaped curve [70].

2.3 Spectral unmixing

In MSOT imaging, the reconstructed optoacoustic images $\boldsymbol{x}_{sol}$ represent the initial pressure distribution p_0 in the region of interest (ROI), which is a combination of Grüneisen parameter, optical absorption coefficient and light fluence, i.e. $p_0 = \Gamma\mu_a\Phi$. Γ is a known constant when the absorber is decided and if the light fluence Φ can be taken as constant if the light energy

arriving at the absorbers at each wavelength is uniform. In this case, the optoacoustic spectra, which are defined as the intensity of recovered optoacoustic images within the absorber area along with multiple wavelengths, are consistent with the absorption spectra of absorbers measured with other optical methods such as optical spectrometer, i.e. $p_0(\lambda)$ and $\mu_a(\lambda)$ are equivalent. Thus, different absorbers and their concentrations can be easily identified with linear unmixing, since $p_0(\lambda)$ can be decomposed into the proportion/weight w of each individual absorber's absorption spectrum $\mu_a(\lambda)$ as [59]:

$$p_0(\lambda) = \sum_{i=1}^{N_a} w_i \cdot \mu_{a,i}(\lambda), \qquad (2.16)$$

where i denotes the ith type of absorbers and N_a is the total number of the absorber types.

However, in most biomedical imaging applications, the assumption of uniform light fluence at different wavelengths does not hold true and the optoacoustic spectral signature of the same absorber can be distorted by surrounding tissues, which complicates the unmixing problem [59]. In reality, biological tissue is highly scattering and has numerous intrinsic absorbers of different optical absorption spectra. Therefore, light travels a long way to arrive at the surface of the absorber and is of varied energy at different wavelengths. In other words, the optoacoustic spectrum $p_0(\lambda)$ is not consistent with $\mu_a(\lambda)$, instead, it is the combination of the spectra of the fluence $\Phi(\mathbf{x}, \lambda)$ and the absorption spectrum $\mu_a(\lambda)$, which is termed as 'spectral coloring' [59]. In this case, directly applying linear unmixing to $p_0(\lambda)$ works poorly and either light fluence compensation or more advanced algorithms based on statistical methods are needed. Light fluence compensation is straightforward to come up, but nontrivial to fulfill, since the light fluence estimation in *in vivo* tissues is very difficult and therefore remains an unsolved problem. In order to avoid light fluence estimation, statistical methods have been developed to overcome the spectral coloring effect by modeling the spectral fluctuation using priors [71]. Those statistical unmixing algorithms can be classified into two categories depending on their goals: one is to identify the relative ratios of the intrinsic absorbers such as the oxygenated and deoxygenated blood [72, 73], which is for tissue physiology study; while the other is to identify the existence of the extrinsic absorbers, which is also termed as 'target detection' [71, 74] and suitable for molecular imaging applications.

Section I: A study of molecular sensitivity of preclinical MSOT with synthetic data framework

3. A Synthetic Data Framework (SDF) for prediction of molecular sensitivity of preclinical MSOT

3.1 Motivation

Contrast agents that absorb light have been widely used in small-animal studies using preclinical MSOT. The optimal concentration of these contrast agents for a given experimental situation and imaging set-up cannot currently be estimated in advance, which means that it must be determined through pilot studies that require time and effort and increase the number of experimental animals required. Such pilot studies could be minimized if an analytical method was available to estimate the minimum detectable concentration, i.e. molecular sensitivity [76, 77] for contrast agents under a given set of experimental conditions and imaging hardware specifications. Such a method could also help streamline efforts to design next-generation optoacoustic contrast agents.

The molecular sensitivity of MSOT depends on a multitude of parameters: (1) characteristics of the contrast agents employed, i.e. the molar extinction coefficient, Grüneisen coefficient and the absorption spectrum; (2) the agent location within tissue (tissue depth); (3) the size of the lesion occupied by the agent; (4) the optical properties and overall characteristics of the imaged tissue; (5) the specifications of the imaging system and (6) the image reconstruction and spectral analysis method used, therefore, varies substantially across studies.

Different methods and research groups have attempted to characterize the molecular sensitivity of MSOT with simulations or phantom experiments [30, 53, 78]. Although such studies offer insight into the physical parameters affecting sensitivity, they typically do not consider the challenges of *in vivo* imaging, in which the optoacoustic contrast agent needs to be spectrally unmixed from a spatially heterogeneous absorbing tissue background. Therefore, the molecular sensitivity values refer to the particular parameters contained in the simulation or phantom studied but do not universally capture *in vivo* conditions. Detection limits in biological tissues (e.g. chicken muscle) *ex vivo* have also been considered for better approximation of tissue imaging conditions and for exploring the maximum imaging depth achieved using a certain agent concentration [28, 32, 79]. However, excised tissue muscle does not reproduce the complex, dynamic physiological conditions that affect optoacoustic contrast *in vivo*, such as the hemoglobin distribution. Moreover, those previous studies did not consider multispectral detection. Reports of the detection of contrast agents *in vivo* have enabled insights into the optoacoustic molecular sensitivity in real settings [18, 31, 34-36, 38, 53] but also do not allow for a generalized understanding of the molecular sensitivity achieved, because they report only on the specific conditions of the experimental measurements. Despite an extensive number of demonstrations with various dyes and

nanoparticles, it is not possible to extrapolate from those measurements in order to estimate the molecular sensitivity if experimental parameters change, such as the applied contrast agent, tissue, depth, lesion size or imaging set-up.

Therefore, we developed a streamlined approach to estimate the molecular sensitivity of contrast agents in small-animal optoacoustic molecular imaging for a given set of experimental conditions and imaging parameters, which may reduce the need for extensive animal experiments. We developed a Synthetic Data Framework (SDF) that combines experimental measurements and a signal simulation framework to derive synthetic multispectral optoacoustic images. Background optoacoustic signals are experimentally measured from animals *in vivo*, in the absence of exogenous agents. Using these measurements as the imaging background, SDF simulates the signals obtained from assumed agents embedded in tissue, enabling a framework that allows the generalized study of MSOT molecular sensitivity by achieving simulations that correspond to the optical properties and detection conditions of live animal tissues and the specifications of a real MSOT system. The SDF developed was validated using experimental *in vivo* MSOT data on tissue containing known concentrations of contrast agents. We showcase close agreement between SDF data and experimental data in terms of both image intensity and minimum detectable concentrations. Finally, using SDF we generalize observations of MSOT molecular sensitivity for different conditions, such as agent types, lesion size and imaging depth.

3.2 Synthetic Dataset Framework (SDF)

The SDF platform generates synthetic MSOT images that mimic MSOT experimental images, in which the tissue background is based on experimental data from healthy, untreated animals and the signal from exogenous contrast agent is simulated based on the known properties of the agent and the specifications of the MSOT imaging system. The SDF simulator compensates for the fact that while it is straightforward to simulate the propagation of optoacoustic signals emitted from well-defined agents, it is difficult to accurately simulate signals coming from tissue, since the optical and acoustic properties of biological tissues are not precisely known.

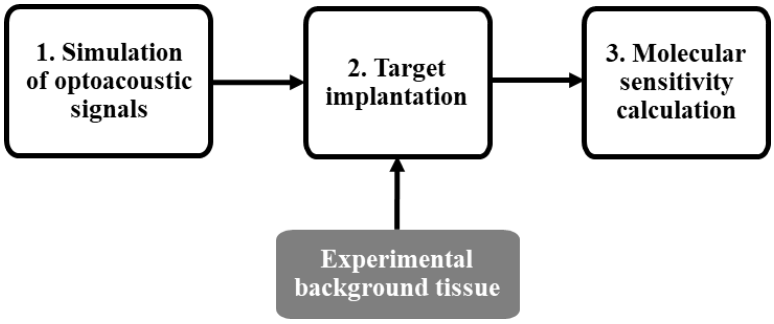

Figure 3.1. Schematic presentation of the SDF-based molecular sensitivity study. This figure is adapted from Ref. [75].

To develop a generalized way to study the MSOT molecular sensitivity, we developed a pipeline to study the MSOT molecular sensitivity based on the SDF, which comprises three modules as Figure 3.1shows. Each module in Figure 3.1is explained in detail in following text.

3.2.1 Simulation of optoacoustic signals of contrast agents

The formation of an optoacoustic signal includes three main factors [59]: (1) the light fluence at the agent location, (2) the propagation of pressure perturbations that arise when the tissue absorbs the laser light and heats up, and (3) the characteristics of the imaging system such as the spatial impulse response (SIR) and the electrical impulse response (EIR) of the transducer array. Serving the goal of simulating close-to-reality optoacoustic signals, the optoacoustic signal generation process is described in a mathematical way in this section.

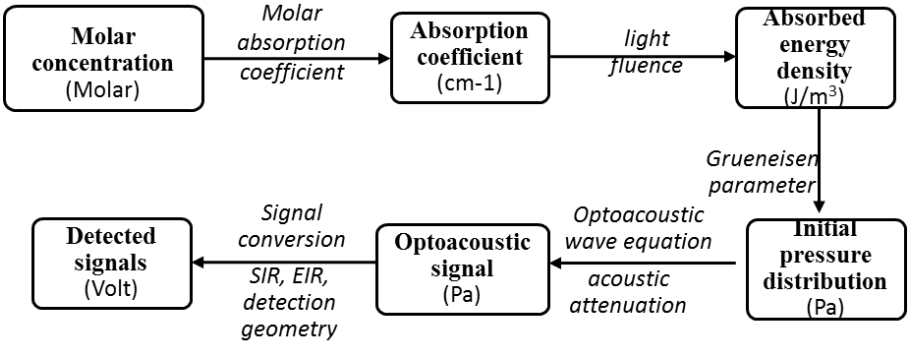

Figure 3.2. Workflow of the generation process of optoacoustic signals of an absorber. EIR, electrical impulse response and SIR, spatial impulse response. This figure is adapted from Ref. [75].

In the first stage, being illuminated by a transient light fluence field $\Phi(\mathbf{x},\lambda)$, an optical absorber of absorption coefficient $\mu_a(\mathbf{x},\lambda)$ generate the initial pressure P_{init}:

$$P_{init}(\mathbf{x},\lambda) = \Gamma \cdot \Phi(\mathbf{x},\lambda) \cdot \mu_a(\mathbf{x},\lambda), \qquad (3.1)$$

where $\mu_a(\mathbf{x},\lambda) = c_a(\mathbf{x})\varepsilon(\lambda)$, $\mathbf{x}$ is spatial coordinates, λ is the wavelength, c_a is the concentration of absorbers, ε is the molar extinction coefficient and Γ is the Grüneisen coefficient. The propagation of the initial pressure in the medium can be described with wave equation $\nabla^2 P - \frac{1}{c^2}\frac{\partial^2 P}{\partial^2 t} = P_{init}$, whose derivation and physical explanation can be found in Chapter 2 The wave equation is discretized and simplified as a model matrix, which allows the propagating pressure waves P_w be expressed as a function of the initial pressure distribution as:

$$P_w(\mathbf{x},\lambda) = \mathbf{M} \cdot P_{init}, \qquad (3.2)$$

where $\mathbf{M}$ is a model matrix that corresponds to the imaging geometry of the system and describes the optoacoustic wave propagation [65]. Then the pressure waves arrive at the surface of transducer and are spatially averaged by the active area of the transducer, which generate an averaged pressure $P_{avg}(\mathbf{x},\lambda)$ which can be modeled using the SIR of the transducer. The above process is noted mathematically as

$$P_{avg}(\mathbf{x},\lambda) = S(\mathbf{M}) \cdot P_{init}, \qquad (3.3)$$

where $S(\mathbf{M})$ stands for the operation that incorporates the SIR of the transducer array into model matrix $\mathbf{M}$. Discretization and details about the model matrix that incorporates the SIR have been described [80].

Because of the acoustic attenuation and the fact that optoacoustic signals are broadband [13], the amplitude of the averaged pressure is frequency- and distance-dependent. With the attenuation model in a uniformly attenuating medium, the acoustic pressure after attenuation P_{att} can be expressed as

$$P_{att}(\mathbf{x},\lambda)=\mathrm{Re}\{F^{-1}(F(P_{avg})\cdot h_{att})\}, \quad (3.4)$$

where F and F^{-1} stand for the Fourier and inverse Fourier transforms, respectively; and $h_{att}(f,d)=exp(-\alpha_{0f}|f|^{n}d)$ is the acoustic attenuation function [81], where α_{0f} is a material-related acoustic attenuation constant, n is a real positive constant, f is the frequency bandwidth of the agent and d is the propagation distance of the acoustic wave. For water, $\alpha_{0f}=0.00217\ dBMHz^{-1}cm^{-1}$ and n is 2; for tissues, n is 1 and $\alpha_{0f}\approx 0.5\ dBMHz^{-1}cm^{-1}$ [82]. The pressure signal $P_{\mathrm{att}}(\mathbf{x},\lambda)$ is converted into an electrical signal P:

$$P(\mathbf{x},\lambda,t)=k\cdot h_{EIR}(\mathbf{x},t)*P_{\mathrm{att}}(\mathbf{x},\lambda), \quad (3.5)$$

where $h_{EIR}(\mathbf{x},t)$ is the EIR of the transducer element [83] and k is a constant for converting pressure to voltage. Combining Equations 3.1-3.5 allows the acquired pressure signals to be expressed as a function of the absorber concentration:

$$P(\mathbf{x},\lambda)=k\cdot h_{EIR}*\mathrm{Re}\{F^{-1}(F(\Gamma\cdot S(\mathbf{M})\cdot\Phi\cdot c_a(\mathbf{x})\cdot\varepsilon)\cdot h_{att})\}. \quad (3.6)$$

Equation 3.6 expresses the acquired optoacoustic signals as a function of the spatially varying molar concentration $c_a(\mathbf{x})$ of absorbers through sequential steps graphically presented in Figure 3.2.

The simulation of optoacoustic signals is based on Equation 3.6 which includes three additional unknown parameters: the light fluence Φ, which is strongly dependent on the background tissue; the Grüneisen coefficient Γ of the agent, which is typically not known; and the conversion factor k of transducer. The Grüneisen coefficient and conversion factor are jointly estimated as one calibration factor cal, which leads to a simpler form of Equation 3.6:

$$P(\mathbf{x},\lambda)=cal\cdot h_{EIR}*\mathrm{Re}\{F^{-1}(F(S(\mathbf{M})\cdot\Phi\cdot c_a(\mathbf{x})\cdot\varepsilon)\cdot h_{att})\}, \quad (3.7)$$

where $cal=\Gamma\cdot k$. Light fluence and cal are estimated as described below.

1) Estimation of the light fluence field

As dictated by Equation 3.7, in order to simulate the optoacoustic signals emanating from a specific agent concentration distribution $c_a(\mathbf{x})$, an estimation of the light fluence field $\Phi(\mathbf{x},\lambda)$ is required. To simulate the light fluence within the tissue, we use a 2D finite element method (FEM) to solve a diffusion equation previously described for modeling light propagation inside turbid media [84]. This simulation of light fluence occurs in the following steps:

- An anesthetized mouse with a rectally inserted capillary tube filled with ink is scanned *in vivo* at 21 wavelengths (from 700 nm to 900 nm in 10-nm steps) in the lower abdominal area using MSOT.
- The experimental data acquired in step 1 are reconstructed.
- The tissue region is segmented based on the reconstructed images.

- Constant optical properties μ_a, μ_s and oxygen saturation (sO2) are assumed within the segmented tissue region.
- Based on the assumed optical properties, $\Phi(\mathbf{x}, \lambda)$ is simulated using the FEM, and the light fluence $\mathbf{\Phi_x}$ at the position **x** of the ink is obtained.
- Following Equation 3.1, $\mathbf{\Phi_x}$ is multiplied by the absorption spectrum of ink, which has previously been measured using a photospectrometer, to get the simulated optoacoustic spectrum $S_{ink.sim}(\lambda)$.
- The experimental optoacoustic spectrum of the ink $S_{ink.exp}(\lambda)$ is calculated from the reconstructed experimental images.
- $S_{ink.sim}(\lambda)$ is normalized and compared to the normalized $S_{ink.exp}(\lambda)$.
- The process is repeated by varying μ_a, μ_s and sO2 until an optimal fit between $S_{ink.sim}(\lambda)$ and $S_{ink.exp}(\lambda)$ is achieved.

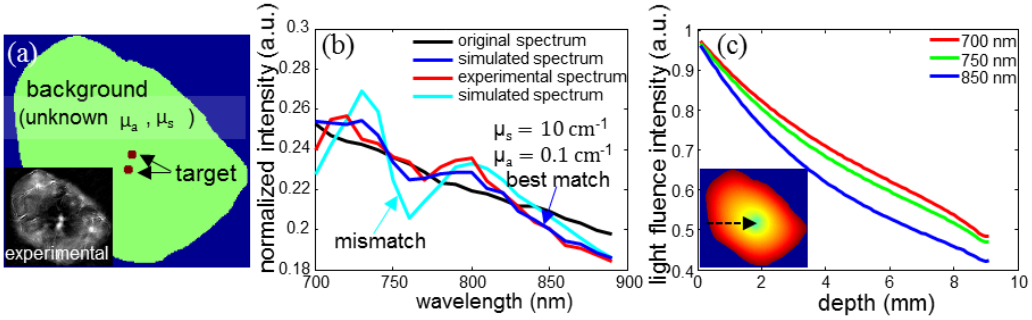

Figure 3.3. Estimation of the light fluence within tissue background. (a) Background tissue mask of Group A experiments; (b) estimation of tissue optical properties through fitting of the simulated colored spectra of ink to the experimental one; (c) light fluence profile from surface to center within the background. This figure is adapted from Ref. [75].

As Equation 3.7 dictates, the light fluence is an important input of the simulation of the optoacoustic signals emanating from a contrast agent. Figure 3.3 shows the light fluence estimation example related to the Group A experiments introduced in Section 3.3. Figure 3.3(a) shows the segmented mask from experimental MSOT images (highlighted as 'experimental' in all figures) of Group A experiments. In Figure 3.3(a), the background is the mouse tissue, for which both absorption and scattering are unknown. The absorption spectrum of the agent (ink in this case) was measured with a spectrometer in advance and the scattering coefficient of the ink solution was assumed to be approximately 0.01 cm^{-1}, since the ink was diluted in distilled water. Figure 3.3(b) shows the spectrum of ink from the spectrometer (black) and the colored spectra from the agent region in experimental (red) and synthetic (blue and cyan) images. As the blue, cyan and red curves stand for the absorbed energy per volume, compared to the original spectrum of ink, the obtained optoacoustic spectra are distorted by $\Phi(\mathbf{x}, \lambda)$ according to Equation 3.1. In Figure 3.3(b), the blue curve shows the best match of the simulated and experimental spectra with a tissue background of the scattering coefficient 10 cm-1 and absorption coefficient of 0.1 cm^{-1}. The cyan curve shows the mismatched simulated spectra of ink. Figure 3.3(c) shows the light fluence intensity profile from the surface to the center of the mask and the profiles from three different wavelengths (700, 750 and 850 nm) are presented. These profiles show that light

fluence within tissue is wavelength- and depth-dependent and is shaped by the optical properties of the background.

2) Estimation of the calibration factor (cal)

Since the calibration factor cal in Equation 3.7 accounts for the Grüneisen coefficient and the conversion factor, it is an agent-dependent constant when the imaging system is known. In order to calculate the calibration factor of different contrast agents, a cylindrical phantom with a diameter of 2 cm and containing 1.2% intralipid and 2.6% agar was imaged. In the center of the phantom, a tube with a 3-mm diameter was iteratively filled with a certain concentration of one of the following absorbers: India ink, AF750, ICG or GNRs. During the experiments, the phantom was fixed in the center of the transducer array and immersed in distilled water within a holder.

After the measurement, the experimental data were reconstructed and the signals of the contrast agent in the phantom were simulated and reconstructed based on Equation 3.7 assuming cal equals 1. Then we calculated the mean intensity of the agent region on the experimental and simulated optoacoustic images. Dividing the mean intensity of the experimental image by the mean intensity of the simulated image gave the calibration factor. Using these procedures, we calculated the following calibration factors: India ink, 5.18×10^{-6}; AF750, 3.0×10^{-6}; and GNRs, 4.0×10^{-6}.

3) Imaging system and parameter settings

During the simulation of optoacoustic signals using Equation 3.7, the system parameters are assigned based on the commercially available inVision256 system (iThera Medical GmbH, Munich, Germany), which features a transducer array of 256 cylindrically focused elements providing 270° angular coverage; the transducer array has a diameter of 40 mm and a central frequency of 5 MHz, since this machine is used for the *in vivo* experiments for validation purpose. The SIR of each transducer element is approximated by 140 line-transducers and simulated analytically. For the acoustic attenuation, the distance from the agent to the surface of the transducer is assumed to be constant at 4 cm (1 cm tissue and 3 cm water).

3.2.2 Target implantation

Figure 3.4 shows that the simulated optoacoustic signals P_{sim} (output of last section), which correspond to an assumed concentration distribution of an agent, are merged with experimentally measured background signals P_{exp} to produce synthetic signals. In other words,

$$P_{syn} = P_{sim} + P_{exp}. \qquad (3.8)$$

In Equation 3.8, P_{exp} is the experimental signals obtained from *in vivo* experiments of a mouse without any exogenous contrast agent, and the synthetic signals are reconstructed to generate synthetic MSOT images. In this chapter, we reconstruct all the MSOT images using a LSQR and standard Tikhonov regularization [69]. We reconstruct all the datasets in this work with a field of view (FOV) of $2cm \times 2cm$ and 200×200 pixels.

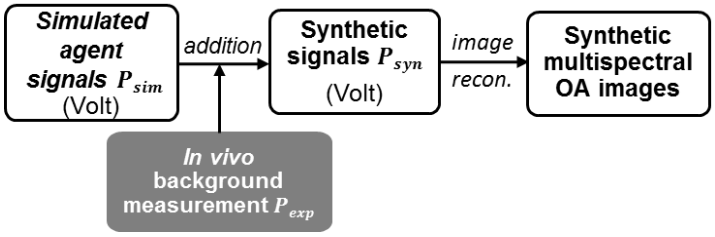

Figure 3.4. Schematic of target implantation. The simulated optoacoustic signals of an agent (output of Simulation Module) are superimposed onto experimental tissue signals from an in vivo animal measurement, giving rise to synthetic MSOT signals. After image reconstruction, synthetic MSOT images are generated. This figure is adapted from Ref. [75].

3.2.3 Molecular sensitivity calculation

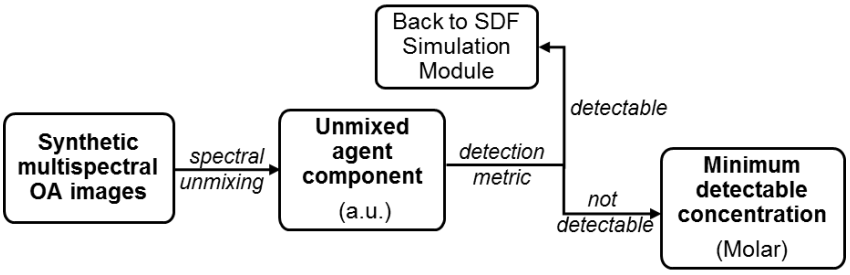

Figure 3.5. Schematic of the determination of MSOT molecular sensitivity. The synthetic MSOT images generated by SDF simulator are unmixed. Then a detection metric is applied to the unmixing result to define the detectability of the contrast agent until the minimum detectable concentration is defined. This figure is adapted from Ref. [75].

Figure 3.5 shows the derivation of MSOT molecular sensitivity based on the SDF simulator. To assess the molecular sensitivity of MSOT as a function of tissue depth, lesion size and contrast agent employed, we analyzed the reconstructed synthetic images produced by the target implantation module using an unmixing algorithm based on the adaptive matched filter (AMF) [74]. Our goal was to spectrally resolve the distribution of the agent from the absorbing background. The spectral unmixing result is a 2D image $D(\mathbf{x})$. In order to derive the minimum detectable concentration of the agent, a standard for defining an agent as 'detectable' should be established. In the present study, the agent is treated as 'detectable' if it can be distinguished from the background with only a moderate amount of false positives after unmixing [74], which can be expressed as

$$\sum_{\mathbf{x}\in D_a} D(\mathbf{x}) > \sum_{\mathbf{x}\in D_b \wedge D(\mathbf{x})>\overline{T}} D(\mathbf{x}), \qquad (3.9)$$

where D_a is the agent region and $D_b$is the background region, D_b=$D \setminus D_a$ and '\' denotes set subtraction, and $\overline{T}$ is the mean intensity of the agent region from the unmixing result D. According to the detection metric above, if the agent is detectable, the process restarts at the simulation module, this time with a lower input concentration. The iterations continue until the agent can no longer be detected. Then the lowest detectable concentration is defined as the molecular sensitivity.

3.3 Validation of SDF

To validate the SDF simulator, we performed experiments with two anesthetized CD1 mice *in vivo*, i.e. Group A and Group B in Table 3.1. For each animal experiment, a polyester capillary tube of inner diameter 0.8/1 mm was rectally inserted into the mouse. Then the mice were imaged at 21 wavelengths (from 700 nm to 900 nm with 10 nm interval) in the lower abdominal area. First, the animal was scanned with a water-filled tube in order to acquire the background signals for agent implantation (Experiments A1 and B1). Then for Group A experiments, the inserted tube was iteratively filled with 2 concentrations of ink (4.6 and 9 cm^{-1}) (Experiment A2) and 10 increasing concentrations of AF750 (0.12, 0.21, 0.35, 0.64, 1.22, 2.3, 4.6, 9.2, 16.1 and 23 cm^{-1}) (Experiment A3). For Group B experiments, the inserted tube was iteratively filled with distilled water (Experiment B1), 8 concentrations of ink (0.35, 0.58, 0.78, 1.52, 3.54, 4.49, 5.75 and 8.74 cm^{-1}) (Experiment B2) and 8 increasing concentrations of AF750 (0.28, 0.64, 0.74, 1.33, 2.78, 4.6, 9.2 and 13.8 cm^{-1}) (Experiment B3). For the *in vivo* experiments, the animals were anesthetized using 1.8% isoflurane (Forene©, Abbott AG, Switzerland) vaporized in 100% oxygen at 0.8 L/min. All animal procedures were approved by the Government of Upper Bavaria.

As a complement to the *in vivo* measurements in Experiments A2-3 and B2-3, we performed simulations using the SDF simulator, in which $\mu_a(\mathbf{x}, \lambda)$ in the agent region equals the absorptions. Four synthetic datasets were generated: Synthetic A2-3 and B2-3. To validate the simulation framework, the reconstructed synthetic images were compared to *in vivo* experimental images in two ways. First, the intensities of the agent region in synthetic and experimental optoacoustic images were compared in a process referred to below as 'intensity validation'. Second, the synthetic and experimental images were spectrally unmixed, and the minimum detectable AF750 concentrations determined from each set of images were compared. This process is referred to below as 'molecular sensitivity validation'. Table 3.1 summarizes key information about *in vivo* experiments performed with MSOT in the present study.

Table 3.1 Summary of in vivo experiments

Group	Expt. no.	Agent	No. of concs.	Purpose
A	1	none	0	Background signal for synthetic dataset
	2	India ink	2	Light fluence field estimation; intensity validation
	3	AF750	10	Intensity validation; sensitivity validation
B	1	none	0	Background signal for synthetic dataset
	2	India ink	8	Light fluence field estimation; intensity validation
	3	AF750	8	Intensity validation; sensitivity validation

Expt. no., experiment number; No. of concs., number of concentrations. This table is adapted from Ref. [75].

In order to validate the SDF, four synthetic datasets (Synthetic A2, A3, B2 and B3) were generated corresponding to Experiments A2, A3, B2 and B3 described in Section 3.3.1 and

3.3.2. We followed two different approaches for validation to demonstrate the agreement of the SDF with the real experiments in terms of image intensity and molecular sensitivity. In the first approach the image intensity of the agent region in synthetic images is compared to that of the experimental ones, while in the second approach the minimum detectable concentration after spectral unmixing is compared.

3.3.1 Intensity validation

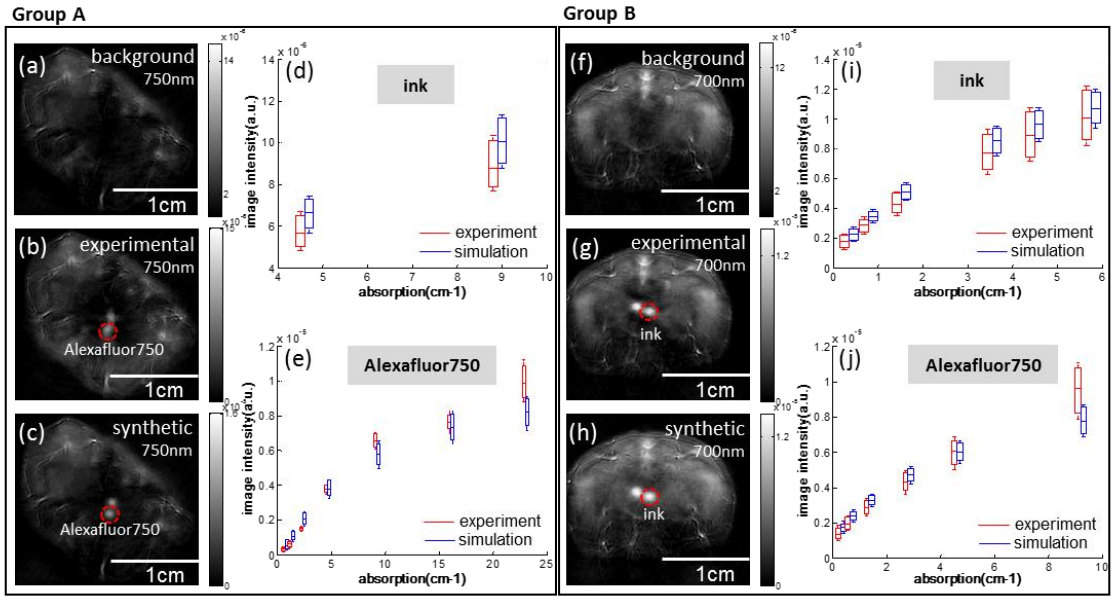

Figure 3.6. Comparison of the image intensity within the agent area between experimental and synthetic images. (a) Animal background image from Experiment A1; (b) experimental image with a 0.8-mm tube filled with 16.1 cm^{-1} AF750 at 750 nm (Experiment A3); (c) synthetic image with the simulated agent of the same absorption, location and size as the agent in panel (b); (d) quantitative analysis of image intensity within the agent area for Experiment A2 and Synthetic A2; (e) quantitative analysis of image intensity within agent area for Experiment A3 and Synthetic A3; (f) Group B animal background image (Experiment B1); (g) an experimental image of B2 with 1-mm tube filled with 5.75 cm^{-1} India ink at 700 nm; (h) synthetic image with the simulated agent of the same absorption, location and size as the agent in panel (g); (i) quantitative analysis of image intensity within agent area for Experiment B2 and Synthetic B2; (j) quantitative analysis of image intensity within agent area for Experiment B3 and Synthetic B3. All error bars stand for standard deviation. All scale bars are 1 cm. This figure is adapted from Ref. [75].

First the accuracy of the SDF by comparing the image intensity within the agent area was validated. Figure 3.6(a) – 3.6(e) correspond to the Group A experiments. Figure 3.6(a) presents the experimental background image (only the 750-nm image shown for simplicity) from the abdominal area of the animal in Experiment A1. Figure 3.6(b) presents the experimental image (in Experiment A3) in which the inserted tube containing AF750 at an absorption of 16.1 cm^{-1} is highlighted with a red circle. Figure 3.6(c) presents a synthetic image (highlighted as 'synthetic' in all figures) derived from the SDF simulator with the same absorption as Figure 3.6(b). Optoacoustic image intensities within the circled area for different concentrations of ink (Experiment A2 and Synthetic A2) and AF750 (Experiment A3 and Synthetic A3) are presented in Figure 3.6(d) and 3.6(e) with blue error bars, respectively.

Figure 3.6(f) – 3.6(j) correspond to the Group B experiments in Table 3.1. Figure 3.6(f) presents the background image (only the 700-nm image shown for simplicity) from the abdominal area of the second animal in Experiment B1. Figure3.6(g) presents the image from Experiment B2 with the tube containing 5.7 cm^{-1} ink. Figure 3.6(h) is formed using the background signals shown in Figure 3.6(f) and the simulated signals of the tube region with the same absorption as in Figure 3.6(g). The optoacoustic image intensities within the circled tube area for different ink (Experiment B2 and Synthetic B2) and AF750 concentrations (Experiment B3 and Synthetic B3) are presented in Figure 3.6(i) and 3.6(j), respectively.

From Figure 3.6(d), 3.6(e), 3.6(i), and 3.6(j), it can be seen that the mean and median intensities of the agent region accord well between experimental and synthetic MSOT images in most cases. Discrepancies in the intensity fluctuation range between experiments and simulations is due mainly to the manual segmentation of agent area in experimental images, which is unavoidable as there exists no prior information about the boundary of the agents.

3.3.2 Molecular sensitivity validation

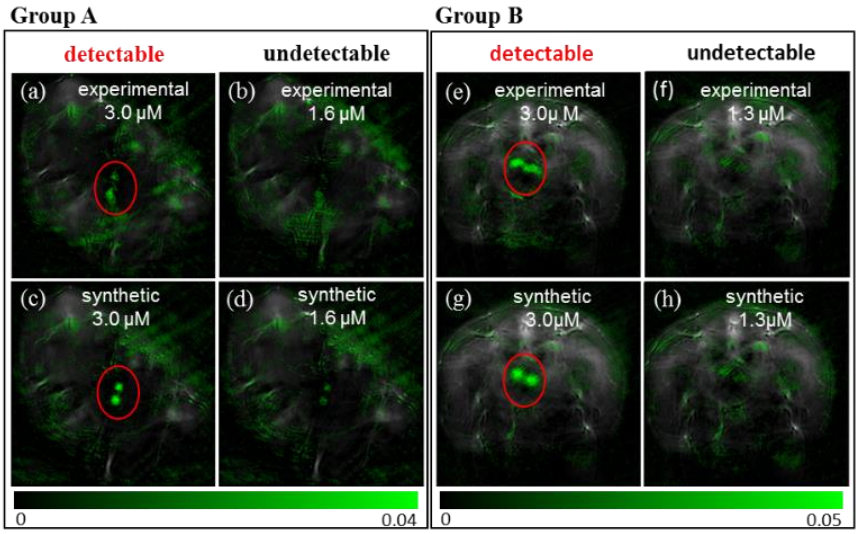

Figure 3.7. The minimum detectable concentration of AF750 after spectral unmixing in experimental and synthetic datasets. (a) Spectral unmixing result of Experiment A3 with 3.0 μM AF750; (b) spectral unmixing result of Experiment A3 with 1.6 μM AF750; (c) spectral unmixing result of Synthetic A3 at 3 μM; (d) spectral unmixing result of Synthetic A3 at 1.6 μM; (e) spectral unmixing result of Experiment B3 with 3 μM AF750; (f) spectral unmixing result of Experiment B3 with 1.3 μM AF750; (g) spectral unmixing result of Synthetic B3 with 3 μM AF750; (h) spectral unmixing result of Synthetic B3 with 1.3 μM AF750. This figure is adapted from Ref. [75].

Besides the intensity validation, spectral unmixing was also applied to the reconstructed images of Experiment A3, Synthetic A3, Experiment B3 and Synthetic B3 to verify the accuracy of the SDF. Figure 3.7(a) - 3.7(d) show the overlay of the spectral unmixing result of AF750 (green) and anatomical MSOT image (gray) from Experiment and Synthetic A3 datasets at respective concentrations of 3.0 and 1.6 μM. Figure 3.7(e) - 3.7(h) are the spectral unmixing results of AF750 from Experiment and Synthetic B3 datasets at concentrations of 3.0 and 1.3 μM. Figure 3.7(a) and 3.7(b) show two adjacent concentrations in Experiment A3, and 3.7(e) and 3.7(f) show two adjacent concentrations in Experiment B3. Based on the detection metric in Equation 3.9, the agent in Figure 3.7(a) and 3.7(e) are detectable, while

the agent in Figure 3.7(b) and 3.7(f) are not, which demonstrates that in this case the minimum detectable concentration of AF750 is about 3 μM. At the same time, the spectral unmixing results of corresponding synthetic datasets [Figure 3.7(c) - 3.7(d) and 3.7(g) - 3.7(h)] also show the same minimum detectable concentration in both cases. Comparing these two groups of unmixing results, it can be seen that the synthetic datasets provide the same minimum detectable concentration of AF750 as the experimental cases, which means that the developed simulation framework SDF can be used to determine the molecular sensitivity of MSOT.

3.4 SDF-based molecular sensitivity study

After the validation of the SDF, various agents were implanted at different depths and volumes into Experiment A1 background signals [experimental signals corresponding to Figure 3.6(a)], and MSOT molecular sensitivity was determined. Agents with distributions like disks with diameters of 1, 2 or 3 mm were separately implanted at seven imaging depths (1, 2.4, 3.8, 5.2, 6.6, 8 and 9.4 mm). At each imaging depth, 4 disks of the same diameter were implanted at different locations on the background to study molecular sensitivity variations at the same imaging depth; such variations should reflect mainly heterogeneity in the background. Figure 3.8(a) and 3.8(b) show that 4 agents with diameters of 2 and 3 mm at 1 mm depth are detected, respectively. Figure 3.8(c) and 3.8(d) are the molecular sensitivity curves of AF750 and GNRs, respectively. Both panels show that the minimum detectable concentration increases with depth of the agent and decreases with agent size. For each agent size, molecular sensitivity to AF750 and GNRs varies at every depth, reflecting the heterogeneity of background tissue. For example, in Figure 3.8(a) and 3.8(b), four agents on the same image are of the same depth and size, but the agent on the bottom is much more difficult to detect than the other three agents. In other words, with the same depth and lesion size, the minimum detectable concentration of the bottom agent is much higher than the other three agents, which introduces standard deviation into the curve. Agent at the bottom was difficult to detect because of the strongly absorbing vessel (highlighted with a red arrow on the images) and the 270-degree transducer coverage. Since the synthetic signal P_{syn} is generated by superimposing the simulated optoacoustic signal of the contrast agent P_{sim} onto the experimental background signal P_{exp}, i.e. $P_{syn} = P_{sim} + P_{exp}$, the presence of strong non-homogenous intrinsic absorber (such as blood vessels) in the background makes the background signal dominate the synthetic signal. In this case, the unmixing algorithm detects the main absorber at that location as hemoglobin and fails to detect the contrast agent. Additionally, the coverage angle of the transducer array is only 270 degrees and does not cover the central bottom part of the image. Therefore, signal from that region is slightly weaker than the signal from other regions. The molecular sensitivity curve also fluctuates because the sensitivity metric (shown in Equation 3.9) is related to agent location and size. Comparing panel 3.8(c) and 3.8(d), we can see that MSOT can detect gold nanorods with nanomolar molecular sensitivity, which is much higher than micromolar molecular sensitivity to AF750.

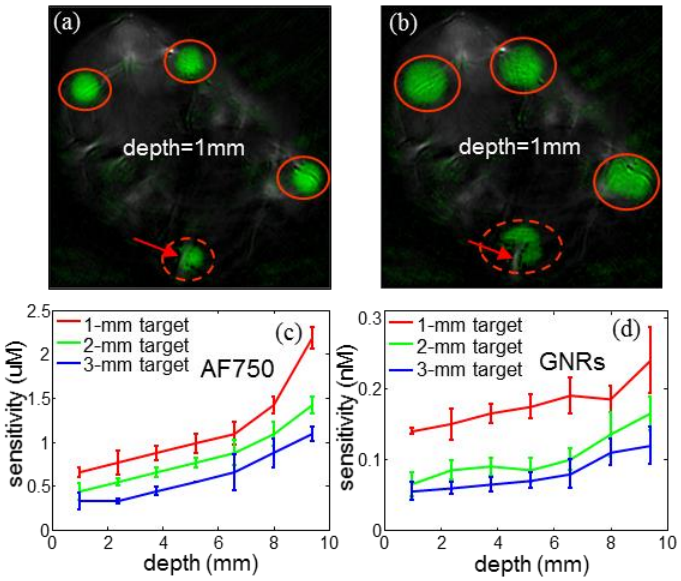

Figure 3.8. Molecular sensitivity curves of AF750 and GNRs as a function of depth with agents showing disk-like distributions with diameters of 1, 2 or 3 mm. (a) Spectral unmixing result for an agent with diameter of 2 mm at a depth of 1 mm; (b) spectral unmixing result for an agent with diameter of 3 mm at a depth of 1 mm; (c) molecular sensitivity to AF750 as a function of imaging depth for agents with diameters of 1, 2 or 3 mm; (d) molecular sensitivity to GNRs as a function of imaging depth for agents with diameters of 1, 2 or 3 mm. All error bars stand for standard deviation. This figure is adapted from Ref. [75].

Figure 3.9 shows another example of using the SDF to estimate molecular sensitivity of AF750 in blood-rich/pigment-rich organs such as liver. In this simulation, the coefficient of optical properties of the liver is referred to published studies: absorption, 0.6 cm^{-1} [85], scattering, 7.5 cm^{-1} [86] and the oxygen saturation, 85% [87]. The optical properties of the superficial tissue surrounding the liver are assumed as absorption, 0.1 cm^{-1}, scattering, 10 cm^{-1} and oxygen saturation, 80%.

Figure 3.9(a) is a cross-sectional image of the liver region at 750 nm. The intensity decreases dramatically from the surface to the center, due mainly to attenuation of light fluence with increasing depth, which is shown in Figure 3.9(b). Figure 3.9(c) shows the unmixing results at a depth of 2.4 mm and concentration of 0.93 μM overlaid onto the background image. Figure 3.9(d) shows the molecular sensitivity of AF750 as a function of imaging depth for agents with a diameter of 2 mm.

The result shows that the molecular sensitivity to AF750 is 6× higher (meaning lower injection concentration required) in the abdominal region (1 μM, Figure 3.8) than in the liver region (6 μM, Figure 3.9) for the 2-mm target size and 8-mm depth, which is due mainly to the strong absorption in liver. Since light absorption is much higher in blood-rich/pigment-rich organs than in abdominal tissue, light fluence is attenuated much more in these organs. In other words, after propagating the same distance, much less light energy arrives at the location of the contrast agent, which is demonstrated by comparison of Figure 3.5(c) and Figure 3.9(b). Approximately 40% of light energy arrives to a depth of 1 cm in the abdominal region, while only 5% reaches the same depth in the liver region. The dramatic decrease of light energy leads to a relatively lower SNR of the optoacoustic signals, which as expected

lowers the molecular sensitivity and consequentially requires high AF750 injection concentration for imaging in this region.

Furthermore, MSOT molecular sensitivity to AF750 is lower in the liver region for a second reason. The optoacoustic spectrum of the contrast agent extracted from multi-spectral optoacoustic images is the combination of the absorption spectrum of the agent and the light fluence spectrum arriving at that location, which is termed spectral coloring. When the light fluence spectrum is flat, the signature of the optoacoustic spectrum is the same as the absorption spectrum. However, in hemoglobin-rich organs such as liver, the light fluence spectrum is strongly distorted by the absorption of the hemoglobin/pigment in the pathway of the light. Therefore, the signature of the optoacoustic spectrum turns to be very different from the absorption spectrum of the contrast agent due to such spectral coloring effect. This makes spectral unmixing difficult for liver imaging and thus requires relative high concentration of exogenous contrast agents. Similar conclusion can also be applied to other contrast agents and target sizes in other hemoglobin-rich organs, such as spleen and kidney.

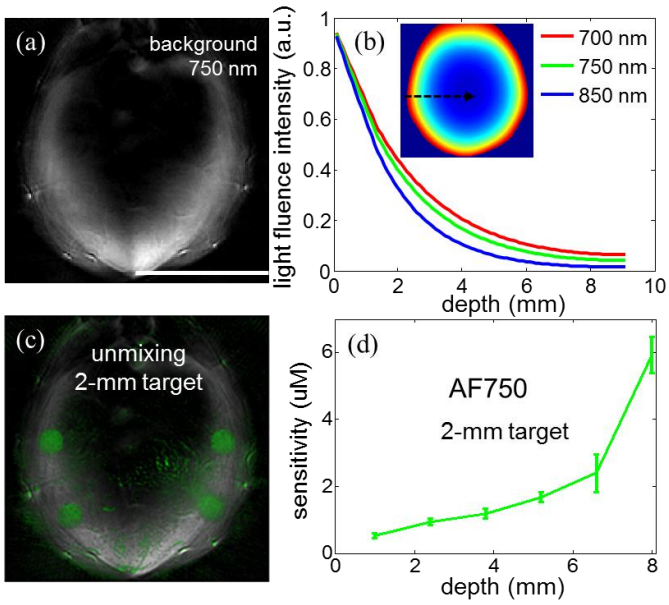

Figure 3.9. Molecular sensitivity curve of AF750 in the liver region as a function of depth with agents showing disk-like distributions with a diameter of 2 mm. (a) In vivo background image. (b) Light fluence profile from surface to center within the background. (c) Spectral unmixing result of synthetic data at 0.93 μM. (d) Molecular sensitivity of AF750 as a function of imaging depth for agents with a diameter of 2 mm. Error bars indicate standard deviation.

3.5 Discussion and outlook

In this study, a new synthetic data framework is developed to systematically assess the molecular sensitivity of MSOT. The synthetic data generated using this technique are compared against controlled *in vivo* experiments and show good agreement. For the first time, a framework can predict MSOT molecular sensitivity as a function of lesion size, imaging depth and agent type, including fluorescent dyes and photo-absorbing nanoparticles.

The SDF developed in this study is able to generate realistic synthetic MSOT data mainly because it uses experimental measurements for tissue background signal determination and a calibrated agent implantation method. The concept of agent implantation has previously been used [39, 71, 74] to compare the performance of different spectral unmixing algorithms. However, in those previous studies, only the relative agent intensity was of interest, and therefore, the intensity of the implanted agents was not accurate in an absolute sense. That work was substantially expanded in the present study because we included a number of additional system parameters (SIR, EIR), physical effects (ultrasound attenuation) and calibration parameters (light fluence, Grüneisen coefficient) into our simulation in order to achieve accurate simulated agent intensities. Furthermore, instead of superimposing the image of simulated agents onto the background tissue image, we merged the simulated optoacoustic signals of agents with the experimental MSOT signals of background tissue before image reconstruction. This approach generates more realistic synthetic MSOT images.

The molecular sensitivity of MSOT depends on a multitude of parameters: (1) characteristics of the contrast agents employed, i.e. the molar extinction coefficient, Grüneisen coefficient and the absorption spectrum; (2) the agent location within tissue (tissue depth); (3) the size of the lesion occupied by the agent; (4) the optical properties and overall characteristics of the imaged tissue; (5) the specifications of the imaging system and (6) the image reconstruction and spectral analysis method used. These parameters affect the molecular sensitivity of MSOT in two ways. One way is via the optoacoustic signal intensity generated by the absorber. The molecular sensitivity is affected by the relative intensity between the signal from an agent and the signal from background absorbing tissue. The amplitude of the signals depends, in turn, on its optical and thermal properties (absorption and Grüneisen coefficients) and on the light fluence reaching the agent. These considerations mean that agents showing higher absorption and Grüneisen coefficients [88] can be detected with greater molecular sensitivity, and that the same agent can be detected with different molecular sensitivities at different locations or laser powers [89]. The second way is that different spectral unmixing algorithms differ in their ability to detect and quantify the absorbers of the same relative signal intensity against the absorbing tissue background. For example, statistical sub-pixel detection methods offer 5-fold greater molecular sensitivity than linear unmixing approximations [39, 74]. The performance of spectral unmixing algorithms depends, in turn, on the absorption spectrum signature of the agent and the illumination wavelength(s). A contrast agent with a distinct absorption peak (e.g. AF750) is easier to detect than an agent with a flat spectrum signature (e.g. India ink). Molecular sensitivity can increase by an order of magnitude simply by moving from single- or dual-wavelength to multi-wavelength illumination.

Since the molecular sensitivity of MSOT is affected by numerous parameters as mentioned above, the reported values in literature vary substantially across different studies. For example, among all studies performed with dyes and gold nanorods, the Vevo LAZR system (VisualSonics, Toronto, Canada) was reported to detect 5 nM gold nanorods beneath the skin layer for assessing protease activity in colorectal cancer [90]. The LOUIS-3D system (TomoWave Laboratories, Houston, USA) was reported to achieve molecular sensitivity of ~50 μM to ICG in tissues with relatively low blood content [89]. The Nexus 128 system (Endra Life Sciences, Ann Arbor, USA) detected a cellulose-based nanoparticle with a detection limit of 6 pM in vitro and 0.35 nM *in vivo* [36], or gold nanorods with a limit of 0.40 nM in ovarian

cancer cell line 2008 and a limit of 24 pM *ex vivo* [38]. In studies with the same MSOT inVision256 system used in this work (iThera Medical, Munich, Germany), ~10 μM AF750 was injected into the pelvic limb of euthanized wild-type mice, approximately 5 mm below the knee joint, in order to reveal functional and molecular information [18]. The same system detected 0.6 mM Lipo-ICG within the tumor microenvironment [29]. In addition to these commercial systems, molecular sensitivity of in-house optoacoustic systems has been reported. Optoacoustic molecular imaging has been reported with sensitivities of 5 nM for ICG in phantoms [30], ~10 μM in the blood stream *in vivo* [31] and ~129 μM within chicken muscle at a depth of 5.2 cm [32]. Another system has shown sensitivity of 5 μM for IRDye800-c(KRGDf) at a depth of ~2 mm in chicken tissue [28]. Gold nanorods at a concentration of 50 pM have been visualized in rat tail joints [91]. These results are summarized in Table 3.2.

Table 3.2 Summary of reported molecular sensitivities with nanorods and dyes

system name	contrast agent applied	detected concentration	experiment type	Ref.
Vevo LAZR	gold nanorods	5 nM	*in vivo*	[90]
Nexus 128	cellulose-based nanorods	6 pM	in vitro	[36]
		0.35 nM	*in vivo*	[36]
	gold nanorods	0.4 nM	in vitro	[38]
		24 pM	ex vivo	[38]
in-house system University of Michigan	gold nanorods	50 pM	*in vivo*	[91]
MSOT inVision256	AF750	~10 μM	*in vivo*	[18]
	Lipo-ICG	0.6 mM	*in vivo*	[29]
LOUIS-3D	ICG	~50 μM	*in vivo*	[89]
in-house system OptoSonics, Inc.	ICG	5 nM	phantom	[30]
in-house system Texas A&M University	ICG	~10 μM	*in vivo*	[31]
		~129 μM	ex vivo	[32]
in-house system National Tsing Hua University	IRDye800-c	5 μM	ex vivo	[28]

AF750 = Alexa Fluor 750; ICG = indocyanine green. This table is adapted from Ref. [75].

The results of our SDF-based molecular sensitivity study indicate that the minimum detectable concentration of AF750 lies in the lower micromolar (< 2 μM) to upper nanomolar (> 200 nM) scale, depending on the agent size and imaging depth. Conversely, in the case of GNRs, the molecular sensitivity lies in the range of 200 pM to 50 pM. These sensitivities predicted by the SDF in our study appear consistent with the *in vivo* experiments and are comparable to, or better than, values previously reported for dyes and GNRs. The molecular sensitivity determined here was higher than in some previous studies probably because of the use of multi-wavelength imaging and spectral unmixing techniques, which can increase MSOT molecular sensitivity by an order of magnitude [39]. We also note that, as the interested target and tissue/animal differs in each molecular imaging application, the molecular sensitivity of a given system for potential contrast agent varies. Thus, the SDF-based method is hereby proposed to derive molecular sensitivity under different optoacoustic molecular imaging scenarios. As the molecular sensitivity numbers predicted by the SDF-based study appear consistent with physical experiments, these numbers can be

used as a reference for the minimum amount of contrast agent that should be injected in MSOT studies.

The SDF development is here focused on MSOT, but the framework could also be used in the context of other state of the art optoacoustic imaging systems for identifying their molecular imaging sensitivities to varied contrast agents in future applications. In the simulation module (Figure 3.2), the properties of the transducer (e.g. the EIR, SIR, conversion factor) are taken into account and the geometrical parameters of the transducer array (e.g. concave design as well as radius, focal length and coverage angle of the array) are incorporated into the model matrix M. As these parameters are easily adjustable, the SDF could be adapted for other imaging systems to estimate the molecular sensitivity. The SDF is also suitable for (pre)clinical studies with various tissue types, such as hypoxic tissue. In this case, the sO2 needs to be changed during the estimation of light fluence in Simulation Module.

The simulation framework discussed in this paper can predict MSOT molecular sensitivity without the need for extensive animal experiments. It provides reliable estimates of concentrations of contrast agents required for MSOT experiments. Nevertheless, the influence of each factor (e.g. system hardware components, spectral unmixing algorithm, signal processing and imaging processing method) in attaining certain molecular sensitivity in MSOT imaging can be quantitatively analyzed with this simulation framework, since all those factors are independent and easily adjustable in the SDF, which is infeasible with physical experiments. This offers the possibility for further improvement of MSOT. To allow accurate simulation of all kinds of agents, a more accurate light fluence model to simulate a more complex light distribution within a large, strong absorber should be developed.

In this chapter, a novel simulation framework including all effects in MSOT imaging was developed and the accuracy of this method was demonstrated with controlled *in vivo* experiments. Using this framework, we estimate the molecular sensitivity of MSOT for fluorescent dyes (AF750) and GNRs as a function of agent size and imaging depth. With this method, MSOT molecular sensitivity can be systematically predicted in order to optimize the type and concentration of contrast agent for MSOT studies. Having those molecular sensitivity numbers as a reference, the minimum concentration of injected contrast agents can be decided before performing MSOT imaging. This can save time and resources as well as improve animal welfare by offering more insightful information during the experimental design stage. This framework will also be useful as a tool to study the effect of each parameter in Equation 3.6 on MSOT molecular sensitivity, which will allow systematic studies to improve MSOT performance.

Section II: Studies of image reconstruction in handheld optoacoustic and ultrasound (OPUS) imaging

4. Characteristics and operation of the OPUS system

4.1 The probe designs of OPUS systems

As introduced in Chapter 1, since the only way to make MSOT practical in clinics is to develop a handheld device, a probe similar to that used in clinical B-mode ultrasound imaging is needed in clinical MSOT, which means less coverage angle for both illumination and detection. The change in detection and illumination from preclinical to clinical MSOT imposes a series of unique challenges for image reconstruction. To bypass the challenges, the combination of MSOT with other imaging modality, especially the combination with ultrasound, i.e. OPUS is a popular way.

Among all reported OPUS systems, two implementation strategies of the probe have been used. The first and most straight-forward strategy to combine optoacoustic and ultrasound is using a commercial ultrasound probe of a linear-array or a convex transducer array for ultrasound wave detection in both modalities and adding optical fibers on the side of the probe to guide the laser beam for the illumination in optoacoustic imaging [46, 92-95]. The second strategy is to use a cylindrically focused concave transducer array for both optoacoustic and ultrasound imaging [96, 97]. The major difference between these two methods is the choice of transducer type and geometry of the array. In order to understand the advantage and disadvantage of each design, the main difference of ultrasound detection in ultrasound imaging and optoacoustic imaging needs to be clarified.

In conventional pulse-echo mode ultrasound imaging, the probe is normally a linear or convex ultrasound array which composes of multiple flat acoustic transducer elements. These elements are of small size and densely placed to meet the spatial sampling theorem, that is, the pitch size should be ideally less than half a wavelength [98]. This sampling theorem is mainly to confine the pulse energy in the main beam and prevent the occurrence of grating lobes or side lobes which are caused by sound energy that spreads out from the transducer at angles outside the electronically driven direction [97]. The energy in grating lobes can interact with the specimen in the same way as the main beam, and thus generate echoes causing spurious indications on an ultrasound image and interference to the inspection.

For clinical optoacoustic imaging, ultrasound waves, which are broadband and non-directional [13], are generated by the thermo-expansion of optical absorbers in the tissue. Based on this mechanism, a concave transducer array is normally used to fulfill a tomographic detection of ultrasound signals with multiple focused transducer elements. The concave geometry of the array is to assure a large coverage angle to the specimen which is necessary for the reconstruction of spherical waves source [99]. The choice of focused transducer is due to the fact that the ultrasound wave in optoacoustic imaging is generated from light absorption and light scattering is strong inside tissue, the sources of ultrasound signals are located in a large volume of specimen and focused transducer elements are needed to choose the imaging plane [97]. Meanwhile, the amplitude of optoacoustic signals is relatively weak,

therefore large element size is preferred in optoacoustic imaging to enable high detection sensitivity [96].

Back to the comparison of the two implementation strategies of hybrid OPUS probes, although the first strategy, i.e. a commercial ultrasound probe with the addition of laser bundles on side, is easy to implement from the hardware point of view, some studies have already demonstrated that it results in obvious limited-view artifacts and poor optoacoustic image quality [100], because the coverage angle of the probe and small pitch designs provide insufficient recording of optoacoustic signals [4, 101]. Meanwhile, for the second strategy, i.e. a concave array with large element size, it is mainly optimized for optoacoustic detection and due to the large element size (larger than half a wavelength), grating lobes are inevitable and put higher requirement for imaging technique, signal processing and image processing to get rid of the artifacts introduced by grating lobes. Therefore, those two strategies should be carefully chosen based on the focus of applications.

4.2 Operation principles of the experimental OPUS system – Acuity256

Since commercial linear array has been demonstrated inefficient in optoacoustic imaging and results in poor optoacoustic image quality [97] and concave array has been demonstrated to be able to generate adequate ultrasound image quality using synthetic aperture technique and spatial compounding to reduce the effect of the grating lobes [61, 96, 97], a hybrid OPUS system with a probe using the second implementation strategy, such as the commercially available Acuity256 system (iThera Medical GmbH, Munich, Germany), is of major interest in this dissertation. All clinical studies in this dissertation are carried out with a customized Acuity256 system.

The customized OPUS system is of a handheld probe which uses a concave transducer array for both optoacoustic and ultrasound imaging. As pulse-echo mode ultrasound and optoacoustic imaging have opposite requirement on transducer element size and pulse-echo ultrasound image quality is sensitive to pitch size, the customized OPUS system uses a compromise value of pitch size, which is 0.59 mm (i.e. 1.9λ assuming the speed of sound 1530 m/s). The transducer array of the system comprises 256 cylindrically focused transducer elements (of 4 MHz central frequency and 60 mm focal length) and 145°angular coverage with heavy water as the coupling medium, as Figure 4.1(a) shown. For optoacoustic imaging, a 25 mJ laser pulse (of 10 ns duration) is emitted at 25 Hz repetition rate to excite the sample. Generated optoacoustic waves are detected by all the transducer elements as Figure 4.1(b) shows. Figure 4.1(c) illustrates the operation of ultrasound module in the customized Acuity256 system. Under the ultrasound module, each of the transducer elements is activated to generate an ultrasound pulse sequentially and half of the transducer array are activated to detect the reflected ultrasound echoes after each pulse being generated. More information about ultrasound module will be introduced in Chapter 6.

For the synchronization of optoacoustic module and ultrasound module, the laser pulse is used as the trigger of the acquisition of both modalities. Figure 4.1(d) shows the operating protocol used in the handheld OPUS system. When the laser pulse is emitted, the optoacoustic module is activated immediately to acquire optoacoustic signals and perform reconstruction, which takes about 10ms. After a delay of ~10ms, ultrasound module is activated to acquire signals for ~26 ms and perform reconstruction approximately 110 ms. As a result, within the

time of the acquisition and reconstruction of one ultrasound frame, multiple optoacoustic frames are acquired and reconstructed. Due to the use of a common detector and the synchronization procedure, the acquired optoacoustic and ultrasound images using such an OPUS system can be accurately co-registered if no movement is introduced from outside.

As the magnitude of ultrasound echoes is normally several orders of magnitude higher as compared to optoacoustic signals [4], the used OPUS system utilizes two different data acquisition system for optoacoustic and ultrasonic signals acquisition. Both optoacoustic and ultrasonic signals are reconstructed with back projection algorithm in real-time to display on the screen during the measurements. At the same time, the reconstructed images and raw ultrasound and optoacoustic signals can be saved for each scan.

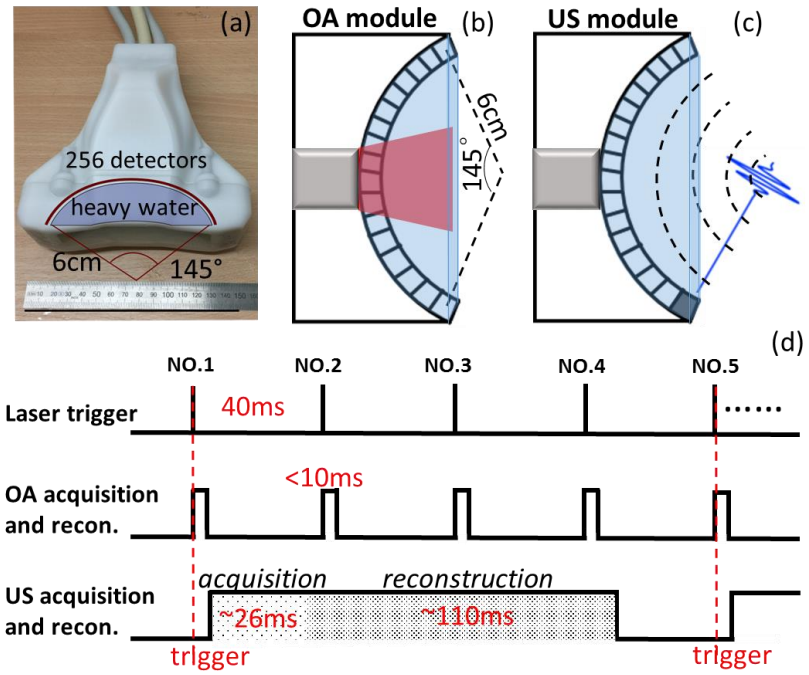

Figure 4.1. The hybrid OPUS imaging system and dual-modality operating procedure. (a) Photograph of the scanning head. (b) Schematic of the OA module in the scanning head. (c) Schematic of the US module in the scanning head. (d) Timing diagram of Acuity. OA: optoacoustic; US: ultrasound.

5. Dual-Speed-of-Sound (SoS) model-based optoacoustic reconstruction

5.1 Motivation

As introduced in Chapter 2.2, in most optoacoustic reconstructions, the imaging medium is normally assumed to be acoustically homogeneous and the SoS in imaged region to be therefore invariant, enabling the derivation of a closed-form solution to the acoustic wave equation [64]. However, this assumption leads to visible artifacts on the image when the variation of the SoS in the imaged region is around 10% [103]. It might not introduce too many errors with uniform SoS assumption in small-animal studies, since water or ultrasound gel is normally used as coupling medium and of similar SoS to the SoS of the tissue of mice. However, in some clinical studies which aim to image biological chromophores whose absorption peak appears between 850 nm to 1000 nm like lipids and proteins [104], water cannot be used as coupling medium. Instead, heavy water is used as coupling medium for handheld OPUS system [105] since light absorption is much lower in heavy water than in water at wavelengths >900 nm [106]. The new coupling medium does enable many interesting clinical studies, e.g. fatty tumors has been successfully image with an optoacoustic imaging set-up with heavy water as coupling medium to demonstrate the potential of handheld optoacoustic tomography in the diagnosis and evaluation of subcutaneous soft-tissue masses [104]. Simultaneous imaging lipid and hemoglobin while also determining oxygen saturation, which is required for many cardiovascular and oncological applications [107, 108] is also achieved with a handheld optoacoustic system with heavy water as the coupling medium.

In such cases, the SoS variation between coupling medium and tissue is larger than 10% and can introduce strong artifacts in reconstructed images, which might hinder the proper interpretation of the optoacoustic images. Therefore, we developed a dual-SoS model-based reconstruction to account for the SoS variation between coupling medium and the specimen, aiming to improve the quality of reconstructed images.

5.2 Dual-SoS model-based optoacoustic reconstruction

The reconstruction artifacts induced by uniform SoS model have attracted increasing attention in recent years. Previous work has shown that uniform SoS can introduce localization errors, reconstruct absorbers with inaccurate dimensions, and decrease the maximal resolution of the recovered image [106]. Other studies have described additional artifacts such as smearing and deformation of absorbers due to the assumption of constant SoS, and these artifacts are difficult to reduce using post-processing schemes [109, 110]. All these studies have focused on image intensity artifacts in single-wavelength optoacoustic

data. Much less understood is the impact of uniform SoS reconstruction on the spectra of multiple chromophores in multi-spectral optoacoustic data. It is likely that the impact of such artifacts on multi-spectral optoacoustic imaging is underestimated, and that they can hinder quantitative analysis of reconstructed spectral information [8], such as the analysis of endogenous chromophores such as lipids and proteins [78].

Therefore, in this section a dual-SoS model is developed for handheld optoacoustic tomography to consider the SoS variation between coupling medium and sample, with an emphasis on the reduction of spectral artifacts contributed by dual-SoS model comparing to the uniform SoS model. The analysis is based on the multi-spectral optoacoustic images of a phantom and human tissue *in vivo*, allowing us to develop and evaluate a dual-SoS model that can assign different SoS values in heavy water and the sample.

Since model-based schemes can explicitly take experimental characteristics into account and offer superior accuracy and image fidelity [65, 69], therefore, we develop our dual-SoS reconstruction under the scheme of model-based reconstruction by extending the algebraic reconstruction technique type model-based reconstruction using IMMI (Chapter 2) [65] and angular discretization strategy [69] to include different SoS.

5.2.1 Methods

When the SoS difference between coupling medium and sample is considered (dual SoS), the solution to optoacoustic wave equation (Equation 2.10) needs to be rewritten, i.e. the pressure distribution at $\boldsymbol{r}$ and t (Equation 2.11) in this case is rewritten as:

$$p(\mathbf{r},t)=\frac{\Gamma}{4\pi c_1}\int_{L_1(t)}\frac{H(\mathbf{r}')}{|\mathbf{r}-\mathbf{r}'|}d\mathbf{r}'+\frac{\Gamma}{4\pi c_2}\int_{L_2(t)}\frac{H(\mathbf{r}')}{|\mathbf{r}-\mathbf{r}'|}d\mathbf{r}', \qquad (5.1)$$

where $L_1(t)=\{\mathrm{r'}\in \mathrm{R}^3 \mid |\mathrm{r}-\mathrm{r'}| = c_1\mathrm{t}\}$, $L_2(t)=\{\mathrm{r'}\in \mathrm{R}^3 \mid |\mathrm{r}-\mathrm{r'}| = c_2\mathrm{t}\}$, c_1 and c_2 are the SoS in coupling medium and tissue sample in this section, respectively. The integral is split into two domains (coupling medium and tissue), assuming that wave equation is linear with respect to SoS variation and discretize Equation 5.1 as

$$\boldsymbol{p}=\mathbf{M}_{dual}\boldsymbol{x} \qquad (5.2)$$

where $\mathbf{M}_{dual}$ is the model matrix with dual SoS. The inversion of Equation 5.2 can be achieved as,

$$\boldsymbol{x}_{sol}=arg\min_{\boldsymbol{x}}\|\boldsymbol{p}_{det}-\mathbf{M}_{dual}\boldsymbol{x}\|^2+\lambda\|\mathbf{L}\boldsymbol{x}\|^2. \quad (5.3)$$

The computational complexity of Equation 5.3 and 2.15 is the same, i.e. the dual-SoS reconstruction can contribute to more accurate results than uniform SoS reconstruction without increasing computational cost.

In order to compare the spectral performance between the two different reconstruction schemes (uniform SoS and dual SoS), spectral similarity $S(\mathbf{I_i},\mu_a)$ between the normalized optoacoustic intensity spectrum in each pixel $\mathbf{I_i}$ and the normalized absorption spectrum of target chromophore $\mu_a$is calculated [111]:

$$S(\mathbf{I_i},\mu_a)=-\|\mathbf{I_i}(\lambda)-\mu_a(\lambda)\|_2^2 \qquad (5.4)$$

5.2.2 Optoacoustic imaging of phantoms and human tissue with Acuity256

The efficiency of dual-SoS reconstruction was evaluated using the experimental data of a phantom and a healthy volunteer, which were scanned using Acuity256 with 28 wavelengths from 700 nm to 970 nm with 10 nm interval. The phantom is with three plastic tube insertions and shown in Figure 5.1(a). The background of the phantom is made with a mixture of agar, distilled water and intralipid and the tubes contain indocyanine green (ICG, $\mu_a(750nm) = 2.1$ cm-1), Alexafluor750 (AF750, $\mu_a(750nm) = 4.2$ cm-1) and Indian ink ($\mu_a(750nm) = 3.9$cm-1) solution, respectively. Therefore, SoS inside the phantom is close to the SoS in water, i.e. approximately 1500m/s while the SoS in coupling medium is around 1400 m/s, i.e. the SoS of heavy water [105]. The absorption spectra of ICG, AF750 and ink were measured with a spectrometer and plotted in Figure 5.1(b). Further the spectral efficacy of the proposed reconstruction was studied with *in vivo* measurements, to this end the forearm and frontal neck regions of a healthy volunteer were imaged. Procedures on human subjects were performed after obtaining their written informed consent.

5.2.3 Results

In this section, the reconstruction results of the phantom and human tissue based on Equation 5.3and 2.15 are presented. The difference of the reconstruction results between these two methods are compared and the improvement from dual-SoS model is highlighted.

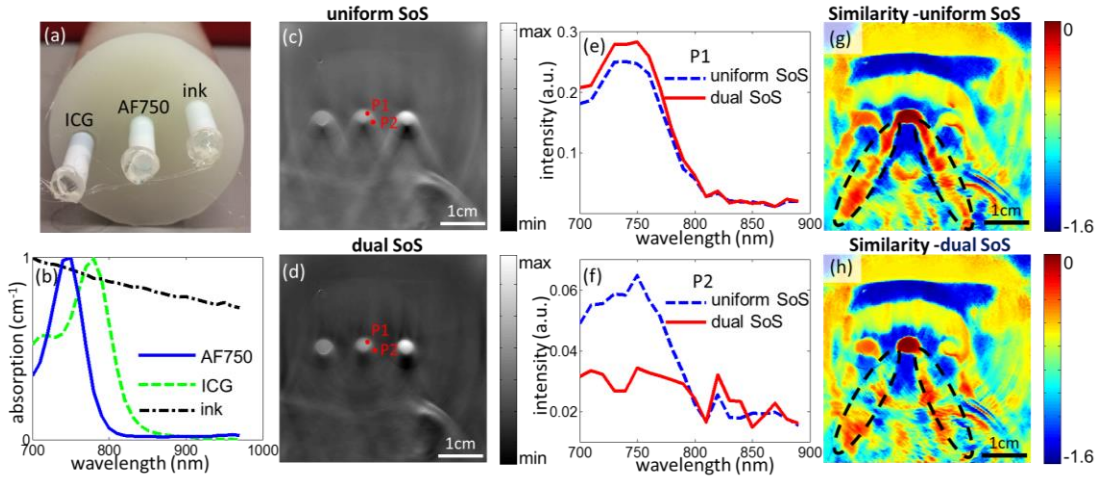

Figure 5.1. Comparison of phantom reconstruction assuming uniform SoS or dual-SoS. (a) Photograph of the imaged phantom. (b) Absorption spectra of imaged chromophores. (c) Reconstruction of the phantom assuming uniform SoS at 700 nm. Red dots indicate the areas (~15 pixels) whose spectra are shown in panels (e) and (f). (d) Reconstruction of the phantom assuming dual-SoS at 700 nm. Red dots indicate the areas whose spectra are shown in panels (e) and (f). (e) Reconstructed spectra at P1 in panels (c) and (d). (f) Reconstructed spectra at P2 in panels (c) and (d). (g) Similarity between the spectrum at each pixel in panel (c) and the spectrum of AF750 in panel (b). (h) Similarity between the spectrum at each pixel in panel (d) and the spectrum of AF750 in panel (b). This figure is adapted from Ref. [102].

Figure 5.1 evaluates and compares reconstructions of the phantom carried out assuming uniform SoS (Equation 2.15) or dual SoS (Equation 5.3). Figure 5.1(c) shows anatomical deformation with assumption of uniform SoS, consistent with previous studies [103, 109].

Figure 5.1(d) shows that using dual-SoS model reduces the deformation, allowing the signal to converge to a circular structure. To compare the two SoS approaches in greater detail, Figure 5.1(e) plots the mean intensities of a small region inside the middle tube (indicated as P1) as a function of wavelengths, while Figure 5.1(f) plots the mean intensities outside the tube (indicated as P2). As the tube in the middle contains AF750 solution, the spectrum of P1 should be similar to the absorption spectrum of AF750 shown in Figure 5.1(b). In contrast, the spectrum of P2 should not bear any resemblance to the AF750 spectrum, since P2 is a background region containing primarily water, which absorbs negligibly below 900 nm. Figure 5.1(e) shows that reconstruction assuming either uniform or dual-SoS recovers the AF750 spectrum in P1. Figure 5.1(f) indicates that only dual-SoS reconstruction accurately gives a noisy spectrum at P2, whereas uniform SoS reconstruction shows a spectral signature similar to AF750. In other words, assuming uniform SoS causes "spectral smearing" in which spectral information of an absorber smears over neighboring regions.

Figure 5.1(g) shows spatial analysis of this spectral smearing by quantifying the similarity between the spectrum observed in Figure 5.1(c) and the absorption spectrum of AF750: spectral similarity is greatest in the middle tube containing AF750, and the smearing extends to the very bottom of the image to form two obvious smearing 'tails' [dashed ellipses in Figure 5.1(g)]. Figure 5.1(h) shows that with dual-SoS reconstruction, spectral similarity values are highest only in the middle tube, and smearing 'tails' are largely eliminated. Comparing Figure 5.1(g) and 5.1(h) indicates that uniform SoS reconstruction can cause extensive spectral smearing even when it is less obvious in the single-wavelength images, and that this smearing can be drastically reduced by modeling the SoS variation between heavy water and sample.

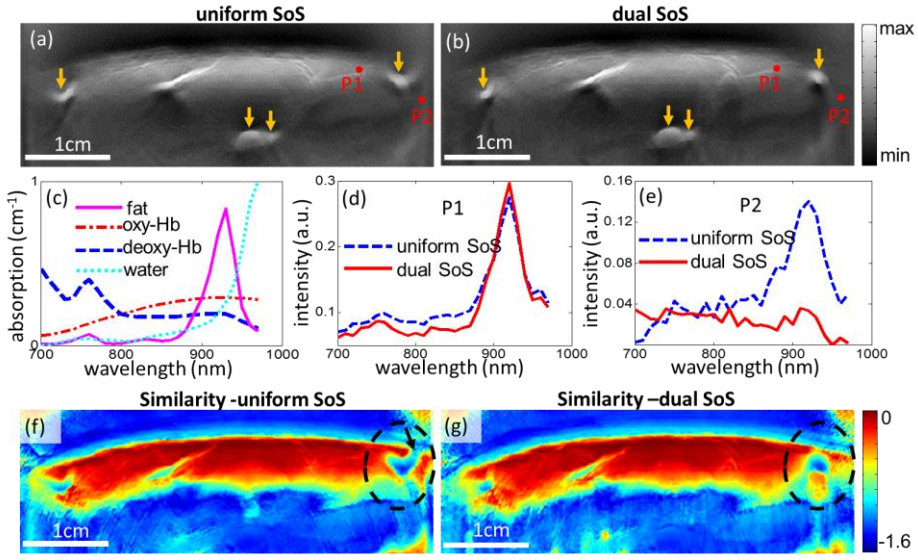

Figure 5.2. Comparison of image reconstruction of human forearm assuming uniform SoS or dual-SoS. (a) Reconstruction assuming uniform SoS at 930 nm. Red dots indicate the area (~ 15 pixels) whose spectra are shown in panels (d) and (e), and yellow arrows indicate blood vessels. (b) Reconstruction assuming dual-SoS at 930 nm. (c) Absorption spectra of four endogenous chromophores in tissues [112]. (d) Reconstructed spectra at P1 in panels (a) and (b). (e) Reconstructed spectra at P2 in panels (a) and (b). (f) Similarity between the spectrum at each pixel in panel (a) and the spectrum of fat in panel (c). (g) Similarity between the spectrum at each pixel in panel (b) and the spectrum of fat in panel (c). This figure is adapted from Ref. [102].

Next we extended this comparison between uniform and dual-SoS reconstruction to biological samples. Figure 5.2 compares the two reconstructions of a region of forearm in a healthy volunteer. Figure 5.2(a) reveals substantial deformation of blood vessel shape due to the assumption of uniform SoS, whereas Figure 5.2(b) shows the expected circular shape when dual-SoS model is used. In order to quantify spectral smearing just as we did for the phantom dataset, we had to modify our procedure to take into account the more heterogeneous background intensities of the tissue as well as the fact that we had no prior information about the exact distribution of chromophores within imaged tissue. As the subcutaneous fat layer is easily identifiable, we analyzed the similarity between the reconstructed optoacoustic spectra of pixels in the observed reconstruction and the reference absorption spectrum of fat in Figure 5.2(c). Figure 5.2(d) and 5.2(e) compare the reconstructed spectra in an area inside the subcutaneous fat layer (marked as P1) and in an area below the fat layer (P2). Figure 5.2(d) shows that assuming uniform SoS leads to a lipid-like spectrum in both P1 and P2, whereas Figure 5.2(e) shows that applying dual-SoS more accurately reconstructs P2.

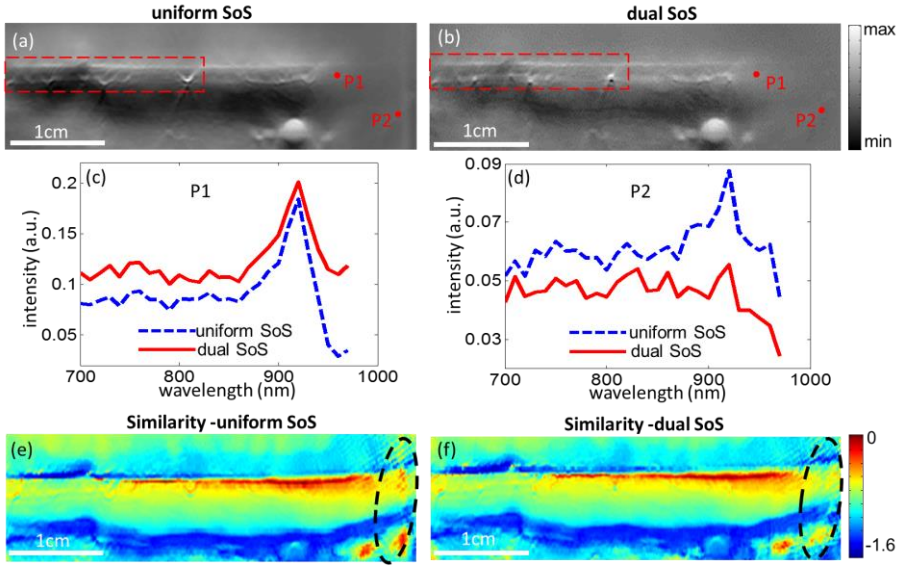

Figure 5.3. Comparison of image reconstruction of human neck region assuming uniform SoS or dual-SoS. (a) Reconstruction assuming uniform SoS at 930 nm. Red dots indicate the area (~ 15 pixels) whose spectra are shown in panels (c) and (d). (b) Reconstruction assuming dual-SoS at 930 nm. (c) Reconstructed spectra at P1 in panels (a) and (b). (d) Reconstructed spectra at P2 in panels (a) and (b). (e) Similarity between the spectrum at each pixel in panel (a) and the spectrum of fat in Figure 5.2(c). (g) Similarity between the spectrum at each pixel in panel (b) and the spectrum of fat in Figure 5.2(c).

Figure 5.2(f) and 5.2(g) show spatial analysis of the similarity of reconstructed spectra of pixels in Figure 5.2(a) and 5.2(b) with the absorption spectrum of fat in Figure 5.2(c). The red color indicates high similarity to the fat spectrum, which should be observed only in the fat layer. The region enclosed within a black dashed ellipse in Figure 5.2(f) shows that the spectrum of the blood vessel smears into the surrounding fat layer and creates a sharp gap (indicated with black arrow) in the similarity map. Meanwhile, dual-SoS reconstruction recovers a spatially continuous fat distribution in the fat layer, which is biologically more

reasonable. We obtained similar results when we compared image reconstruction of a region of human neck assuming uniform SoS or dual-SoS (Figure 5.3).

5.3 Discussion and outlook

In this chapter, we provide the spectral analysis of multispectral optoacoustic imaging artifacts induced by assuming uniform SoS in situations where the SoS changes substantially, such as when the coupling medium is heavy water. In order to improve the image quality, we developed a reconstruction algorithm that takes into account dual SoS, and this algorithm more faithfully reproduced the absorption spectra of chromophores in a phantom and tissue *in vivo*. This approach may serve as a basis for more accurate unmixing of optoacoustic signals from a range of chromophores, including oxy- and deoxy-hemoglobin, fat, and water. In this way, this approach may improve the unique ability of clinical multispectral optoacoustic imaging to simultaneously visualize numerous parameters of health and disease non-invasively in real time.

Previous studies examined artifacts induced by invariant SoS in single-wavelength optoacoustic imaging, and they demonstrated visual smearing of key features in the reconstructed image. Here we demonstrate the spectral equivalent, which we term "spectral smearing", when uniform SoS is assumed during reconstruction of multi-wavelength optoacoustic images. We show that this assumption can lead to substantial spectral distortion even when visual distortion is less obvious in reconstructed images; such spectral smearing can substantially affect the accuracy of the unmixing. This results in inaccurate quantitation of functional tissue parameters and distribution of chromophores, which is precisely where multi-spectral optoacoustic imaging can offer a high-resolution, non-invasive advantage over other imaging methods.

The dual-SoS model developed in this study can be easily adapted to other coupling media, such as water and ultrasound gel, without increasing computational cost. This model may be useful for handling SoS variation not only between sample and coupling medium, but also between different tissues inside the sample, such as fat and muscle. Application of this model should improve spectral unmixing results and subsequent quantitation of molecules in tissues. This should be tested directly in future controlled experiments.

In conclusion, we studied the influence of uniform SoS modeling on spectral accuracy and the benefits of using a dual-SoS model to account for the SoS variation between heavy water and tissue sample. The dual-SoS model was developed by employing two SoS in the imaged region specifically focused towards imaging lipids and biomolecules. The spectral smearing introduced by uniform SoS reconstruction was quantified and the dual-SoS reconstruction was demonstrated to be able to correct the spectral smearing and lead to more accurate spectral information. As spectral accuracy is the foundation of molecular optoacoutic imaging, dual-SoS reconstruction should be applied in the future to avoid spectral smearing and enable accurate unmixing of different chromophores like oxyhemoglobin, deoxyhemoglobin, and lipids.

6. Ultrasound imaging and image reconstruction in OPUS systems

As introduced in Chapter 2 and Chapter 4, hybrid OPUS systems such as Acuity256 are capable of performing ultrasound imaging and optoacoustic imaging with good co-registration in clinical applications. The customized Acuity256 includes a key innovation of a concave transducer array with cylindrical focused transducer elements for both ultrasound and optoacoustic imaging. Meanwhile, the implications of this innovation for hybrid OPUS have not been fully studied. As a result, many aspects of data collection, signal processing and reconstruction are probably far from being ideal. Therefore, in this chapter, the work which has been done to improve the ultrasound image quality ranging from imaging schemes to image reconstruction are studied.

This chapter starts from a brief introduction of the background and technical fundamentals of clinical ultrasound imaging. Then the synthetic aperture technique is described as the foundation of ultrasound image reconstruction. The pipeline of ultrasound image formation based on delay-and-sum algorithm and a dual-SoS model is introduced in the second half of this chapter. Moreover, signal preprocessing techniques used in conventional ultrasound field such envelope detection and spiking deconvolution are introduced and their effect on reconstructed ultrasound images are demonstrated with phantom and tissue datasets acquired using the customized OPUS system. Finally, two variations of the synthetic transmit aperture schemes are explored to speed up the acquisition process and improve ultrasound image quality.

6.1 Conventional ultrasound imaging in medical applications

Ultrasound has been widely used as a diagnostic imaging technique in clinics since the last century [82, 113], because of its unique advantages such as safety/no radiation, portability and real-time capability [61]. In medical applications, ultrasound waves of frequency from 1MHz to 50 MHz [61, 82] are used to perform morphological imaging of internal body structures and organs [114] and to study the dynamics of the target structures [115].

Clinical ultrasound imaging can be divided into transmission mode or reflection mode depending on the spatial relationship between the ultrasound emitter and the receiver [116, 117]. Transmission-mode ultrasound is also known as ultrasound transmission tomography (UTT) [116, 118]; in this case, the ultrasound receiver/transducer/detector is located on the opposite side of the sample from the ultrasound emitter, and the sound wave needs to propagate through the whole specimen to reach the transducer surface. This type of ultrasound is mostly used to estimate the attenuation coefficient [119, 120], refractive index [121] and SoS distribution [120] in tissue for the detection of diseases, for example breast cancer [116]. In reflection-mode ultrasound, also termed pulse-echo ultrasound [117], the ultrasound emitter and transducer are located on the same side of the specimen, and the emitted ultrasound wave is reflected or scattered by the structures in the specimen back to the transducer. This enables the design of portable probes used in most clinical ultrasound applications where the visualization of anatomical structures or their dynamics is needed

[82], such as obstetric ultrasonography [122]. Pulse-echo mode ultrasound is used in our handheld OPUS system and therefore is the focus of the following text.

The physical process of pulse-echo ultrasound imaging in medical applications can be described as follows: a pulser excites the transducer with a short pulse, often modeled as an amplitude-modulated sinusoid [82], i.e. $p(t) = a(t)e^{i2\pi f_0 t}$, where f_0 is the carrier frequency, typically 1-10 MHz. Then an ultrasound pulse is emitted from a transducer surface and propagates inside the tissue and reflected by the acoustic heterogeneities of tissue. The heterogeneities are mainly formed by the interfaces of different tissue layers or scatterers inside the tissue. Depending on the size of the heterogeneity, the ultrasound pulse is partly reflected or scattered back to the transducer and converted from pressure into electrical signals by the transducer and then digitalized and acquired by a data acquisition system at a certain sampling frequency. Our customized Acuity256 system introduced in Chapter 4 generates ultrasound pulses with a central frequency 6 MHz, and the echoes are acquired with a sampling frequency 24 MHz.

Pulse-echo mode ultrasound can be further classified into 3 categories, A-mode, B-mode and 3D ultrasound imaging, depending on the dimension(s) in which the detected electrical signals are displayed.

A-mode (amplitude-mode): In A-mode ultrasonography, a single transducer is used to scan a line through the specimen and then the reflected echoes are plotted as a time sequence that is a function of tissue depth. A-mode ultrasound can be used to estimate the depth and dimensions of organs [123, 124] or to calibrate other modalities [125]. Longitudinal continuous acquisition of A-mode signals can also be used to detect fetal heart beat in early pregnancy [126] and the asymmetry between left and right hemispheres of the brain [127].

B-mode (brightness-mode, 2D mode): B-mode ultrasound forms a 2D image to show the anatomical structures in the object instead of a time sequence in A-mode. In B-mode ultrasound imaging, a linear array comprising multiple transducer elements (normally 64, 128 or 256 elements) are used to scan a plane of the specimen. Real-time B-mode ultrasound imaging has been commonly used in clinical applications, such as image-guided injection [128], lesion identification [129], cardiac or vascular movement visualization [130] and blood flow measurement based on the Doppler effect [131]. Since the ultrasound modality in Acuity256 is B-mode ultrasound, we mainly consider this mode in this dissertation.

3D ultrasound: 3D ultrasound is an extension of B-mode ultrasound from 2D to 3D by adding another scan dimension to B-mode ultrasound. It offers a volume rendering of ultrasound data and is normally capable of displaying the volumetric rendering over time. In 3D ultrasound imaging, the third dimension of scanning is commonly achieved by tilting the probe manually, tilting the probe mechanically with a motor, using an endoprobe or using a matrix array transducer [61]. With 3D ultrasound imaging, three-dimensional structures under investigation can be visualized directly from the monitor, which means that the clinician need not mentally reconstruct the 3D geometry of a lesion from its B-mode images. Therefore, 3D imaging is widely used in cases where volumetric information is necessary, such as fetal, trans-rectal and intra-vascular applications [132].

6.2 Ultrasound imaging with the customized OPUS system

B-mode ultrasound has been widely combined with other imaging modalities to enable hybrid imaging in clinics, such as X-ray computed tomography (CT) [133], MRI) [134], positron emission tomography (PET) [135] or single-photon emission computed tomography (SPECT) [136]. Since both ultrasound and optoacoustic imaging detect ultrasound waves, it is natural to combine them into a hybrid OPUS system.

As introduced in Chapter 4, the customized OPUS system utilizes a cylindrically focused concave transducer array with transducer element size being a compromise value between that needs in optoacoustic imaging and that needs in ultrasound imaging to achieve adequate image quality for both modalities. This design optimizes optoacoustic signal detection but places challenges on ultrasound signal SNR [97]. Although the element size in the customized Acuity256 probe is smaller than that in standard optoacoustic tomography to reduce the occurrence of grating lobes happening in ultrasound imaging, the pitch size of the probe is still approximately 1.9 wavelengths, which is much larger than half a wavelength and therefore leads inevitably to grating lobes [98, 137]. Therefore, in order to reduce the artifacts introduced by grating lobes, optimized transmit-receive beamforming methods such as the synthetic aperture ultrasound technique (SAU) [61, 97, 138] need to be used during ultrasound imaging to achieve good image quality and real-time performance.

The customized OPUS uses a SAU that was firstly applied in radar systems in the 1950s [61]. Since then, the earliest simple model of a generic synthetic aperture (Figure 6.1) has been adapted for different applications, such as the synthetic receiver aperture (Figure 6.2) and synthetic transmitter aperture (Figure 6.3) [61].

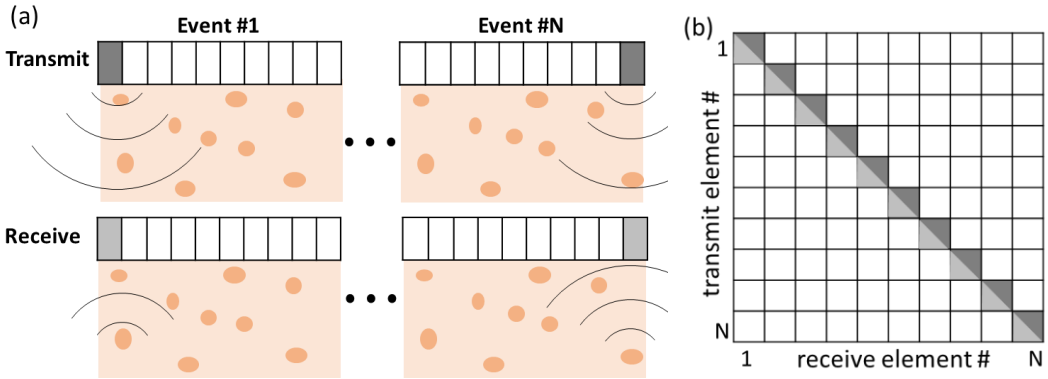

Figure 6.1. Generic synthetic aperture ultrasound imaging. (a) Diagram of the activation of transmitter and receiver elements in each event. The entire acquisition occurs as N events. (b) Active transmitter and receiver transducer element combinations in a generic synthetic aperture. The row number corresponds to the number of the transmitter element; the column number, to the number of the receiver element. Dark gray marks the active transmitter element and light gray marks the active receiver element.

Generic synthetic aperture: In generic synthetic aperture ultrasound, the same transducer element is activated firstly to emit an ultrasound pulse, then later to receive the reflected ultrasound waves after a certain delay time (Figure 6.1). During the entire acquisition process, all elements are activated one by one sequentially. The phrase "imaging event" is used in this

chapter to refer to the process that begins with the emission of an ultrasound pulse and ends with the receipt of reflected echoes.

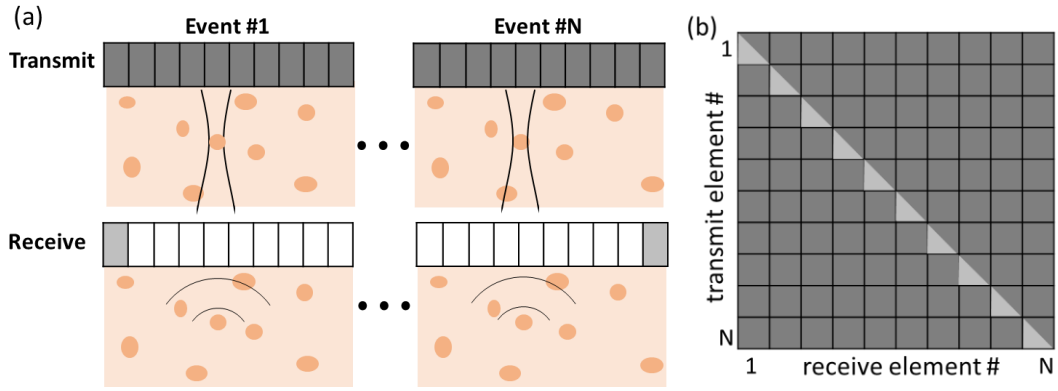

Figure 6.2. Synthetic receive aperture (SRA) ultrasound imaging. (a) Diagram of the activation of transmitter and receiver elements during each imaging event. The entire acquisition involves N imaging events. (b) The combination of active transmitter and receiver transducer elements in the SRA. The row number corresponds to the number of the transmitter element; the column number, to the number of the receiver element. Dark gray marks the active transmitter element and light gray marks the active receiver element.

Synthetic receive aperture (SRA): In one imaging event, all transducer elements are activated to emit ultrasound pulses and focus along a scan line (Figure 6.2). Then the reflectors or scatterers along this scan line reflect ultrasound waves back towards the transducers. During the receiving process, only one element is activated to receive ultrasound waves. The imaging event is repeated by going through all elements for receiving. SRA can provide higher SNR than the generic synthetic aperture, but with long acquisition time [61].

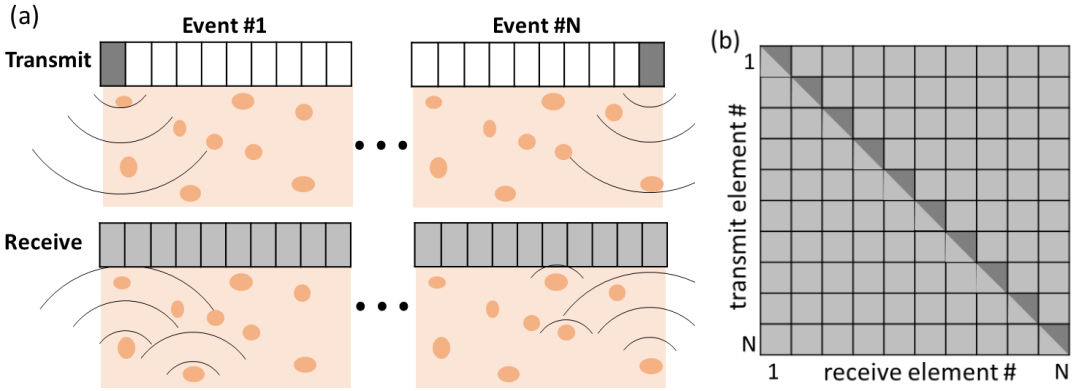

Figure 6.3. Synthetic transmit aperture (STA) ultrasound imaging. Figure 6.3. Synthetic transmit aperture (STA) ultrasound imaging. a) Diagram of the activation of transmit and receive elements in each imaging event. The entire acquisition involves N imaging events. (b) Active transmit and receive transducer element combination in synthetic transmit aperture. The row number corresponds to the number of the transmitter element; the column number, to the number of the receiver element. Dark gray marks the active transmitter element and light gray marks the active receiver element.

Synthetic transmit aperture (STA): As the converse of the situation with an SRA, an STA activates one element to emit an ultrasound pulse but all elements to receive ultrasound echoes during one imaging event (Figure 6.3). This scheme provides higher SNR than the generic synthetic aperture and faster frame rate than the SRA [61].

Given the advantages of the STA and the cylindrical focus of the Acuity256 transducer array, the studies in this dissertation were carried out using a modified STA design (Figure 6.4) if no extra ultrasound working scheme is provided. In each imaging event, one transducer element emits an ultrasound pulse towards the center of the array, then the ultrasound waves are reflected/scattered back towards the transducer from all directions. Then half of the transducer elements are used to detect echoes. In other words, in imaging event #i, element #i is activated to emit an ultrasound pulse and elements from #i to #(i+127) are activated to receive echoes [Figure 6.4(b)].

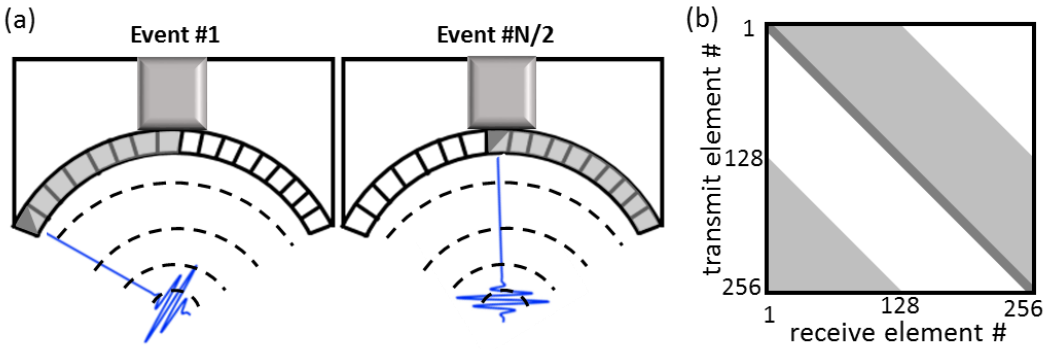

Figure 6.4. The STA in the Acuity256 system. (a) Diagram of the activation of transmit and receive elements in each imaging event. The entire acquisition involves N=256 imaging events. (b) Active transmit and receive element combination in the Acuity256. In each event, one element emits a pulse and 128 elements receive the echoes. The row number corresponds to the number of the transmitter element; the column number, to the number of the receiver element. Dark gray marks the active transmitter element and light gray marks the active receiver element.

6.3 Ultrasound image formation

The ultrasound echoes are detected and converted by the transducers from pressure waves to electrical signals, then digitalized and recorded as a data sequence $S(t)$ by the data acquisition system. The saved data are reconstructed into ultrasound images that can be interpreted by the clinician. In this dissertation, ultrasound images are formed using a delay-and-sum method that takes into account the STA imaging scheme, concave geometry of the transducer array and the use of heavy water as coupling medium. In contrast to conventional delay-and-sum methods, the one used here takes into account the SoS difference between coupling medium and specimen, and it uses a customized stack projection procedure to optimize ultrasound image quality.

6.3.1 Delay-and-sum reconstruction

Delay-and-sum reconstruction in ultrasound imaging is based on the time of flight (ToF) of the ultrasound pulse between emission and receipt. In pulse-echo ultrasound mode, the ToF of a pulse is decided by its traveling distance from the emitter to the reflectors/scatterers and

back to the receiver. Based on the relationship between time and space, the acquired data can be back-projected onto the grids in the imaged region.

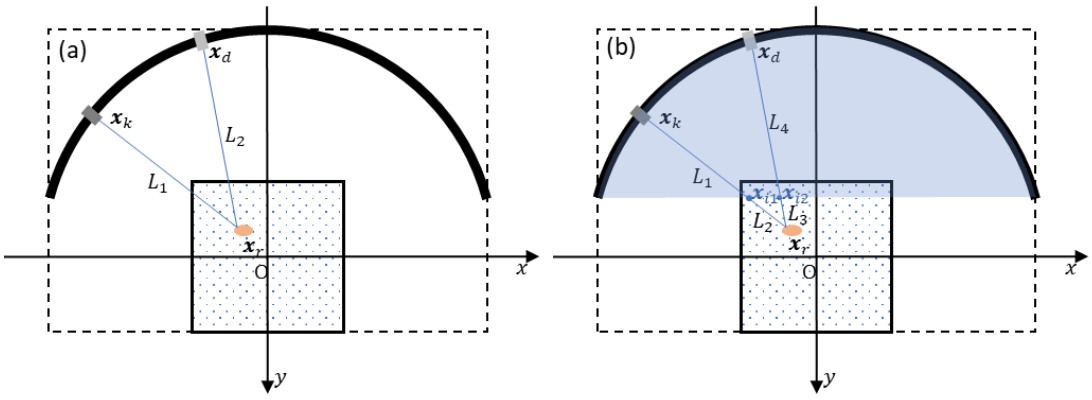

Figure 6.5. Schematic of the spatial relationship among all variables in in the image reconstruction described in this chapter. $\boldsymbol{x}_k$, $\boldsymbol{x}_d$ and $\boldsymbol{x}_r$ are the respective locations of the transmitting/emitting element, receiving element and acoustic reflector/scatter. The black arc represents the entire transducer array, and the black solid square is the image region/ROI. (a) The travel distance in homogeneous medium equals the propagating forward distance plus the backward distance, i.e. $L = L_1 + L_2$. (b) In the Acuity256, which uses coupling medium showing strong mismatch of SoS with the sample, travel distance $L = L_1 + L_2 + L_3 + L_4$, with $\boldsymbol{x}_{i1}$ and $\boldsymbol{x}_{i2}$ being the two intersection points of the acoustic paths with the coupling medium interface.

As Figure 6.5(a) shows, in an acoustically homogeneous medium, the traveling distance L from an emitter with coordinates $\boldsymbol{x}_k$ to a reflector/ scatter $\boldsymbol{x}_r$ and then back to the receptor $\boldsymbol{x}_d$ is described by $L = L_1 + L_2$ which corresponds to a ToF described by

$$t(\boldsymbol{x}_k, \boldsymbol{x}_d, \boldsymbol{x}_r) = \frac{\sqrt{(\boldsymbol{x}_k - \boldsymbol{x}_r)^2}}{c} + \frac{\sqrt{(\boldsymbol{x}_r - \boldsymbol{x}_d)^2}}{c}, \qquad (6.1)$$

where c is the SoS in the medium. The customized Acuity256 system introduced in Chapter 4 uses heavy water as coupling medium, and the SoS difference between this medium and tissue is not negligible since it can introduce deformation to the structures which is demonstrated in Chapter 5. Therefore, a dual-SoS model was applied to ultrasound image reconstruction. In this case, the calculation of ToF needs to be adjusted to

$$t(\boldsymbol{x}_k, \boldsymbol{x}_d, \boldsymbol{x}_r) = \frac{\sqrt{(\boldsymbol{x}_k - \boldsymbol{x}_{i1})^2}}{c1} + \frac{\sqrt{(\boldsymbol{x}_{i1} - \boldsymbol{x}_r)^2}}{c2} + \frac{\sqrt{(\boldsymbol{x}_r - \boldsymbol{x}_{i2})^2}}{c2} + \frac{\sqrt{(\boldsymbol{x}_{i2} - \boldsymbol{x}_d)^2}}{c1}, \qquad (6.2)$$

where $\boldsymbol{x}_{i1}$ and $\boldsymbol{x}_{i2}$ are the respective intersection points of the forward- and backward-propagation paths of an ultrasound wave from $\boldsymbol{x}_k$ to $\boldsymbol{x}_d$ with the interface of coupling medium and sample under the straight ray propagation assumption [Figure 6.5(b)], $c1$ is the SoS in couplant, and $c2$ is the SoS in the sample.

During signal acquisition in one imaging event, the amplitude of acquired signal $S_{k,d}(t)$, in which element k transmits the pulse and element d receives the echoes, reflects the contributions of all reflected echoes arriving at the same time from all reflectors/scatters in the imaged region. This can be expressed as:

$$S_{k,d}(t) = \sum_{i=1}^{M} s_i(t), \qquad (6.3)$$

where $s_i(t)$ is the echo from ith reflector and M is the number of the reflectors in the imaged region that satisfy the condition $c \cdot t = \sqrt{(\boldsymbol{x}_k - \boldsymbol{x}_r)^2} + \sqrt{(\boldsymbol{x}_r - \boldsymbol{x}_d)^2}$. In the inverse computation for an imaging event e in the Acuity256 system, the intensity (reflectivity) of a spatial point I_k is calculated by summing the amplitudes of all reflected signals from that point in the same event:

$$I_k = \sum_{d=k}^{k+\frac{N}{2}-1} S_{e,d}(\mathrm{t}). \quad (6.4)$$

Based on Equation 6.4, an ultrasound image can be formed for each imaging event and N images are formed for all imaging events.

Since each imaging event covers only a limited area of the specimen, therefore captures only part of the information from the sample, each of the N images contains only a few structures in the sample, making each image on its own insufficient for clinical interpretation. To summarize the information contained across all imaging events, the N images need to be merged into one image with a stack projection or Z-projection. The appropriate projection type depends on the type of data being represented and the structures need to be highlighted for a specific application. In the work described in this chapter, our goal was to optimize image contrast and resolution, so we focused on three types of projection: average intensity projection (AIP), maximum intensity projection (MIP) of the N images and the combination of the two projection types (AIP + MIP).

AIP, which is equivalent to summation projection and is widely used in X-ray CT [139] and optoacoustic tomographic image reconstruction [140], can efficiently reduce noise and thereby improve image contrast. The procedure can be expressed as

$$I = \sum_{k=1}^{N} I_k / N. \quad (6.5)$$

MIP is widely used in X-ray CT [141] and magnetic resonance angiography (MRA) [142] for 3D data visualization and has been demonstrated to connect the high intensity dots of the blood vessels in three dimensions, providing an angiogram that can be viewed from any projection. Each point in the MIP represents the highest intensity experienced in that location on any partition within the imaging volume., i.e.

$$I = \max_{k=1,2\ldots N} I_k. \quad (6.6)$$

AIP + MIP: The third projection type is to combine AIP and MIP to enjoy the advantages of both methods. Unlike the standard AIP or MIP, this method prompts for a group size n_{sec} that must be a factor of the total number of slices in the stack, and then the method groups the stack into $(N - n\_sec + 1)$ subsets. Within each subset, AIP is applied, which results in a new stack of N/n_sec slices, with each slice being an averaged image of a subset of the original stack. Then MIP is applied to the resulting $(N - n\_sec + 1)$ images to generate the final ultrasound image. In other words,

$$I = \max_{i=1,2\ldots(N-n\_sec+1)} I_i\,,\ I_i = \left(\sum_{k=i}^{i+n_{sec}-1} I_k\right)/n\_sec. \quad (6.7)$$

In Equation 6.7, if group size n_sec equals the number of slices in the stack, the method will evaluate the stack in the same manner as AIP. If group size n_sec equals 1, the method will

evaluate the stack in the same manner as MIP. In the work described in this chapter, n_sec was set to 16, which in pilot studies with phantom and tissue datasets efficiently reduced noise and kept speckle low in the background. To generate the figures in this chapter, the raw ultrasound image I was compressed logarithmically to enhance contrast, and 2D order-statistic filtering was applied as post-processing when no envelope detection was used during signal pre-processing.

Figure 6.6 shows the reconstruction results of an acoustic phantom and the arm region of a volunteer using the above three types of projection. Procedures on human subjects were performed after obtaining their written informed consent. For the phantom datasets showed in this chapter, they were acquired using a standard Acuity256 whose probe is of 4cm radius, 3 MHz central frequency and 124-degree coverage angle.

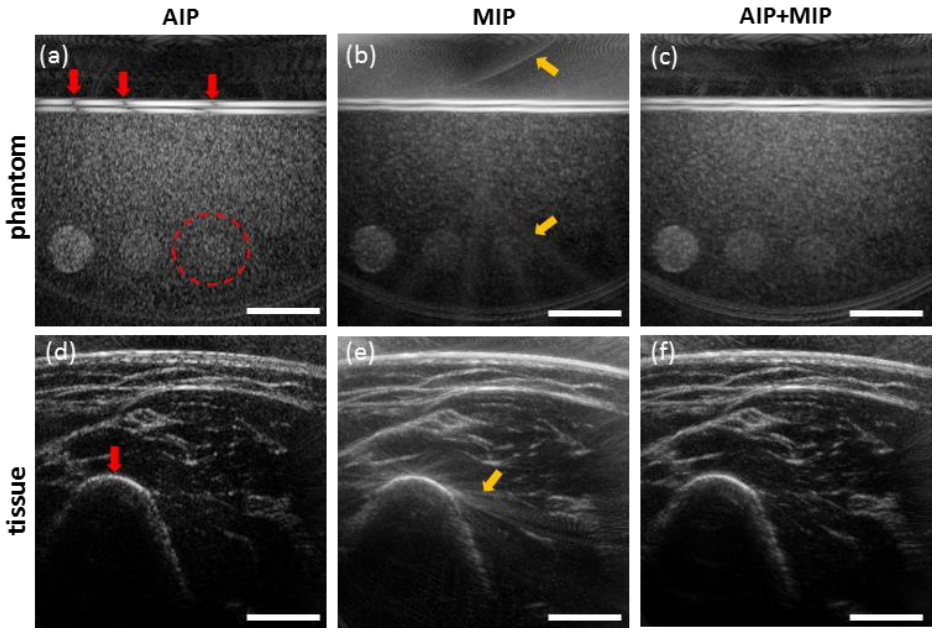

Figure 6.6. Reconstructed ultrasound images with three different Z-projection methods. (a-c) Reconstructed images of the acoustic phantom and (d-f) Reconstructed images of the arm region of a volunteer. Red arrows indicate the discontinuity introduced by AIP; the red dashed circle, the third target region; and yellow arrows, the noise highlighted by MIP. Scale bars are 1 cm.

The first row of Figure 6.6 is the reconstruction result of an acoustic phantom that includes three acoustic regions with different reflectivity. Figure 6.6(a) shows the reconstruction result of AIP, in which discontinuity exists at the interface of coupling medium and sample (marked with red arrows). In addition, strong speckles are visible on the background of the phantom and reduce the contrast of the third target region (red dashed circle). Figure 6.6(b) presents the reconstructed image with MIP, in which the discontinuity issue at the interface is absent, and much less speckling is observed in the background. However, some artifacts not observed in the AIP projection are visible (yellow arrows). Figure 6.6(c) shows the results of combining AIP and MIP. All 3 contrast regions and the interface are successfully reconstructed, and the strong artifacts seen with the MIP projection are eliminated.

Figure 6.6(d) - 6.6(e) are the reconstruction images of the arm region of a volunteer after projection using, respectively, AIP, MIP or AIP+MIP. In Figure 6.6(d), the strong speckle effect of AIP damages the continuity of all structures in the tissue. For example, several gaps are observed along with the surface of the bone (red arrow), which is a strong acoustic reflector and should therefore appear as a continuous arc in ultrasound images [143]. In Figure 6.6(e), the structures inside tissue are successfully reconstructed, but the reflection from bone causes smearing artifacts that contaminates the background. With AIP+MIP in panel 6.6(f), the reflection artifacts are reduced, and the continuity of the structures is maintained.

Comparing the images in the first and second column of Figure 6.6, it can be seen that AIP can contribute to high contrast noise ratio (CNR) because the averaging procedure can reduce noise and enhance the signals from the target, but that the projection approach generates strong speckles that generate gaps in continuous structures. MIP, for its part, can generate smooth and continuous structures, but it suffers from artifacts introduced by random noise or stable reflections in some imaging events. The third column shows that the combination of AIP and MIP combines the advantages of AIP and MIP. The average procedure in the first phase of this method can reduce the noise and the reflection artifacts from strong reflectors. The MIP in the second phase can maintain the continuity of structures and minimize the speckles introduced by coherence of different events.

6.3.2 Advanced signal preprocessing

The images showed in Figure 6.6 were reconstructed after the ultrasound signals had been band-pass filtered according to the central frequency of the excitation pulse and central frequency of transducer elements. However, more advanced signal preprocessing is normally used in conventional ultrasound imaging. For example, envelope detection based on I/Q demodulation [144] or Hilbert transformation [145] is commonly used in signal preprocessing to prevent ripple artifacts in clinical ultrasound imaging. In addition, spiking deconvolution has been developed and demonstrated to give image resolution higher than conventional envelope detection [146].These methods are implemented into the ultrasound image reconstruction of the Acuity256. In this section, we introduce briefly the concept of each method and show the reconstruction results using each method. In addition, the effect of preprocessing methods on the final reconstructed images is discussed.

1) I/Q demodulation

I/Q demodulation, also termed as quadrature detection, is commonly used for envelope detection in ultrasound imaging. This method consists of 3 main steps [144]. In the first step, the method down-mixes a signal $S(t)$ with two sinusoidal signals with a 90-degree phase difference as $\mathrm{I}(t) = S(t)\cos(2\pi f_0 t)$; $\mathrm{Q}(t) = S(t)\sin(2\pi f_0 t)$, i.e. $S_{IQ}(t) = S(t)\mathrm{e}^{-\mathrm{i}2\pi f_0 t}$, where f_0 stands for the central frequency of the excitation ultrasound pulse. In the second step, the method uses a low-pass filter (e.g. finite impulse response filter) to remove the negative frequency spectrum and the noise outside the desired bandwidth. In the third step, the envelope is detected using $\sqrt{I^2 + Q^2}$. The advantage of I/Q demodulation is its straightforward implementation in both hardware and software. On the other hand, it requires low-pass filtering that can result in blurring.

2) Hilbert transform-based envelope detection

Another method to detect the envelope of a signal is based on Hilbert transformation, which is used for creating a so-called analytic signal [145]. For an ultrasound signal $S(t)$, its Hilbert transform is $\hat{S}(\mathrm{t})$ and its analytic signal is $S_a(t) = S(t) + i\hat{S}(\mathrm{t}) = \mathrm{A(t)e}^{-\mathrm{i}\varphi(\mathrm{t})}$, where A(t) is the instantaneous amplitude and can be used to find the envelope of the signal. This method gives good results and is increasingly used as sample rates and digital processing capabilities increase. This method is efficient in reducing ripple artifacts, while maximizing image details. A downside of this method is that it takes more time than I/Q demodulation, which might be problematic in real-time or high-frame-rate imaging.

Although the idea of I/Q demodulation and Hilbert transformation are different, the envelope detection results using these two methods are the same. Therefore, in the following text, we show only the envelope detection results using Hilbert transformation.

3) Spiking deconvolution

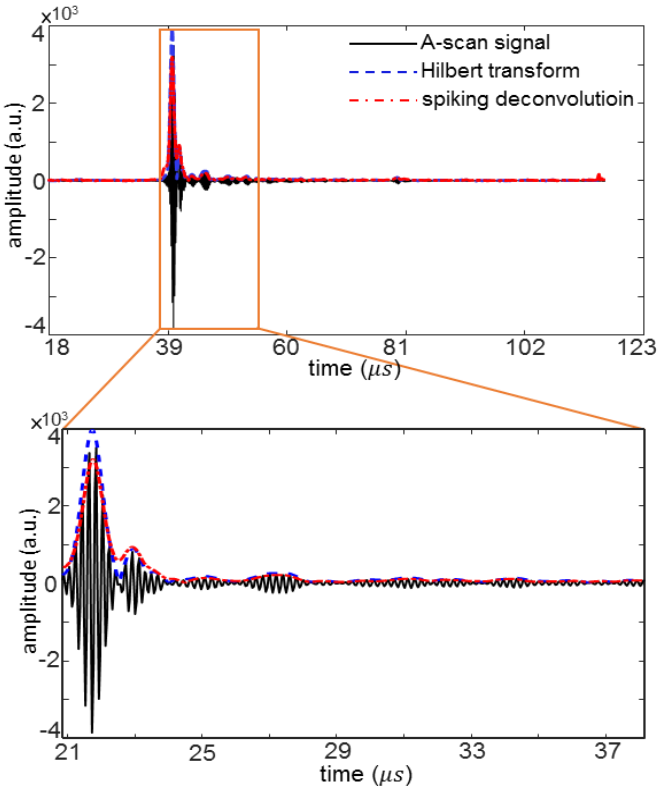

Figure 6.7. Signal preprocessing results with Hilbert transform-based envelope detection method and spiking deconvolution. The A-scan ultrasound signal is a solid black line; envelope detection using Hilbert transformation, a dashed blue line; and spiking deconvolution, a dash-dot red line.

Spiking deconvolution is a relatively new preprocessing method in ultrasound, whose goal is totally different from that of envelope detection. Instead of trying to remove the carrier signal in the pulse and recover the signal envelope, spiking deconvolution tries to identify the reflectors' location in the signal and its reflectivity. The core of this method is the assumption

that an ultrasound echo signal $S(t)$ can be modelled as the convolution of the tissue response $x(t)$ with the emitted ultrasound excitation pulse $w(t)$, which can be expressed as [146]

$$S(t) = w * x\,(t). \qquad (6.8)$$

The emitted excitation pulse is dependent on the pulse $p(t)$ generated by the pulser and the transfer function of transducer elements, while $x(t)$ is the tissue response, which is a spatial reflectivity distribution. Therefore, with the echo signal $S(t)$ and emitted pulse $w(t)$ known, the tissue response $x(t)$ can be deconvolved with the inverse filter of $w(t)$. In the ideal case of homogeneous medium and no acoustic attenuation, sharp peaks appear at the location of reflectors in the deconvolved signals as shown in Ref. [146].

However, this method cannot generate ideal peaks in lossy media, such as tissue, because it is sensitive to noise and the match of acquired signal to the shape of the emitted pulse. As a result, spiking deconvolution of clinical data cannot generate ideal clean peaks, but instead a peak is accompanied by multiple sidelobes and noise. In order to adapt this method for tissue imaging for clinical OPUS systems and avoid ripple artifacts introduced by the sidelobes, envelope detection is applied to the signals after deconvolution. For simplicity, this method including standard spiking deconvolution and envelope detection is hereafter referred as spiking deconvolution.

Figure 6.7 shows an A-scan ultrasound signal from the Acuity256 system in a solid black line, the envelope detection result using Hilbert transformation in a dashed blue line, and the spiking deconvolution result in a dash-dot red line. From the first burst of the A-scan signal in the zoomed-in window, spiking deconvolution gives different results than envelope detection and leads to sharper peaks. The effect of the signal preprocessing on the final reconstructed ultrasound images are demonstrated with Figure 6.8, in which the reconstruction result without advanced signal preprocessing is marked as ‘standard’; the one with envelope detection, as ‘Hilbert transform’; and the one with spiking deconvolution, as ‘spiking deconvolution’.

Figure 6.8 shows the effect of different signal preprocessing methods on the reconstructed ultrasound images. Figure 6.8(a) is the schematic of the acoustic phantom (Model 551, ATS Laboratories-Phantoms, USA), with imaged region demarcated with a red square. Figure 6.8(b) shows the zoomed-in view of the imaged region of the phantom, which includes multiples line targets on vertical and horizontal direction. The reconstructed ultrasound image of this region with no advanced signal preprocessing, with envelope detection or with spiking deconvolution are shown in panels 6.8(c), 6.8(d) and 6.8(e), respectively. Comparing panel 6.8(c) and 6.8(d), it can be seen that envelope detection gives similar image quality as the standard reconstruction for the targets (dots), but with weaker background noise. Comparing the image in panel 6.8(e) with the other two images, we can see that spiking deconvolution recovers a thinner line of interface (marked with yellow arrow), sharper dots and weakest background noise. Due to the intrinsic ability of deconvolution methods to increase SNR, reduction in the random noise on the background using spiking deconvolution translates to stronger fixed-pattern noise, which the algorithm treats as signal from the target (marked with white arrow). Figure 6.8(f) and 6.8(g) show the line profile of the dots along lines 1 and 2 on panel 6.8(b), respectively. The results show that spiking deconvolution achieves the best resolution and SNR among the three methods. In cases where two dots

locate close enough that they are barely differentiated with the standard or Hilbert transformation-based methods, spiking deconvolution clearly separates them [red arrow in panel 6.8(f)].

Although spiking deconvolution outperforms the other two methods, it may amplify some pattern noise. In order to avoid strong artifacts from such noise on reconstructed images, the noise should be removed using a proper filter. Since such noise is normally frequency-dependent, a bandpass, low-pass, or high-pass filter can be used.

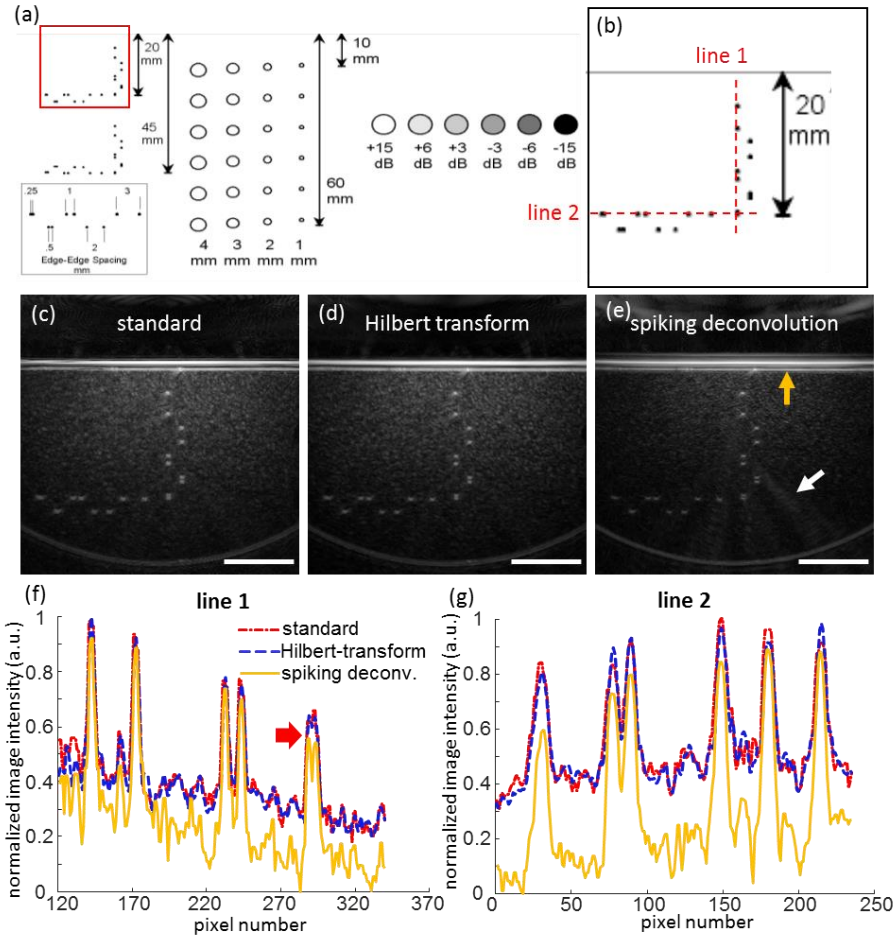

Figure 6.8. Reconstruction of a commercially available acoustic phantom using three signal preprocessing strategies. (a) Schematic of the acoustic phantom with the imaged region highlighted using a red square. (b) Imaged region and the lines (red dashed) used to generate line profiles in panels (f) and (g). Reconstruction of ultrasound signals was performed (c) without advanced signal preprocessing, (d) with envelope detection using the Hilbert transform, or (e) with spiking deconvolution. Image quality was quantitatively analyzed along line profiles (f) along line 1 in panel (b) and (g) along line 2 in panel (b). Scale bars are 1 cm.

6.4 Variation of default STA

In the default STA of the customized Acuity256, data acquisition requires 256 imaging events and 1 emitting element and 128 receiving elements for each imaging event (see Section 6.2). The 128 receiving elements are continuous and shift one by one from event to event. This

acquisition scheme might not be optimal for three reasons. Firstly, when the transmitting element #i is larger than #128, some receiving elements are located on the opposite side of the probe [Figure 6.9(a)], and this lies outside the reflection angle according to Snell's reflection law. Secondly, the default STA takes a long time and generates huge amounts of data, requiring more computational time and power. Moreover, motion is inevitable during clinical scanning, so when acquisition takes too long, motion is inevitable in clinical scan which might introduce artifacts that damage image quality. Therefore, we propose two transmitting-receiving schemes that use the same number of acquisition channels as the default setting, i.e. 128 receiving channels for each event. We then compared these two schemes, named Scheme 2 and Scheme 3, with the default settings, named Scheme 1. In Scheme 2, in order to collect the echoes within the reflection angle, when the emitting element #i is larger than #128, the acquisition elements are from #i to #(i-127) [Figure 6.9(b)]. In Scheme 3, we propose to use only the central 128 elements for transmitting in order to shorten acquisition time and reduce the acquired data amount [Figure 6.9(c)].

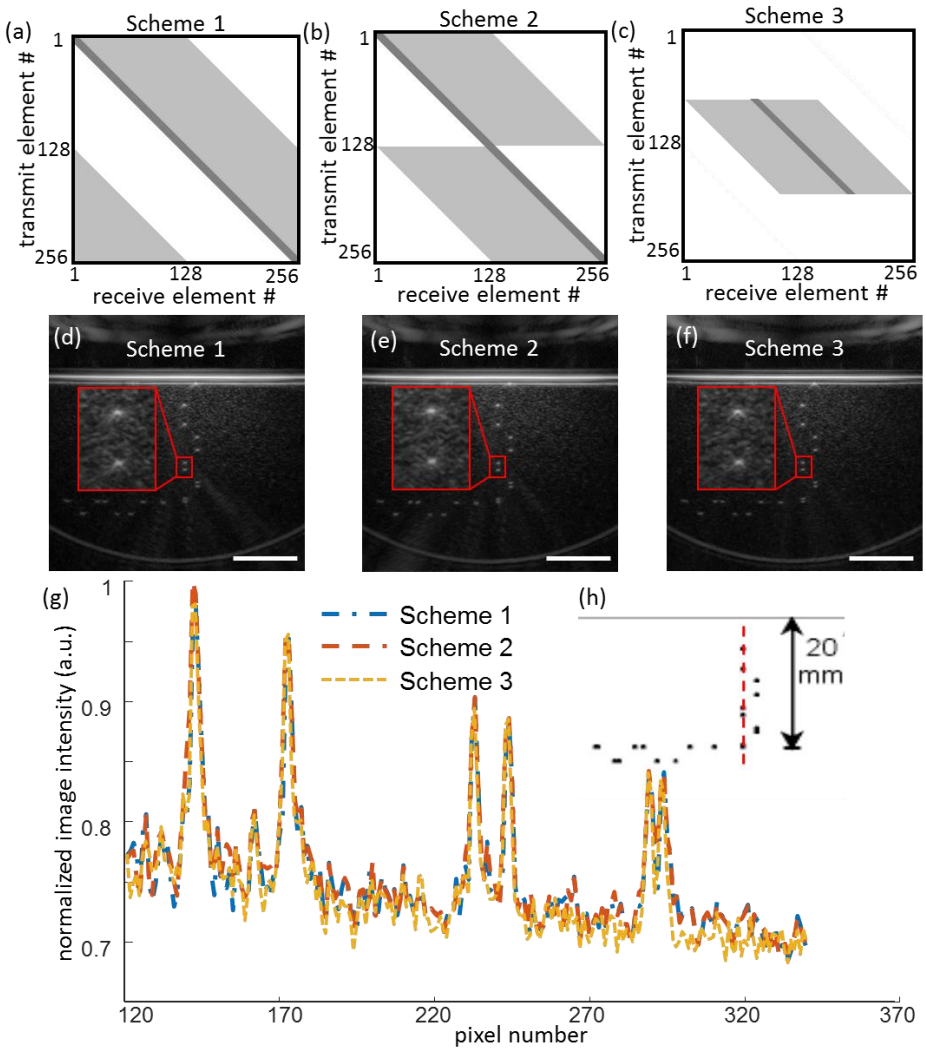

Figure 6.9. Three different transmitting and receiving schemes and their ability to reconstruct the phantom described in Figure 6.8. (a-c) Three emitting and receiving schemes for the Actuity256.

(d-f) Phantom reconstruction using each acquisition scheme. (g) Line profile of the dots along the red vertical line. Scale bars are 1 cm.

Figure 6.9 shows reconstruction with the three transmitting-receiving schemes. The three different acquisition schemes are shown schematically in Figures 6.9(a) – 6.9(c). Each scheme was used to image the same acoustic phantom showed in Figure 6.8(b), and the results are shown in Figure 6.9(d) – 6.9(f). It can be seen that Scheme 2 generates a similar image as Scheme 1 but with better recovery of dot shape (see zoomed-in regions). Scheme 3 generates the best image quality without any information loss, as seen in the line profiles in Figure 6.9(g), even though Scheme 3 handles only half as much data as the other two schemes. From the comparison, we can see that it is redundant to use all elements for transmitting. In other words, proper selection of receiving elements can substantially reduce the number of imaging events without losing any information. The reduction in imaging event number leads in turn to shorter imaging time for each frame and lower computational cost for reconstruction, all of which facilitates real-time imaging.

6.5 Discussion and outlook

In this chapter, clinical ultrasound imaging, the synthetic aperture technique used in conventional ultrasound, and the ultrasound imaging in the customized OPUS system were introduced. In contrast to commercial ultrasound systems, the customized OPUS system optimizes the detection of optoacoustic signals by using a concave transducer array comprised of cylindrical focused transducer elements. To optimize the ultrasound image quality with this geometry, the ultrasound modality in Acuity256 uses an STA technique for sample excitation and echo detection. An adapted delay-and-sum algorithm with different Z-projection types is then used for ultrasound image formation. The best results are obtained by combining the AIP and MIP projection, because their combination avoids the disadvantages of each projection type on its own and maintains the advantages of both types. Besides, envelope detection and spiking deconvolution are applied as advanced signal preprocessing techniques to correct for the blurring introduced by 2D order-statistic filtering used in standard reconstruction. It has been demonstrated that the spiking deconvolution contributes to the best SNR and resolution than that without advanced signal processing and that with envelope detection. Moreover, two new imaging schemes other than the default scheme in customized Acuity256 have been proposed to improve ultrasound image quality and reduce time and computational cost. The Scheme 3 which uses only 128 imaging events shows the potential to reduce the cost of time and computation without scarifying image quality.

For advanced signal preprocessing, it has been demonstrated that spiking deconvolution outperforms the other two methods with better resolution and higher SNR. Since this method is based on the assumption that the A–scan signals can be modelled as the tissue response of the imaged object convolved with the shape of the ultrasound pulse, signal shape strongly influences how well spiking deconvolution performs. It would work perfectly if there is no noise in the signal and no deformation of the pulse shape in the reflected echoes. Spiking deconvolution cannot work ideally with tissue imaging, since it is a lossy medium that causes acoustic attenuation and dispersion during wave propagation, thereby deforming the pulse shape. Applying envelope detection after spiking deconvolution is one way to bypass the sidelobes and noise introduced by the deformation of pulse shape as being demonstrated in

this chapter, but for future studies, a more accurate way is to applying attenuation and dispersion compensation at the signal level before applying spiking deconvolution. Then the direct results of spiking deconvolution can be used directly for reconstruction, which can further improve the image resolution.

A matched filter as another potential advanced signal preprocessing method is worth to explore in the future, which shares the same goal and assumption as spiking deconvolution and will also contribute to higher SNR and better resolution. The assumption that A-scan signals are the convolution of excitation pulse with the tissue response implies that the tissue response can be reconstructed if the location of reflectors is known in the signal. A matched filter can be an alternative to spiking deconvolution for recovering the location of reflectors in the signals, since the A-scan signal can be treated as the summation of multiple reflected excitation pulses with some noise. If the excitation pulse is known, applying the matched filter to the denoised A-scan signals should identify the peaks of the reflectors. This method is likely to require denoising and attenuation compensation, because, like spiking deconvolution, it will be sensitive to noise and pulse shape.

The new imaging schemes for the STA shown in Figure 6.9 show the potential to reduce the number of imaging events, since Scheme 3 uses only half the time and data as the other two schemes, yet it recovers the best image quality. In future, a sparse design for both transmitting and receiving procedures is necessary for real-time imaging, which falls into the field of sparse arrays [147]. Sparse arrays are a popular technique to arrange large radio frequency telescopes in astronomy [61], and they have recently been adapted to ultrasound imaging. For the designers of sparse arrays in ultrasound imaging, how to position the elements of the array to minimize the grating lobes is the most important question. It has been demonstrated that breaking the periodicity in the positions of the elements can reduce the grating lobes, which is achievable by randomly picking the active elements in ultrasound imaging. About the rules to guide the randomly selecting the active elements, Lockwood and Foster [148, 149] have used the idea ‘effective aperture’, which is defined as the spatial convolution between the transmitting aperture function and receiving aperture function to create the Vernier Arrays. Their studies indicate that the optimal design creates an effective aperture with transmitter and receiver elements spaced $\lambda/2$ away in space, which is equivalent to space the transmit aperture (p) $\lambda/2$ and receive aperture (p+1) $\lambda/2$ and smooth the appearance with apodization [61, 148, 149]. This might be the way to optimize the transmitting-receiving schemes for ultrasound imaging using clinical OPUS in the future.

In this chapter, various improvements have been carried out by drawing on imaging schemes and image reconstruction techniques from conventional ultrasound and optoacoustic imaging. In the future, simulations are needed to compare the concave transducer array with conventional linear or convex arrays to fully understand the main difference introduced in wave propagation. Based on the understanding, further optimization studies of the acquisition schemes, signal preprocessing methods and image reconstruction may help ensure that the full potential of the concave design is exploited.

Section III: Studies of integrating hybrid information from handheld OPUS

7. US structural prior integrated model-based optoacoustic reconstruction

This chapter contains adapted text passages and figures from the publication by Hong Yang et al. [150] © 2020 Elsevier. More information is shown in appendix B.

7.1 Motivation

Although the probe design of OPUS systems in analogy to ultrasonography clinical systems allow the portability, this implementation leads to limited-view acoustic detection geometries and the collection of incomplete optoacoustic projection data from the imaged specimen. As a consequence, the corresponding reconstruction problem is ill-posed, possibly deteriorating imaging performance [151]. Limited-view detection results in streak artifacts [152] and in a low CNR in reconstructed optoacoustic images. Combined with a SNR that decreases with increasing imaging depth [67, 153-155] due to light fluence attenuation, limited-view projection optoacoustic tomography may suffer from lowered image quality as a function of depth. Therefore, there is strong motivation to develop methodologies to improve the optoacoustic image quality and facilitate accurate interpretation of physiological and functional information at increased depths, as required in many clinical studies.

Different methodologies have been suggested to account for the effects of limited-projection optoacoustics. Regularization is a suitable tool to condition ill-posed problems and achieve stable approximate solutions, and various regularization methods have been considered in limited-view optoacoustics, including total variation regularization [156] or wavelet sparsity regularization [157, 158]. Hard thresholding, truncated generalized singular value decomposition or preconditioning methods [67] have also been proposed for limited-view optoacoustic tomography. Also, a prefiltering technique has been developed for reducing streak artifacts, based on a full characterization of the artifacts in the framework of microlocal analysis [152]. However, while regularization and filtering address limited-view acquisition problems in a generic way, it does not use information specific to the sample under investigation and is not sufficient to restore the information that is lost due to incomplete data acquisition.

As introduced in Chapter 4, the relatively straightforward availability of hybrid OPUS imaging systems allows for a different approach in improving limited-view optoacoustic imaging. Ultrasound images generally provide anatomical images of tissues and can further resolve blood flow using Doppler techniques. In this role they can be employed post-hoc to aid the interpretation of optoacoustic images [46, 56-58, 159-163]. Special implementations of ultrasound imaging can also be considered for providing information about acoustic reflections in the sample imaged and subsequent correction of reflections from the optoacoustic images [164]. Nevertheless, reduction of acoustic reflections does not address the problem of limited-view projections common in clinical OPUS imaging. It has been also demonstrated in simulations, phantoms, and *ex vivo* experiments that full-view ultrasound transmission data can be used to estimate the SoS distribution in the sample, which in turn

can be used to improve the optoacoustic image quality [109, 165]. However, due to the requirements of full-view data acquisition, this approach is not applicable to handheld optoacoustic imaging.

In this chapter, we propose a novel approach for utilizing ultrasonography data co-registered with optoacoustic data, i.e. as typically collected from clinical OPUS systems, to improve the limited-view tomographic optoacoustic problem. We hypothesized that the ultrasound information could substantially improve the image quality of reconstructed images and improve medical diagnostics in an adaptive, tissue-specific manner. In particular, we considered a regional Laplacian regularization functional for optoacoustic tomography that incorporates structural information obtained from co-registered ultrasound images. Using simulations and *in vivo* measurements, we examine whether the proposed use of priors reduces limited-view artifacts and increases the contrast of structures deep in tissue. Then, we apply the method in clinical OPUS carotid imaging data and show the merits of the proposed method compared to stand-alone optoacoustic imaging. We further demonstrate for the first time that clinically important functional features of atherosclerotic plaques in the carotid can be observed with a clinical handheld OPUS system.

Despite the complementary contrast advantages of the two modalities, efficient integration of the information in co-registered optoacoustic and ultrasound data from OPUS system has not been straightforward. Because in conventional hybrid imaging such as PET-computed tomography [135], PET- MRI [136], fluorescence molecular tomography-x-ray computed tomography [137, 138], or diffuse optical tomography (DOT)-MRI [139], the typical way to integrate information is that priors are taken from a higher resolution modality and integrated into a lower resolution modality. However, in OPUS, two modalities are of similar resolution and different contrast mechanism. Therefore, how to maximize the value of clinical handheld OPUS is the focus of the works presented in this dissertation.

7.2 Methods to integrate structural ultrasound prior

OPUS systems provide complementary information in co-registered ultrasound and optoacoustic images: ultrasound images provide acoustic contrast to identify regions with different acoustic properties, while optoacoustic images provide optical contrast to identify regions with different optical properties. Since tissues with different acoustic properties usually also differ in optical properties, we designed a regularizer based on ultrasound images that promotes smoothness within regions of constant acoustic properties. To take into account the possibility that tissue features or types may have optical contrast, but no acoustic contrast, the prior needs to be 'soft', in the sense, that it does not sacrifice this pure optical contrast.

In the framework of L^2 regularization introduced in Chapter 2, prior spatial knowledge about the reconstructed object can be integrated into the reconstruction by designing a suitable regularization matrix $\boldsymbol{L}$. Previous studies have shown that using the spatial priors in this fashion – as a so-called 'soft prior' [166] – does not bias the image formation when the prior information is imperfect [167]. For example, knowing that the reconstructed object is a smooth function, the matrix $\boldsymbol{L}$ can be chosen to be a spatial high-pass filter, e.g., a discrete Laplacian operator. If, instead, it is known that the reconstructed object is smooth in certain regions and varies strongly in other regions, a regional smoothness prior based on Laplacian

method can be incorporated into $\boldsymbol{L}$. Both of these cases will be introduced in the following sections for the special case of OPUS imaging, and their performance will be compared using simulations and clinical datasets.

7.2.1 Spatial high-pass filter regularization (standard reconstruction)

The matrix $\boldsymbol{L}$ in Equation 2.15 can be defined as a spatial derivative operator [63, 67, 168]. In this case, the regularization term discriminates the high-frequency content of the image [169]. Including such a term into the regularization selects an image that is consistent with the data, while having a minimal amount of high-frequency components. The regularization parameter needs to be chosen such that high-frequency noise is suppressed, while edges are preserved. In the present study, $\boldsymbol{L}$ was defined to be a 2D discrete Laplacian operator given as:

$$L_{ij} = \begin{cases} 1, & if\ i = j \\ -\frac{1}{8}, & if\ j \in 8\ neighbours\ of\ i. \\ 0, & otherwise \end{cases} \qquad (7.1)$$

Throughout this chapter, least-squares reconstruction with this regularization operator is termed 'standard reconstruction'.

7.2.2 Regional Laplacian regularization (prior-integrated reconstruction)

Regional Laplacian regularization can be used to integrate prior information obtained by segmenting an ultrasound image of the sample into different tissue types. Similar to previous methods [167, 170], we construct an anisotropic non-homogeneous smoothness prior:

$$L_{ij} = \begin{cases} 1, & if\ i = j \\ -\frac{1}{N_k - 1}, & if\ i \neq j\ and\ i, j\ \in\ ROI_k, \\ 0, & otherwise \end{cases} \qquad (7.2)$$

where k is the index of the ROI and N_k is the number of pixels in ROI_k. The ROIs are obtained by segmenting an ultrasound image into n ROIs labelled by the index $k \in \{1,2,3, \dots, n\}$. With this design of the L matrix, each ROI is weighted equally, regardless of its area. It is the analogue of the random walk normalized graph Laplacian. Throughout this chapter, least-squares reconstruction with this regularization operator is termed 'prior-integrated reconstruction'.

This design of $\boldsymbol{L}$ promotes a reconstructed image that is smooth inside each ROI and highlights the difference between different ROIs, while remaining consistent with the data. This approach is based on the idea that dominant photon-absorbers vary between different tissue types, but are similar within one tissue type. Therefore, it is reasonable to expect heterogeneity among different ROIs and homogeneity within one ROI. Figure 7.1(a) shows the workflow to integrate the ultrasound prior into a model-based optoacoustic reconstruction. From the ultrasound images, ROIs are segmented and labelled to form a prior mask. Then the regularization matrix $\boldsymbol{L}$ is constructed based on Equation 7.2. Finally, an appropriate regularization parameter is chosen to reconstruct optoacoustic images from the acquired optoacoustic data using the model-based scheme in Equation 2.15.

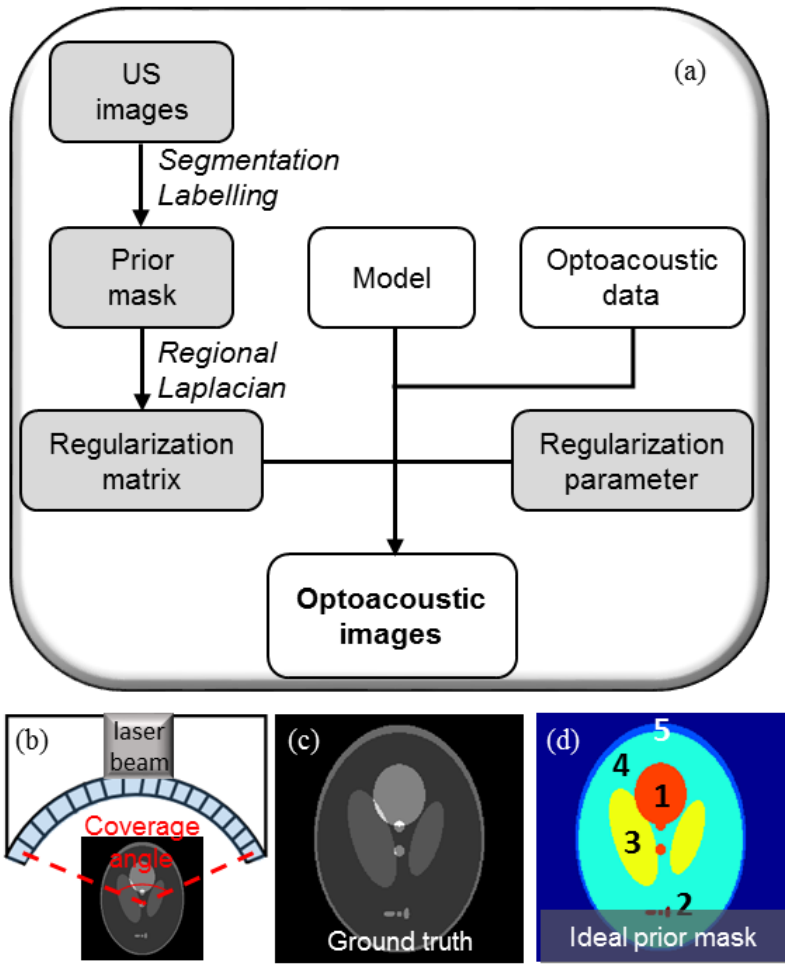

Figure 7.1. Block diagram of prior-integrated reconstruction, the related imaging setup and numerical phantom used for simulation. (a) Block diagram of prior-integrated reconstruction. (b) Imaging set-up, with detectors shown in blue. (c) Shepp–Logan phantom without noise (ground truth). (d) Segmented prior mask with 5 labelled ROIs (ideal prior mask).

7.2.3 Numerical simulation

A numerical Shepp-Logan phantom was used to simulate the optoacoustic signals based on Equation 2.13, where the model matrix **M** was calculated based on the probe shown in Figure 7.1(b) of the Acuity256 imaging system (introduced in Chapter 4). In addition, zero mean Gaussian noise was added to achieve a certain SNR. In other words, the simulated optoacoustic signal $\boldsymbol{p}_{sim}$ takes the form:

$$\boldsymbol{p}_{sim} = \mathbf{M}(\boldsymbol{x}_{SL} + \varepsilon), \quad (7.3)$$

where $\boldsymbol{x}_{SL}$ is the Shepp-Logan phantom without noise shown in Figure 7.1(c) and ε is zero mean Gaussian noise. The simulated optoacoustic signals $\boldsymbol{p}_{sim}$ were inverted using standard and prior-integrated reconstruction, and the performance of those two methods was assessed based on the reconstructed image quality using the metrics described in Section 7.2.5. In order to analyze the effect of various parameters on algorithm performance (noise level, coverage angle of the transducer array, segmentation accuracy, ROI labelling, and regularization parameter), we performed multiple simulations by modifying the Shepp-

Logan phantom and the ideal prior mask in Figure 7.1(d), which was segmented from the ground truth image.

The mentioned parameters were analyzed in 4 groups of simulations. In the first group (SIM1), different noise levels and coverage angels of the detector array were simulated; in the second group (SIM2), segmentation errors (e.g. too large or small ROIs), were mimicked with morphological operations; in the third group (SIM3), labelling errors were simulated; and in the fourth group (SIM4), the simulated signals were reconstructed with varying regularization parameters.

1) Noise and coverage angle (SIM1)

In order to analyze the robustness of the algorithm with respect to noise, we added different levels of white Gaussian noise ε to degrade the ground truth image $\boldsymbol{x}_{SL}$, achieving an SNR (dB) of 26, 20, 16.5, 14, 12, 10.5, 9.1, 8, 7 and 6. The ability of the algorithms to deal with the limited-view projections was analyzed by simulating the following coverage angles of the transducers: 200°, 175°, 150°, 125°, 100°, 75° and 50°. Except for this group, for all other simulations the default SNR was 26 dB and the default coverage angle was 125°.

2) Segmentation accuracy (SIM2)

Accurate image segmentation in the presence of noise is challenging. Therefore, we used morphological operations to mimic inaccurate segmentation. For the Shepp-Logan phantom, the exact segmented prior mask, termed the 'ideal prior mask', is shown in Figure 7.1(d). We eroded the ideal prior mask with a disk of diameter 2, 4, 6 or 8 pixels to simulate the case that the ROIs are segmented too small; and we dilated the ideal mask with a disk of diameter 2, 4, 6 or 8 pixels to simulate the case that the ROIs are segmented too large. Another potential segmentation error is the number of segmented regions, as for different segmentation methods, the number of segmented ROIs may vary. In order to analyze how this parameter affects the quality of the reconstructed images, we derived 5 prior masks based on the ideal prior mask. The first prior mask included only ROI 1, the second prior mask included ROI 1 and 2, and so on.

3) ROI labelling (SIM3)

After image segmentation, labelling the segmented ROIs, is a key step in the regional Laplacian method, since the labelling has a direct effect on N_k in Equation 7.2. In order to examine the effect of labelling a non-existing region, which mimics the case that a region is an efficient acoustic reflector but not a good optical absorber, we modified the Shepp-Logan phantom by removing the lowermost structure [Figure 7.4(a)] and labelled an independent non-existing ROI 2 in the prior mask [Figure 7.4(b)]. A further variant of labelling is to label multiple ROIs as the same tissue type. To simulate this case, we labelled the non-existing ROI 2 in the ideal prior mask with the same label as ROI 1 [Figure 7.4(c)].

4) Regularization parameter (SIM4)

For regularization problems, many methods have been developed to optimize the selection of regularization parameter λ. In this study, in order to analyze the effect of the prior mask

on the selection of the regularization parameter, we used the L-curve to find a proper λ for each prior mask and examined the reconstructed images with different λ.

7.2.4 Tissue imaging of healthy volunteers and patients

Procedures on human subjects were performed after obtaining their written informed consent. To image the radial artery, we scanned one healthy volunteer over the ventral side of the distal forearm with the Acuity256. To image the carotid, we scanned three healthy volunteers and five patients with diagnosed carotid atherosclerosis over the lateral cervical region of the neck on both sides, i.e. 6 healthy volunteers' datasets and 10 patients' datasets in total. Signal data were not averaged for either modality.

7.2.5 Image quality evaluation

In this study, we compared standard and prior-integrated reconstruction mainly in terms of several quantitative quality indicators of the reconstructed image, as described below.

1) CNR

As contrast is the most crucial factor to determine if a region can be differentiated from the background or not, we used CNR to quantify the improvement in image contrast. The CNR of an image was defined as follows [171]:

$$CNR = \frac{contrast}{noise} = \frac{|\mu_1 - \mu_2|}{\sqrt{{\sigma_1}^2 + {\sigma_2}^2}}, \qquad (7.4)$$

where μ_1, μ_2 and σ_1, σ_2 are the means and the standard deviations of, respectively, a given ROI and the background (defined as the whole image except for the ROI).

2) Structural SIMilarity Index (SSIM)

Since limited-view projections introduce deformations of structures, SSIM is an appropriate indicator to quantify the structural accuracy of the reconstructed images. SSIM is commonly used for measuring the similarity between two images based on an initial distortion-free image (ground truth) as reference [172]. It can be calculated as.

$$SSIM(x, y) = \frac{(2\mu_x\mu_y + c_1)(2\sigma_{xy} + c_2)}{({\mu_x}^2 + {\mu_y}^2 + c_1)({\sigma_x}^2 + {\sigma_y}^2 + c_2)}, \qquad (7.5)$$

where μ_x and ${\sigma_x}^2$ are, respectively, the mean and variance of x, with x representting the reconstructed image. μ_y and ${\sigma_y}^2$ are, respectively, the mean and variance of y, with y being the reference image (ground truth). The variable σ_{xy} is the covariance of x and y, while c_1 (0.01 in this study) and c_2 (0.03 in this study) stabilize division by a weak denominator.

7.3 Results

To demonstrate the performance of the two regularization schemes introduced in the Section 7.2, we performed 4 groups of simulations (SIM1: different noise level and coverage angle; SIM2: segmentation errors; SIM3: labelling errors; and SIM4: varying regularization parameters) and reconstructed 2 groups of clinical datasets – one for radial artery images

and one for carotid artery images. The reconstruction results for the numerical phantoms are presented in Section 7.3.1, and the results for the clinical datasets are shown in Section 7.3.2.

7.3.1 Simulations

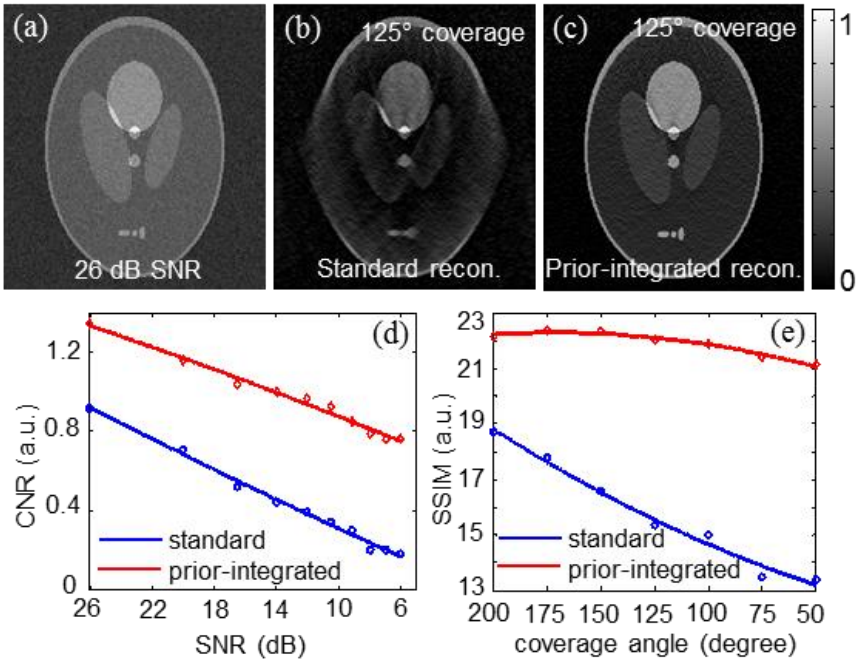

Figure 7.2. Integrating US priors into the OA reconstruction enhances the contrast and reduces limited-view artifacts. (a) Shepp–Logan phantom with zero-mean Gaussian noise (26 dB SNR). (b-c) Reconstructed image under a 125° coverage angle with (b) standard or (c) prior-integrated reconstruction. (d) CNR of the reconstructed images at different noise levels following standard or prior-integrated reconstruction. (e) Variation of SSIM of the reconstructed images with respect to the coverage angle.

Figure 7.2 shows the results of SIM1, which demonstrates that for varying SNR and coverage angle, prior-integrated reconstruction can efficiently enhance the contrast and reduce the limited-view artifacts. Figure 7.2(a) shows the degraded image of the Shepp-Logan phantom of 26 dB SNR. Figures. 7.2(b) and 7.2(c) show, respectively, standard and prior-integrated reconstruction of Figure 7.2(a) under the default coverage angle (125°). In Figure 7.2(b), both the structural deformation due to limited-view and the intensity fluctuation within the same region due to noise can be clearly seen. These artifacts are reduced by incorporating priors into the reconstruction [see Figure 7.2(c)]. Figure 7.2(d) shows the CNR of the reconstructed images for varying SNR. For linearly decreasing SNR, the CNR of the images also decreases linearly. However, the CNR of the prior-integrated reconstructions decreases more slowly than the CNR of the standard reconstructions, while the CNR of the prior-integrated reconstruction outperforms the one of the standard reconstruction at all SNR levels. Figure 7.2(e) shows the SSIM of the reconstructions for varying coverage angles. With standard reconstruction, the structural similarity of the reconstructed images decreases linearly with decreasing coverage angle. However, with prior-integrated reconstruction, the SSIM of the reconstructed images remains relatively unchanged even when the coverage angle decreases dramatically. Therefore, the prior-integrated reconstruction is demonstrated to efficiently reduce limited-view artifacts and to contribute to a better CNR than standard reconstruction in all simulations.

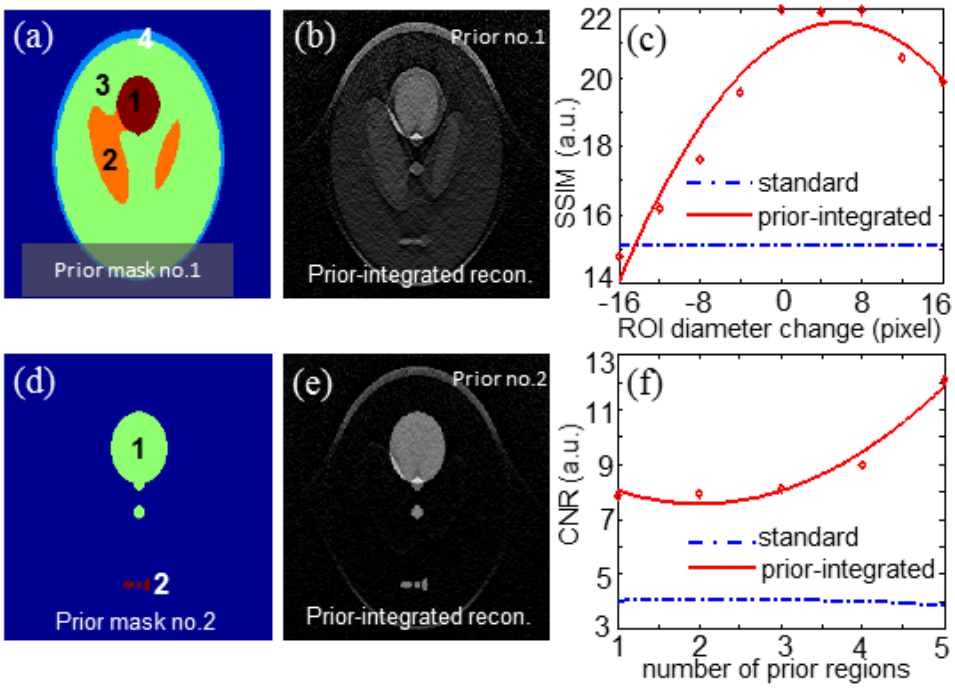

Figure 7.3. Effects of segmentation accuracy and the number of ROIs on prior-integrated reconstruction. (a) An inaccurately segmented prior mask, which is generated by the erosion of the ideal prior mask in Figure 1d with a disk of diameter 6 pixels. (b) Reconstruction of the noisy phantom (Figure 7.2a) using the prior mask in panel (a). (c) Variation of SSIM of the reconstructed images with respect to erosion and dilation. (d) A prior mask with only 2 ROIs. (e) Reconstruction of the noisy phantom in Figure 7.2(a) using the prior mask in panel (d). (f) Variation of the CNR of ROI 1 with respect to the number of ROIs ROIs were added according to their labels in Figure 7.1(d).

Figure 7.3 shows the results of SIM2, which demonstrates the effect of segmentation accuracy with respect to the size and the number of the segmented ROIs on the reconstructed images. Figure 7.3(a) shows an inaccurately segmented prior mask. Figure 7.3(b) shows the reconstruction result of the degraded phantom in Figure 7.2(a) using the prior mask in Figure 7.3(a). On this image, we can see that the true boundary of each ROI remains while the prior mask introduces false boundaries inside each ROI, which is expected to be reflected by a lower SSIM index. Figure 7.3(c) shows the SSIM in the presence of various segmentation errors. When there is no segmentation error, or the segmented ROI is slightly larger than the true case, the SSIM of the reconstructed images with prior-integrated reconstruction is optimal. However, if the segmented ROI is obviously smaller or larger than the true case, strong false boundaries start to appear in the reconstructed images, which reduces the SSIM values. Figure 7.3(d) shows another type of inaccurate prior mask that includes only two ROIs. Figure 7.3(e) presents the reconstruction result of Figure 7.2(a) using the prior mask in Figure 7.3(d). It can be seen that due to the prior mask, the structure and intensity of ROI 1 and 2 are well recovered, while the remainder of the image is poorly reconstructed. Figure 7.3(f) shows the variation in CNR for ROI 1 as the number of ROIs in the prior mask changes: more ROIs in the prior mask translates to better CNR. Regardless of the number of ROIs in the segmented prior mask, CNR is always better with prior-integrated reconstruction than with standard reconstruction. These analyses suggest that in prior-integrated reconstruction, when there is a clear target region to analyze, it is better to segment only the target region

and treat the rest of the image as one region. This can achieve high CNR inside the target region without introducing extra false boundaries in other regions.

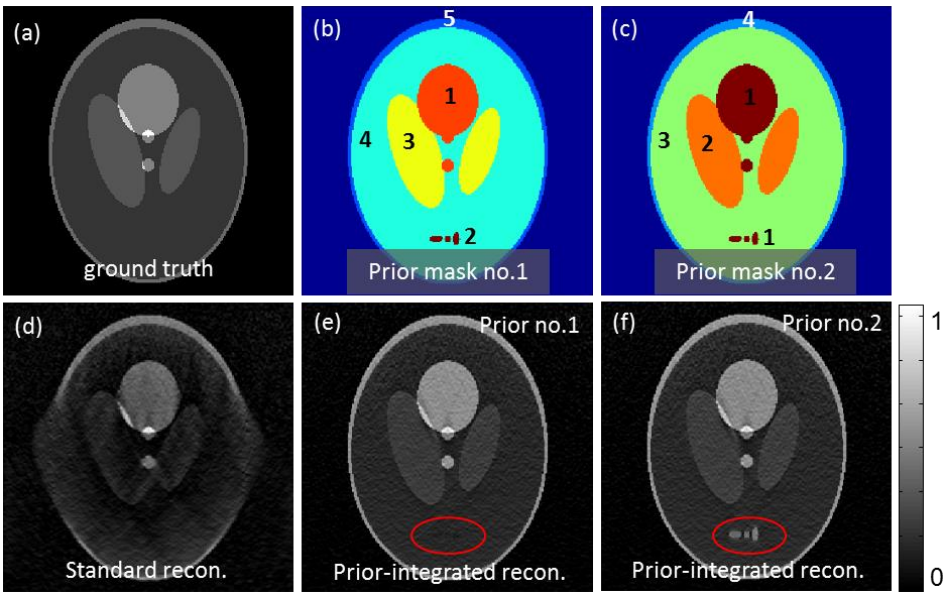

Figure 7.4. Effects of ROI labelling on prior-integrated reconstruction. (a) A modified Shepp-Logan phantom with the lowermost structure removed. (b-c) Inaccurate prior masks in which (b) a nonexistent ROI has been added, or (c) the nonexistent ROI has been added to ROI 1. (d-f) Reconstruction of the noisy phantom with (d) standard reconstruction or with prior-integrated reconstruction using (e) prior mask no. 1 or (f) prior mask no. 2. The red ellipse in panels (e) and (f) indicates the location of the ROI that was assigned different labels, introducing a false positive in panel (f).

Next, we examined the effects of ROI labelling on prior-integrated reconstruction (SIM3). Figure 7.4 shows that erroneous labelling of the segmented ROIs in the prior mask after segmentation might introduce false positives. Figure 7.4(a) is the modified Shepp-Logan phantom, which was the ground truth in this simulation. Figure 7.4(b) shows an erroneous mask on which a nonexistent region is labelled as ROI 2. Figure 7.4(c) shows that a nonexistent region is labelled as the same tissue type as ROI 1. Figure 7.4(d) is the reconstructed image using standard reconstruction. Figure 7.4(e) is the reconstruction result of prior-integrated reconstruction using the prior mask in Figure 7.4(b), which demonstrates that labelling a nonexistent region as an independent ROI in the prior mask introduces no error to the reconstructed image. Figure 7.4(f) shows the prior-integrated reconstruction result with the prior mask on panel 7.4(c), which demonstrates that labelling a nonexistent region to an existing region definitely introduces false positive. Therefore, two separated or discontinuous regions should never be labelled a priori as the same tissue type.

Since the regularization parameter is important for all regularization methods, SIM4 was performed. Figure 7.5 demonstrates that the prior mask affects the selection of an appropriate regularization parameter. Figure 7.5(a) shows the ideal prior mask as one example of the prior mask. Figure 7.5(b) shows a prior mask including only one ROI as another example of the prior mask. Figure 7.5(c) presents the L-curve corresponding to the masks in panel 7.5(a) and 7.5(b). It can be seen that different prior masks lead to different L-curves, specifically different corner points of the L-curves. As the corner point of the L-curve is the basis to find an appropriate λ, it is necessary to examine the choice of the λ when the

prior mask changes. Figure 7.5(d)–7.5(f) show the reconstructed images of Figure 7.2(a) using the prior mask in panel 7.5(b) with a small, appropriate and large λ. With a small regularization parameter, the prior-integrated reconstruction is similar to the standard reconstruction. With an appropriate regularization parameter, the ROI can be reconstructed with higher accuracy and maintain the information on the background in prior-integrated reconstruction. With a large regularization parameter, the prior dominates the reconstruction result and basically only the prior mask is reconstructed with all other information being discarded.

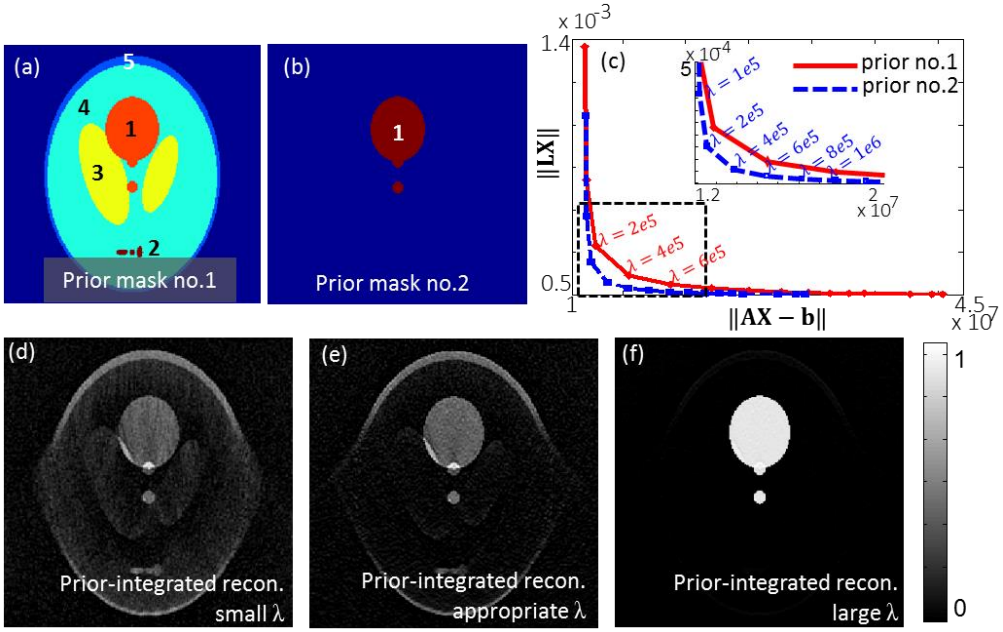

Figure 7.5. The prior mask affects the choice of appropriate regularization parameter. (a) Ideal prior mask. (b) A prior mask that has only ROI 1. (c) L-curves corresponding to the prior masks in panels (a) and (b). (d-f) Reconstruction of the noisy phantom in Figure 2a with (d) a small regularization parameter (1e5), (e) an appropriate regularization parameter (4e5) or (f) a large regularization parameter (1e7).

7.3.2 Clinical datasets

Based on the simulation results, we proceeded to test the performance of the prior-integrated method for reconstruction of clinical datasets. We focused on the distal forearm, where a precise longitudinal measurement of radial artery dimensions allows assessment of cardiovascular health [173], and on the carotid artery in the lateral aspect of the neck, which is the major source for cerebrovascular disease and stroke [174]. For imaging of the radial artery, optoacoustic images were reconstructed at the wavelength of 800 nm, which allows detection of both oxygenated and deoxygenated blood. For imaging of the carotid artery, optoacoustic images were reconstructed at wavelengths of 850 nm to detect oxygenated blood and of 930 nm to detect lipid.

Figure 7.6 shows that prior-integrated reconstruction improves the contrast of the radial artery deep in the distal forearm of a healthy volunteer as compared to the standard reconstruction. Figure 7.6(a) – 7.6(c) show the reconstruction results of the radial artery at 3.5 mm, 7.4 mm and 11.6 mm depth, respectively, using the standard reconstruction. Figure

7.6(d) – 7.6(f) show the reconstructed images of the radial artery using the prior-integrated reconstruction at a depth of 3.5 mm, 7.4 mm and 11.6 mm, respectively. The zoomed-in images of the radial artery show that the prior-integrated method reconstructs the radial artery with much better contrast, which allows better visualization even when the radial artery is lying in deep tissue.

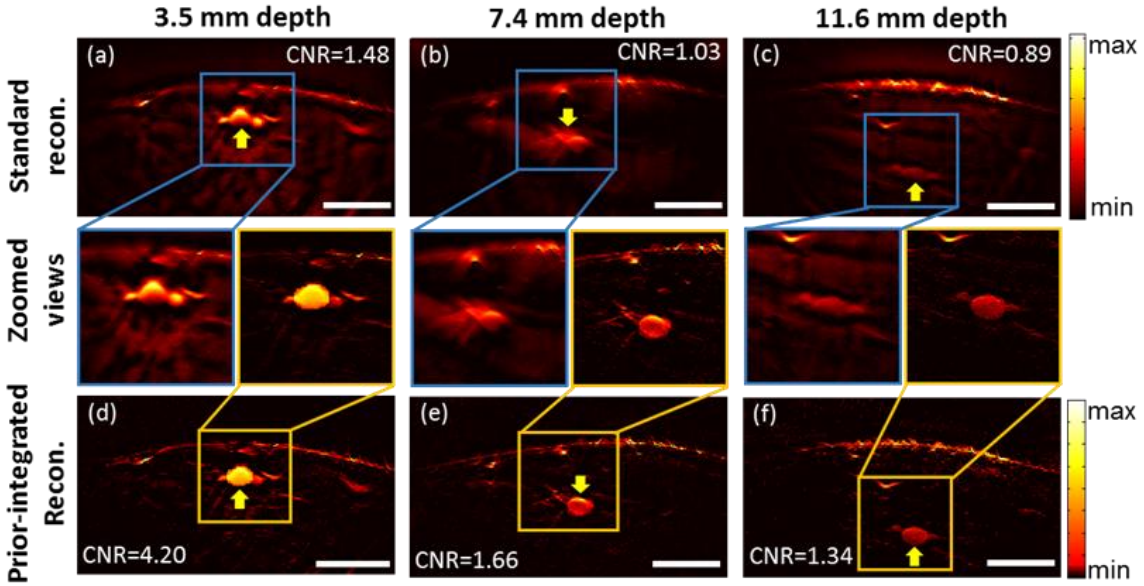

Figure 7.6. Prior-integrated reconstruction improves the contrast of the radial artery (yellow arrow) deep in tissue. Standard reconstruction of the radial artery at 800 nm at depth (a) 3.5 mm, (b) 7.4 mm and (c) 11.6 mm. Prior-integrated reconstruction of the radial artery at 800 nm at depth (d) 3.5 mm, (e) 7.4 mm and (f) 11.6 mm. The scale bar is 1 cm.

Figure 7.7 compares the performance of prior-integrated and standard reconstruction for reconstructing images of the carotid artery of an atherosclerosis patient and of a healthy individual. Figure 7.7(a) – 7.7(i) are the results of patient with proven carotid atherosclerosis. Figure 7.7(a) is the prior mask used for reconstructing the carotid at 850 nm. Figure 7.7(b) is the reconstructed optoacoustic image at 850 nm using the prior mask in panel 7.7(a). Figure 7.7(c) is the reconstructed image at 850 nm using the standard reconstruction. Comparing Figure 7.7(b) and 7.7(c), it can be seen that the carotid is not visible against the background in the standard reconstruction, but it is visible in the prior-integrated reconstruction. Since the major absorber is hemoglobin (blood in the carotid) at 850 nm and lipid (contained in plaque) at 930 nm, the prior mask at 930 nm, corresponding to the plaque, is different from the prior mask of the carotid at 850 nm. Figure 7.7(d) – 7.7(f) show the reconstructed optoacoustic images at 930 \nm with prior-integrated reconstruction and standard reconstruction, respectively. With the standard reconstruction, the plaque in the carotid artery is not recognizable from the optoacoustic images, but with the prior-integrated reconstruction, the lesion is clearly detectable. Figure 7.7(g) is the co-registered ultrasound image from which the prior masks are segmented. Figure 7.7(h) is the overlay of US and the optoacoustic images of panel 7.7(b) and 7.7(e). Figure 7.7(i) is the overlay of the US and the optoacoustic images of panel 7.7(c) and 7.7(f).

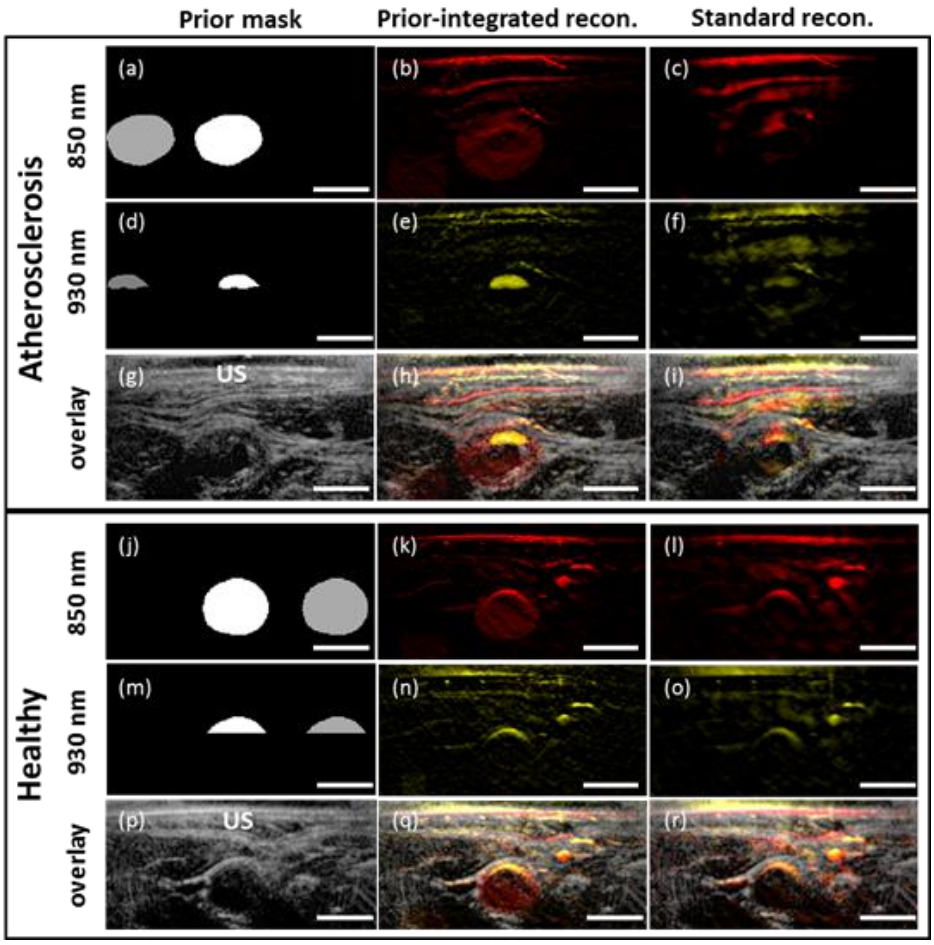

Figure 7.7. Prior-integrated reconstruction improves the contrast of the carotid and the detectability of a plaque inside the carotid. The results of an atherosclerosis patient are shown in panels (a)-(i). (a) A prior mask for the carotid. (b-c) Reconstructed images at 850 nm using (b) prior-integrated and (c) standard reconstruction. (d) A prior mask for the lesion inside the carotid. (e-f) Reconstructed images at 930 nm using (e) prior-integrated and (f) standard reconstruction. (g) US image of the neck region. (h) Overlay of panels (b), (e) and (g). (i) Overlay of panels (c), (f) and (g). (j-r) The results of a healthy volunteer are shown in panel. (j) A prior mask of the carotid. (k-l) Reconstructed images at 850 nm using (k) prior-integrated and (l) standard reconstruction. (m) Prior mask of a nonexistent lesion inside the carotid. (n-o) Reconstructed images at 930 nm using (n) prior-integrated and (o) standard reconstruction. (p) US image of the neck region. (q) Overlay of panels (k), (n) and (p). (r) Overlay of panels (l), (o) and (p). The scale bar is 1 cm. The grey regions in the prior masks are the control for the true ROI in white.

Figure 7.7(j) – 7.7(r) are the results of a healthy volunteer as the control. Figure 7.7(j) is the prior mask at 850 nm. Figure 7.7(k) – 7.7(l) are the reconstructed optoacoustic images at 850 nm using the prior mask in panel 7.7(j) and the standard reconstruction, respectively. The carotid is well recovered by the prior-integrated method but only the upper boundary is visible with standard reconstruction. Figure 7.7(m) is a manually drawn prior mask including a non-existing lesion and used for the reconstruction at 930 nm to examine whether it introduces false positive or not. Figure 7.7(n) and 7.7(o) are the reconstructed optoacoustic images at 930nm with prior-integrated reconstruction and standard reconstruction, respectively. The two reconstruction methods gave similar images; the prior-integrated method did not introduce false positives. Figure 7.7(p) is the co-registered ultrasound image from which the prior mask in panel 7.7(j) is segmented. Figure 7.7(q) is the overlay of panel

7.7(p) and the optoacoustic images on panel 7.7(k) and 7.7(n). Figure 7.7(r) is the overlay of the 7.7(p) and the optoacoustic images of panel 7.7(l) and 7.7(o).

A comparison of the results using prior-integrated and standard reconstruction shows that prior-integrated reconstruction is efficient in improving the contrast of the carotid and making the carotid visible directly from reconstructed optoacoustic images. The results obtained at 930 nm shows that the prior-integrated method increases the detectability of the plaque, which is not visible with standard reconstruction. At the same time, using priors does not introduce a false positive, such that no false lesion is detected in the healthy volunteer.

Finally, Figure 7.8 shows the intensity analysis of the datasets presented in Figure 7.7 and extends the analysis to the full datasets of 10 datasets from patients and 6 datasets from healthy individuals. The y-axis is the intensity ratio of the target ROI and the reference ROI (white region to grey region in the prior masks in Figure 7.7). Figure 7.8(a) – 7.8(b) show that at 800 nm, both prior-integrated and standard reconstruction give a similar intensity ratio for patients and healthy volunteers. This is expected since the image intensity from the target ROI at 800 nm is mainly due to the blood in the carotid, and hence, there should be no significant difference between atherosclerotic patients and healthy volunteers. However, a significant intensity difference is expected at 930 nm, as lipids are the main absorbers at 930 nm, and the patients with carotid artery disease frequently have atherosclerotic plaques that contain lipids, while the healthy volunteers do not. As expected, prior-integrated reconstruction shows a significant difference between the intensity ratios of patients and healthy volunteers [Figure 7.8(c)], while the standard reconstruction fails to show a clear difference [Figure 7.8(d)]. From Figure 7.8(c) and 7.8(d), we can see that there is a difference in the intensity ratio distribution depending on whether reconstruction incorporates US priors. These results suggest that such priors can improve optoacoustic image quality, and therefore clinical usefulness, in real clinical datasets.

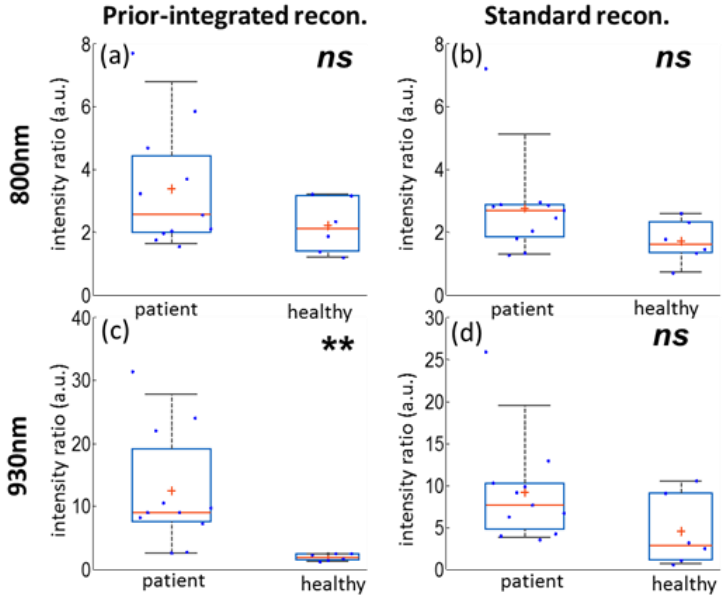

Figure 7.8. Statistical analysis of carotid images from atherosclerosis patients and healthy volunteers. (a-b) Intensity ratio of the reconstructed images at 800 nm using (a) prior-integrated or (b) standard reconstruction. (c-d) Intensity ratio of the reconstructed images at 930 nm using

*(c) prior-integrated reconstruction and (d) standard reconstruction. ns: difference between two groups is not significant, p>0.05; **: difference between two groups is very significant, p<0.01.*

7.4 Discussion and outlook

Simultaneous recording of co-registered ultrasound and optoacoustic images using a hybrid handheld system offers not only a comprehensive anatomical ultrasound-based validation of optoacoustic images, but also valuable prior information for improving optoacoustic reconstructions. Ultrasound priors can be efficiently incorporated into optoacoustic model-based reconstruction by a regional Laplacian regularization method based on segmented ultrasound images. This prior-integrated reconstruction is shown to improve the optoacoustic image quality and the detectability of structures in deep tissue.

In all clinical datasets and simulations that were considered, we found that the prior-integrated reconstruction improves the optoacoustic image quality in terms of structural similarity, contrast, and detectability of certain ROIs. In particular, we demonstrate that the radial artery can be reconstructed with a sharp contrast even deep in tissue, and that functional features of plaques in the carotid of atherosclerosis patients can be extracted with prior-integrated reconstruction, which is not possible with the considered standard reconstruction.

In addition, the regional Laplacian method is found to be an efficient way to at least partially compensate the information loss due to limited-view detection. For example, vertical structures with acoustic contrast can partially be recovered, which is known to be a major problem for limited-view geometry systems [154]. Thus, our approach can help complete boundaries in optoacoustic images even in the regions not fully covered by detectors.

Similar regional Laplacian methods have been applied to integrate prior information in multi-modal imaging in other fields [175-179]. While in these cases, priors are taken from a higher resolution modality and integrated into a lower resolution modality, we demonstrate for the first time that priors from one modality can improve the reconstruction in a second modality when the two modalities offer similar resolution, as is the case for OPUS systems.

Previous studies integrating prior information did not examine how their method performed in the presence of specific, isolated factors that can affect reconstruction quality. Here we analyzed the influence of certain parameters during prior integration on the final reconstruction quality, we found that the segmentation accuracy of the prior masks and the regularization parameter have a strong influence on the reconstructed image quality. In addition, labelling unconnected regions as the same tissue type can introduce false positive to the results. In order to avoid this, the labelling of the prior mask is suggested to follow the connectivity of the regions, i.e. two unconnected regions should not be labelled a priori as the same tissue type.

For further improvement of the proposed method, automatic segmentation of the prior mask could be considered. For example, superpixel segmentation might be an appropriate way to automatically segment the priors. Even though superpixels might oversegment the image, it is expected to find the relevant edges in the ultrasound image [180]. In general, automatic segmentation should avoid the bias introduced by manual segmentation. Also, automatic

selection of the regularization parameter should be considered, since using the L-curve is a time consuming method [181].

In summary, this chapter proposes a novel perspective to further enhance the capabilities of handheld OPUS imaging systems. It is shown that the use of ultrasound priors can facilitate optoacoustic image reconstruction. The developed prior-integrated method improves the quality of the reconstructed optoacoustic image and increases the detectability of deep-lying structures. The demonstrated improvements will allow more accurate image analysis in applications requiring high contrast deep in tissue, such as vascular imaging, and vascularity analysis of soft-tissue tumors. Moreover, by achieving higher contrast in the target ROIs, our method shows great potential for increasing the diagnostic information available to clinicians to support diagnosis, characterization and monitoring of disease and response to therapy.

8. Ultrasound SoS prior integrated optoacoustic reconstruction

8.1 Motivation

As being demonstrated in last chapter, in OPUS imaging, the structural information in ultrasound images can be integrated as prior into optoacoustic reconstruction to improve optoacoustic image quality, not just be used to provide basic anatomical orientation or post hoc validation to aid the interpretation of optoacoustic images. In addition to structural information, ultrasound images also carry information about the acoustic properties of the imaged sample, such as the SoS distribution which is one of the most important parameters for optoacoustic reconstruction and of particular importance in clinical imaging (demonstrated in Chapter 5).

However, due to the simplicity of implementation using uniform SoS and the difficulty to derive the spatial-variant SoS distribution in imaged samples, most optoacoustic reconstruction algorithms assume uniform SoS in the imaged region [64] or inside the sample, i.e. dual-SoS model [102, 103, 182] along with straight ray propagation assumption, which is contrary to the acoustically inhomogeneous nature of tissue. When the real SoS distribution is heterogeneous and different from the above assumption, the discrepancies in SoS can lead to reduced image contrast and resolution, distortions in the reconstructed structures, and so reduce their clinical value. Therefore, the estimation of a close-to-reality SoS distribution should be pursued not only because it enables image correction, but also as a way of improving image accuracy which paves the way for quantitative OPUS imaging.

In OPUS imaging, a common way to estimate the SoS distribution is using UTT [116, 118], which has previously been shown to allow accurate reconstruction of the SoS distribution in phantom studies [183-185] and *ex vivo* studies [183, 185]. In UTT, the acoustic properties of sample are estimated by sending a series of ultrasonic pulses through the sample and measuring the resulting wavefield with an array of ultrasound transducers on the opposite side of the ultrasound emitters. The calculation of the SoS is based mainly on the slowness (i.e. reciprocal of the SoS) [183] difference between with and without a sample in the imaged region. Although this severs well for the purpose of SoS estimation, it needs full-view data acquisition in transmission mode and not applicable to handheld OPUS systems which is working on reflection mode. A few methods have been developed to derive the SoS distribution with reflection-mode ultrasound imaging systems [186-189]. Depend on whether an extra reflector to mimic the UTT is needed or not, these methods can be classified into two categories. For the category which needs an extra reflector to enable full transmission and reflection of the ultrasound pulse from the emitters back to the receivers [189], it is not feasible in clinical imaging, because in clinical imaging, the ultrasound waves will be fully reflected by bones in human body. Besides, adding an extra reflector also loses the portability of handheld probes. For the other category, the slowness difference is extracted from the phases of the signals reflected by the reflectors inside the sample at different incident angles. Although this is an interesting perspective to derive the SoS distribution from reflection-mode ultrasound imaging, the reconstructed SoS distribution

suffers from low resolution and heavy artifacts [186]. Moreover, all above studies have been done using either phantom or small-animal data, no work has been done for clinical studies, in which the variation of SoS inside the sample is more significant. Therefore, we developed an iterative ultrasound-image-driven method to estimate the SoS distribution, which needs no extra UTT measurements or extra adaption to the handheld probe and is easily applicable for all handheld OPUS systems.

In this chapter, a method to reconstruct SoS distribution in imaged samples from reflection-mode ultrasound images using an iterative nonlinear optimization scheme is proposed and the proposed method is demonstrated with simulations, phantoms and clinical datasets from clinical OPUS system. Different from the conventional methods which are based on slowness difference, the proposed method derives the spatial-variant SoS distribution by modeling the ultrasound image as a function of SoS, which is based on the fact that the intensity of ultrasound images is the representation of acoustic impedance and encodes the SoS distribution of the imaged samples. In addition, bent ray propagation model based on fast marching method (FMM) is used to further improve optoacoustic image quality and accuracy.

8.2 Ultrasound-image-driven SoS reconstruction

Since the contrast mechanism of an ultrasound image is the change in acoustic impedance (which is the combination of the SoS and density) of different media encountered during sound wave propagation, the acoustic properties of the sample, such as the SoS distribution, is encoded in the intensity of ultrasound images and should be possible to be derived.

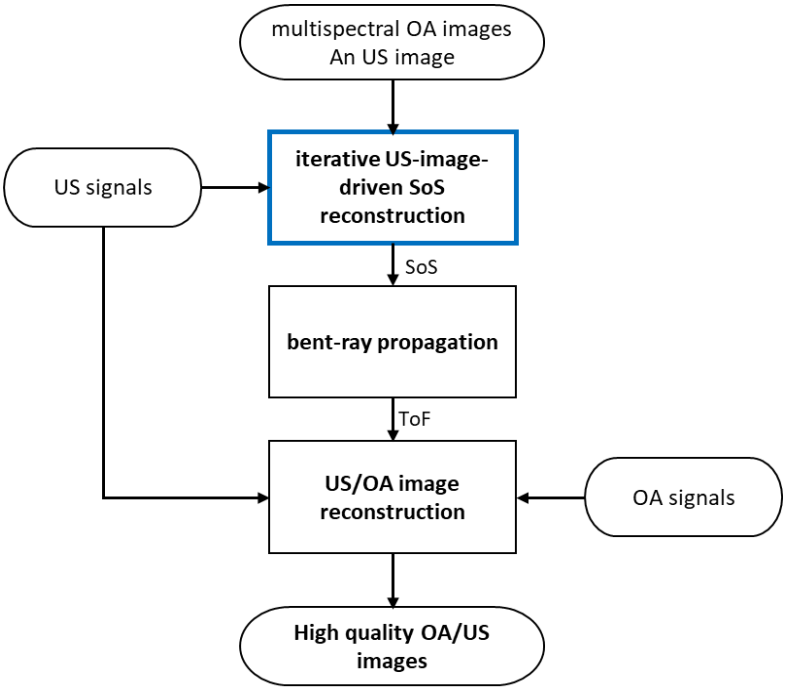

Figure 8.1. Ultrasound-image-driven high-quality reconstruction scheme. OA - optoacoustic; US - ultrasound; SoS – Speed of Sound; ToF – Time of Flight.

Figure 8.1 shows the workflow of the high-quality reconstruction framework which is built upon the proposed ultrasound-image-driven SoS reconstruction method. The workflow

comprises three modules. In the first module, a multispectral optoacoustic image stack, its co-registered ultrasound image, and the ultrasound signals are used as the inputs of the proposed iterative ultrasound-image-driven SoS reconstruction to estimate the SoS distribution inside the imaged region. In the second module, with the spatial-variant SoS output from last module, a bent-ray propagation model is applied to calculate the ToF from each transducer element to all grid points in the full FOV of the transducer array. In the third module, optoacoustic signals and ultrasound signals are reconstructed using the ToF output from the second module with the reconstruction methods introduced in Chapter 2 and 6, respectively. Since the calculated ToF is based on close-to-reality SoS distribution and bent-ray propagation model, the reconstructed optoacoustic and ultrasound images are of higher accuracy in terms of the dimension, location and shape of structures and better image quality than the ones reconstructed with uniform or dual SoS straight ray propagation models.

8.2.1 Iterative ultrasound-image-driven SoS reconstruction

Figure 8.2 shows the workflow of the proposed iterative ultrasound-image-driven SoS reconstruction method. In this method, we model the ultrasound image as a function of SoS and use model-based nonlinear optimization to reconstruct the SoS in the imaged sample. The inputs of the model-based SoS reconstruction are the raw ultrasound image and initial SoS guess, while the output is the estimated SoS distribution. According to a preset criterion, the calculated SoS is either forwarded to form a new ultrasound image for another iteration or output as the optimal estimation achieved. Since the model-based SoS reconstruction is a non-linear optimization process which requires a good initial guess, a data-driven clustering method is applied to segment different tissues and then assign the corresponding SoS values to them according to literature, which is used as initial guess to start the iterative process of deriving the SoS distribution based on ultrasound images. The three major steps highlighted in Figure 8.2, i.e. tissue segmentation based on data-driven clustering, the model-based SoS reconstruction, and bent-ray propagation are introduced in detail in the following sections.

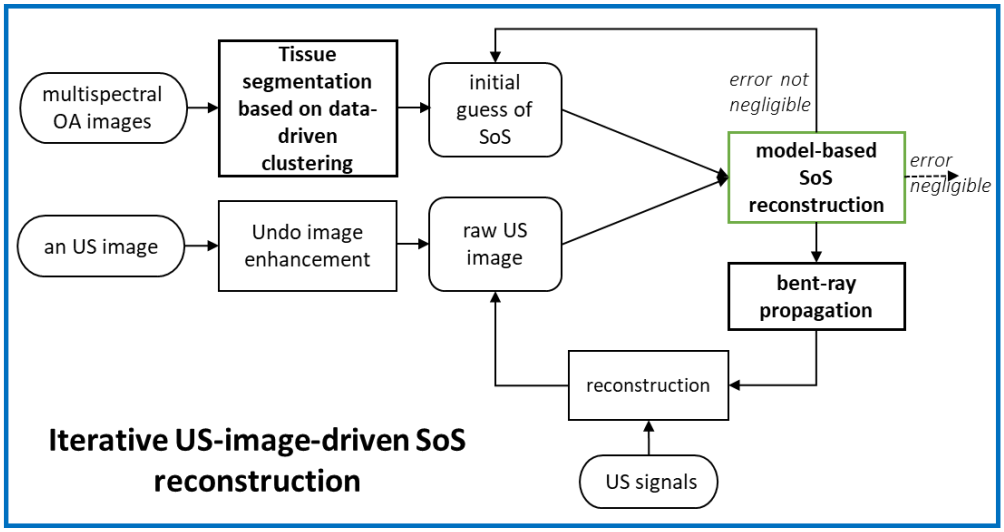

Figure 8.2. Framework of iterative US-image-driven SoS reconstruction.

8.2.2 Model-based SoS reconstruction

For handheld ultrasound probes, the detected ultrasound signals are the reflected echoes of the emitted ultrasound wave from each transducer element, which means that the contrast of reconstructed ultrasound images are mainly affected by the reflectivity of the structures inside the imaged sample. Moreover, the reflectivity R is the function of SoS and density as follows (only normal incidence is considered):

$$R(\rho, c) = \left(\frac{\rho_2 c_2 - \rho_1 c_1}{\rho_2 c_2 + \rho_1 c_1}\right)^2, \qquad (8.1)$$

where ρ is the density and c is the SoS of the medium, subscript 1 and 2 stand for two media beside an interface. The reflectivity in normal incidence stays the same whether the sound is travelling from medium 1 to medium 2 or vice versa. The production of density and SoS is termed as acoustic impedance of a material. From Equation 8.1, it can be seen that the proportion of energy reflected depends on the acoustic impedances of the two media beside an interface. The greater the difference is, the greater the fraction reflected is and the less the fraction transmitted is. According to the reported values of tissue density and SoS in literature [190], the density and SoS of most soft tissue types follow a linear relationship which can be modeled with linear regression. In this study, we use the density and SoS values of water, blood, fat, liver, kidney, brain, heart, muscle, skin reported in Ref. [190] for linear regression as following:

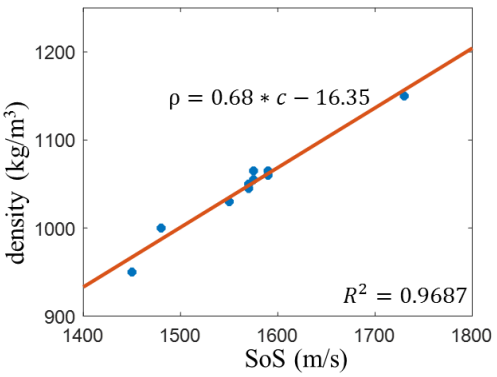

material	density (kg/m³)	SoS (m/s)	material	density (kg/m³)	SoS (m/s)
water	1000	1480	brain	1030	1550
blood	1055	1575	heart	1045	1570
fat	950	1450	muscle	1065	1575
liver	1060	1590	muscle	1065	1590
kidney	1050	1570	skin	115	1730

Figure 8.3. Linear regression of tissue density and SoS.

With the linearity between tissue density and SoS, Equation 8.1 can be simplified as a single variable equation:

$$R(c) = \left[\frac{0.68(c_2{}^2 - c_1{}^2) - 16.35(c_2 - c_1)}{0.68(c_2{}^2 + c_1{}^2) - 16.35(c_2 + c_1)}\right]^2. \qquad (8.2)$$

The intensity of a raw ultrasound image reconstructed with the method introduced in Chapter 6 is mainly decided by the reflectivity of the tissue, acoustic attenuation during ultrasound wave propagation and limited-view detection, we assume that the ultrasound image intensity can be expressed as a function of SoS distribution and simulated as Figure 8.4 shows.

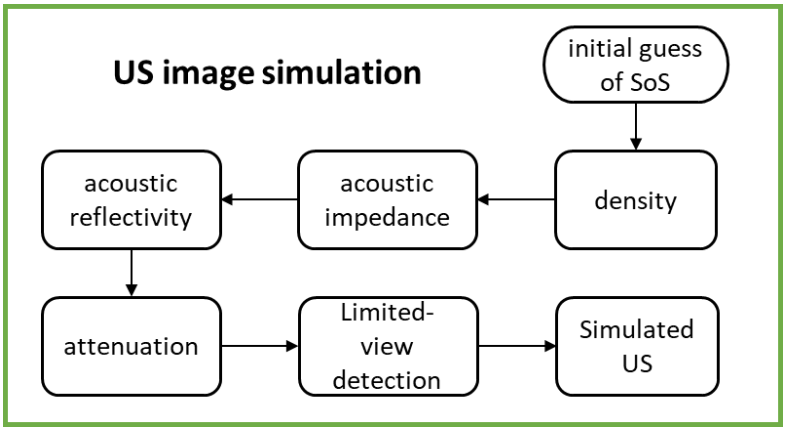

Figure 8.4. Workflow of ultrasound image simulation.

In order to model an ultrasound image as the function of the SoS and simulate ultrasound images using the workflow in Figure 8.4, the process from an ultrasound pulse being generated to an ultrasound image being formed in OPUS system should be recapped. When OPUS system works in ultrasound modality, an acoustic pulse is emitted from a known location outside the object. The acoustic wave travels through the object until being reflected by the acoustic reflectors. The resulting pressure wavefield is recorded by a collection of ultrasonic transducers surrounding the object. This process is repeated for several emitter locations corresponding to different views around the object.

The initial excitation pulse generated by the emitter can be written as:

$$p_{init}(t) = a(t)e^{i2\pi f_0 t}, \quad (8.3)$$

where a is the amplitude of the ultrasound pulse and f_0 is the carrier frequency. The ultrasound wave travels through the FOV until being reflected by an acoustic reflector with reflectivity R . The reflected ultrasound echo is written as

$$p(t) = p_{init}(t) \cdot R(\boldsymbol{r}), \quad (8.4)$$

where $\boldsymbol{r}$ is the spatial location of the reflectors in the imaged region. After being reflected by reflectors, most of the sound waves travel back towards the ultrasound transducers.

During ultrasound wave propagation in medium, the energy would loss due to viscosity, scattering and absorption of the medium, which causes frequency- and distance-dependent reduction of the amplitude of detected ultrasound signals. We model the amplitude reduction of the ultrasound wave with an exponential decay, which is most commonly used in reported studies [81]:

$$p(t) = p_{init}(t) \cdot R(\boldsymbol{r}) \cdot e^{-2|\boldsymbol{r}'-\boldsymbol{r}|\alpha_{0f}|f|^n}, \quad (8.5)$$

where α_{0f} is a material-related acoustic attenuation coefficient, n is a real positive constant, f is the central frequency of the ultrasound wave and d is the propagation distance of the acoustic wave. For water, $\alpha_{0f} = 0.00217\text{dB} \cdot \text{MHz}^{-1} \cdot \text{cm}^{-1}$ and n is 2; for tissues, n is 1 and $\alpha_{0f} \approx 0.5\ \text{dB} \cdot \text{MHz}^{-1} \cdot \text{cm}^{-1}$ [82]. In the considered case (Acuity 256), the central

frequency/carrier frequency is 6 MHz and distance d comprises 2 parts: couplant (4 cm) and the travelling distance inside sample.

Since each transducer is focused and of limited-detection aperture, the detected ultrasound echo from the whole FOV is

$$p_d(t) = \int_{\Omega_0} \left[p_{init}(t) \cdot R(\boldsymbol{r}) \cdot e^{-2|\boldsymbol{r}'-\boldsymbol{r}|\alpha_{f0}} \right] d\Omega_0/\Omega_0, \qquad (8.6)$$

where $d\Omega_0$ stands for the detection aperture of the transducer and $\Omega_0 = 4\pi$ for spherical and cylindrical geometry. In tomography, several detector elements at different spatial locations along the surface are used for detection, so $d\Omega_0/\Omega_0$ denotes the weighting factor of the contribution of one single detection element in each imaging event to the reconstructed p at a point $\boldsymbol{r}'$.

Assume the excitation pulse is narrow band, last equation can be approximated as

$$p_d = \int_{\Omega_0} \left[A \cdot R(\boldsymbol{r}) \cdot e^{-2|\boldsymbol{r}'-\boldsymbol{r}|\alpha_{f0}} \right] d\Omega_0/\Omega_0. \qquad (8.7)$$

where A is a constant. According to the working scheme shown in Figure 8.7(d), the intensity of reconstructed ultrasound images can be written as follows:

$$I(\boldsymbol{r}) = \boldsymbol{W}(\boldsymbol{r}) \cdot A \cdot \boldsymbol{R}(\boldsymbol{r}) \cdot \boldsymbol{T}(\boldsymbol{r}) \cdot e^{-2|\boldsymbol{r}'-\boldsymbol{r}|\alpha_{f0}} \cdot \boldsymbol{\Omega_i}(\boldsymbol{r}), \qquad (8.8)$$

where N is the total number of the imaging events (N=256 in this study), $\boldsymbol{\Omega_i}$ is the weighting matrix of ith imaging event which is decided by coverage angle, and $\boldsymbol{W}$ is the weighting matrix created according to the norm direction of the structure in each grid (the detailed information about how to create these two matrixes is presented in Figure 8.5), and $\boldsymbol{T}(\boldsymbol{r})$ is the accumulative transmission coefficient along the depth direction, i.e. $\boldsymbol{T}(\boldsymbol{r}) = \int_{\boldsymbol{d_i}}^{\boldsymbol{r}} (1 - \boldsymbol{R}(\boldsymbol{x}))^2 \, d\boldsymbol{x}$.

Different from UTT, handheld probes have limited-view detection angles. Therefore, the possibility of a structure being successfully reconstructed in an image is not 100 percent any more. Instead, the possibility is decided by the coverage angle of detection at that location and the orientation of the structure. In order to simulate such limited-view effect, we introduce a weighting matrix $\boldsymbol{\Omega_i}$ to simulate the limited coverage angle of detection for each imaging event and $\boldsymbol{W}$ to simulate the effect of structure orientation.

According to the working scheme of ultrasound modality in OPUS system (shown in Figure 8.7), each imaging event uses different transducer elements for detection, therefore generating different coverage angle for the same point in the space. Even in the same imaging event, the coverage angle of detection is different at different spatial location, which is shown in Figure 8.5(a). It can be seen that the coverage angle is a function of spatial locations. In order to take such effect into consideration, we assume that the possibility of a structure in location $\boldsymbol{r}'$ to be fully recovered is 1, if the detection angle is 360 degree. Therefore, in the cases of limited-view detection, the probability of a structure to be detected is proportional to the coverage angle of that spatial point. For example, the detection elements from $\boldsymbol{d_i}$ to

$\boldsymbol{d}_{i+\frac{N}{2}-1}$ forms two different coverage angles α_1 and α_2 to the two points $\boldsymbol{r_1}$ and $\boldsymbol{r_2}$ in Figure 8.5(a), which leads to two different weighting factors, i.e. $\Omega_i(\boldsymbol{r_1}) = \frac{\alpha_1}{360}$ and $\Omega_i(\boldsymbol{r_2}) = \frac{\alpha_2}{360}$. This weighting matrix is created one event by one event. For the effect introduced by the orientation of the structure, the maximum detection angle (i.e. the angle covered by all transducer elements) is considered. When the normal direction of the structure in $\boldsymbol{r}$ falls into the maximum detection angle, $W(\boldsymbol{r}) = 1$, otherwise, $W(\boldsymbol{r}) = 0$, as Figure 8.5(b) shows.

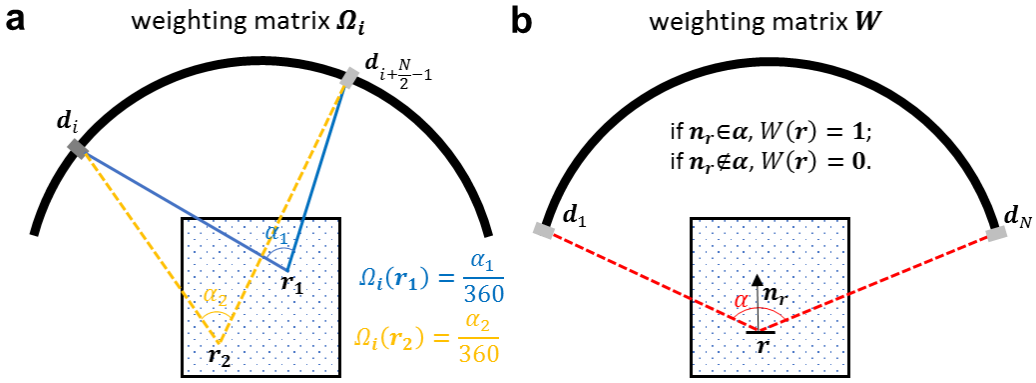

Figure 8.5. multispectral OA data-driven clustering to segment and identify different tissue types. (a) An OA image of the arm at 800 nm; (b) initial segmentation result of (a) with data-driven clustering method; (c) final segmentation results adapted from (b).

Following Equation 8.8, a simulated ultrasound image can be formed for each pulsing event and 256 simulated images are formed at the end. Then Equation 6.7 is used to generate one final simulated ultrasound image $\boldsymbol{I}_{sim}$.

The SoS distribution in the imaged region can be calculated using the least square optimization as:

$$\boldsymbol{c} = arg\min_{\boldsymbol{c}}(\|\boldsymbol{I}_{us} - \boldsymbol{I}_{sim}\|_2^2), \qquad (8.9)$$

where $\boldsymbol{I}_{us}$ is a quantitative ultrasound image without any image postprocessing and reconstructed with the method introduced in Chapter 6. A quantitative ultrasound image is crucial to guarantee that Equation 8.9 can generate meaningful SoS distribution, therefore, if only a contrast-enhanced ultrasound image available, which is common in clinical ultrasound imaging, the post-processing should be undone before going for the optimization problem as Figure 8.2 shown. The optimization problem in Equation 8.9 is nonlinear and the optimal SoS distribution can be found with the nonlinear programming solver 'fminunc' in Matlab. In order to stabilize the solution and avoid the fluctuation introduced by noise, a penalty term is introduced to Equation 8.9 as:

$$\boldsymbol{c} = arg\min_{\boldsymbol{c}}(\|\boldsymbol{I}_{us} - \boldsymbol{I}_{sim}(\boldsymbol{c})\|_2^2 + \lambda\|\boldsymbol{L}\boldsymbol{c}\|_2^2), \qquad (8.10)$$

where λ is the regularization parameter and $\boldsymbol{L}$ is the regularization matrix and designed to be a high-pass filter to enforce smoothness in this case. $\boldsymbol{L}$ is a standard Laplacian operator (the same as the one used in Chapter 7).

8.2.3 Initial SoS guess – multispectral optoacoustic data-driven clustering

The multispectral optoacoustic data-driven clustering method introduced in this subsection is developed by Jan Kukačka.

Since nonlinear optimization converges to local minimum, a good initial guess is important for final solutions. In order to have a good initial guess about the SoS distribution in the imaged tissue sample, a reasonable way is to segment an ultrasound image into different tissue types and then assign corresponding SoS value from literature to each tissue type. However, even though the traditional image intensity-based segmentation methods might be able to segment an image into different tissue types, they cannot identify specifically the tissue type of each segmented region. In this case, multispectral optoacoustic imaging appears as a very promising solution, since it has multi-wavelength illumination and can recover the absorption spectrum of optical absorbers in the imaged sample. As each tissue type contains a characteristic optical absorber and can be distinguished from each other with their absorption spectra, optoacoustic spectra-based clustering can perform not only image segmentation but also identify the tissue type. Therefore, we develop a segmentation method which clusters the pixels in multispectral optoacoustic images into $L = 5$ classes i.e. blood, fat, water, skin and other based on the optoacoustic spectra of each pixel. Since the spectral coloring corrupts the optoacoustic spectra along with imaging depth, we use a data-driven principal component analysis (PCA)-based method to get rid of effect from spectral coloring on the clustering accuracy as follows:

- Prepare a training set T which includes M multispectral optoacoustic image stacks and each image stack is of width w, height h, and number of wavelengths k , i.e. $T = \{I_i \in \mathbb{R}^{w\times h\times k} | i \in [1, \dots, M]\}$;
- Create a matrix P of all pixels in T, $P \in \mathbb{R}^{M\times w\times h\times k}$;
- Extract the first $D = 4$ principal components of P with PCA to form a matrix $A \in \mathbb{R}^{k\times 4}$;
- Project P on A, i.e. $P_{PCA} = PA$;
- Manually assign one of the following labels: blood, fat, water, skin, and other to every pixel in matrix P_{PCA};
- Compute the mean and variance over all pixels assigned to the same label (except for 'other').

After the above training procedure is finished, a multispectral optoacoustic image stack is segmented to different tissue types using the probabilistic graphical mixture model in Figure 8.6. We assume that the observed spectrum $\boldsymbol{x}_n$ in each of the N pixels depends on the tissue type $\boldsymbol{z}_n$ that the pixel belongs to. Furthermore, to capture the large variability of spectra caused by light fluence variability in the tissue, we model each tissue component as a mixture of $K = 3$ diagonal Gaussians and assume the pixel n was generated from the mode $\boldsymbol{s}_{n,l}$. Our model is thus a mixture of Gaussian mixtures, with the joint probability distribution factorized as:

$$p(\boldsymbol{x}, \boldsymbol{z}, \boldsymbol{\theta}, \boldsymbol{\pi}, \boldsymbol{s}, \boldsymbol{\rho} | \boldsymbol{\alpha}, \boldsymbol{\beta}, \boldsymbol{\eta}) = p(\boldsymbol{x}|\boldsymbol{z}, \boldsymbol{s}, \boldsymbol{\theta}) p(\boldsymbol{z}|\boldsymbol{\pi}) p(\boldsymbol{\pi}|\boldsymbol{\alpha}) p(\boldsymbol{\theta}|\boldsymbol{\eta}) p(\boldsymbol{s}|\boldsymbol{\rho}) p(\boldsymbol{\rho}|\boldsymbol{\beta}), \quad (8.10)$$

where $\boldsymbol{\theta}$ represents parameters of the individual Gaussian components, $\boldsymbol{\pi}$ are the mixing coefficients of the tissue types, $\boldsymbol{\rho}$ are the mixing coefficients of the mixtures representing the individual components, and $\boldsymbol{\alpha}$, $\boldsymbol{\beta}$, and $\boldsymbol{\eta}$ are hyperparameters whose values are set based on

the training procedure described above to represent the distribution of tissue types and the mean and variance of each component in each dimension. Specifically, $p(\boldsymbol{x_n}|\boldsymbol{z_n}, \boldsymbol{s_n}, \boldsymbol{\theta}) = \prod_l^L \left[\prod_k^K [\prod_d^D \mathcal{N}(x_{n,d}|\theta_{k,l,d})]^{s_{n,k,l}}\right]^{z_{n,l}}$, where z_n and $s_{n,l}$ are random variables from categorical distributions, i.e. $\boldsymbol{z}_n \sim \text{Cat}(\boldsymbol{\pi})$, $\boldsymbol{s}_{n,l} \sim \text{Cat}(\boldsymbol{\rho}_l)$, $\boldsymbol{\pi}$ and $\boldsymbol{\rho}_l$ are random variables from Dirichlet distributions, i.e. $\boldsymbol{\pi} \sim \text{Dir}(\boldsymbol{\alpha})$, $\boldsymbol{\rho}_l \sim \text{Dir}(\boldsymbol{\beta}_l)$, and $\theta_{k,l,d}$ is distributed as Normal-Inverse Gamma distribution, i.e. $\boldsymbol{\theta}_{k,l,d} \sim \text{Normal} - \text{Inverse Gamma}\ (\boldsymbol{\eta}_{k,l,d})$.

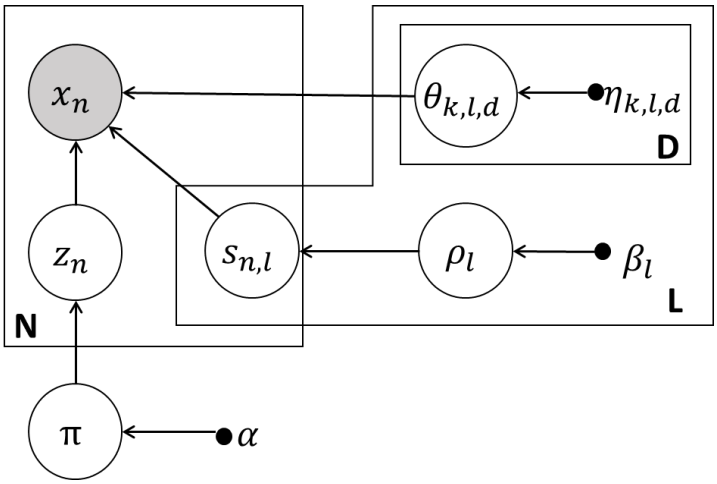

Figure 8.6. Schematic of the multispectral optoacoustic data-driven clustering method. N is the number of pixels in the image, L is the number of tissue types, K is the number of subcomponents for each tissue type, and D is the dimensionality of each pixel.

In this study, L is the number of tissue types ($L = 5$), K is the number of subcomponents for each tissue type ($K = 3$), and D is the dimensionality of each pixel ($D = 4$). To cluster the image, we need to evaluate the probability $p(\mathbf{z}|\boldsymbol{x}, \boldsymbol{\alpha}, \boldsymbol{\beta}, \boldsymbol{\eta})$. This quantity is not tractable, but since the model uses conjugate priors, we can use variational inference procedure to approximate it by a variational distribution $q(\boldsymbol{z})$ and use Monte Carlo sampling to get the distribution of tissue class membership for each pixel, using its mode as hard clustering [191].

8.2.4 Bent-ray propagation -- Fast Marching Method (FMM)

According to Snell's law, the acoustic rays bend when sound waves propagate from one medium to another with different sound speed. In other words, heterogeneous SoS distribution is always accompanied with refraction on the interfaces during wave propagation. For example, the propagation of ultrasound waves from muscle which is of SoS about 1570 m/s to subcutaneous fat which is of SoS 1450 m/s causes a refractive effect that significantly distorts the ultrasound ray direction and eventually causes spatial distortion and intensity artifacts in the resulting images if straight ray propagation model is used. Therefore, accompanied with the spatial-variant SoS distribution, bent ray propagation is necessary to achieve high-accuracy reconstruction.

With the satisfaction to high-frequency assumption, the propagation of a sound wave can be expressed with Eikonal equation as [192]:

$$|\nabla T(\boldsymbol{r})|^2 = \frac{1}{c^2}, \qquad (8.11)$$

where T is the arrival time of a wave front Γ at a spatial location $\boldsymbol{r}$, and the arrival time T of the initial position of the wave front is set to 0, i.e. $T(\Gamma_0) = 0$.

The solution of Equation 8.11 tracks the motion of a monotonically advancing wave front from sound source to detectors. Among all methods for solving Eikonal equation, the fast marching method (FMM) is computationally fast due to the fact that it combines entropy-satisfying upwind schemes and a fast sorting technique to find the solution in one-pass algorithm [193, 194]. In order to reduce the computational complexity and increase the accuracy along diagonal directions of traditional FMM, we used a more advanced FMM named multi-stencils fast marching method (MSFMM) developed by M. Hassouna [193]. With this method, the traveling time of a wave front from the source to each point in space can be calculated.

Considering the case of Acuity256, the image region is normally a $4 \times 4\ cm^2$ and centered in the focus region of transducer array. In order to calculate the ToF in the image region, the SoS from each grid point in that area to every transducer element need to be known. Since the SoS distribution output from model-based SoS reconstruction only covers the image region, we expand the $4 \times 4\ cm^2$-SoS distribution to the whole field which covers transducer array and image region ($12 \times 8\ cm^2$) under the assumption that the space above the skin layer is the coupling medium (heavy water) and the area beneath the interface and outside the defined image region is of a constant SoS 1530 m/s. With the SoS distribution expanded to cover the whole field, MSFMM can be applied to calculate the ToF from each transducer element to every grid based on Equation 8.11.

For each transducer element, one ToF map is calculated, which results in N different ToF maps in total (N equals to the number of transducer elements in the array, N=256 for Acuity256). After the ToF maps from all transducer elements to the grids in image region being calculated, the reconstruction of ultrasound images can be done following the steps introduced in Chapter 6.

If the iteration number is no larger than the optimal setting, the ToFs are only applied to do ultrasound image reconstruction to update the $\boldsymbol{I}_{us}$ in Equation 8.10 for next round of iteration. Using the residual between the simulated ultrasound image and the experimental ultrasound image as the criterion, the non-linear optimization framework shown in Figure 8.2 is run with a few iterations (e.g. 10 iterations).

The whole framework of ultrasound-image-driven high-quality reconstruction (shown in Figure 8.1) introduced in this chapter can be decomposed into a three-phase algorithm. In phase 1, the segmentation of tissues based multispectral optoacoustic images and the preparation of a quantitative ultrasound image are done; in phase 2, the spatial-variant SoS distribution is iteratively reconstructed based on a nonlinear optimization engine; and in phase 3, we use this optimal SoS distribution to guide the bent ray propagation for the reconstruction of optoacoustic and ultrasound images. Note that the image reconstruction is straightforward once accurate ToF maps are available to guide the back-projection of the data into the image region. The algorithm proceeds as follows:

Table 8.1 Ultrasound-image-driven high-quality reconstruction algorithm

load a multispectral OA image stack and the corresponding co-registered US image;

Phase1: initialization of the first iteration

- *segment the OA image with data-driven clustering;*
- *assign SoS value from literature to each tissue type;*
- *prepare the US image to be a quantitative raw image;*

Phase2: iterative SoS reconstruction

- if $i \leq optimal\ N\_iteration$, loop
  - *apply the nonlinear optimization (Equation8.10) to derive the SoS distribution in imaged region;*
  - *extend the SoS from image region to the whole field;*
  - *calculate the ToF from each grid to each transducer element with MSFMM;*
  - *back project the US signals according to the ToFs to form a new US image;*
  - *update the input US image in the nonlinear optimization;*
  - *update the initial guess of SoS distribution in the nonlinear optimization;*

Phase3: reconstruction with optimal SoS distribution

- if $i > optimal\ N\_iteration$,
  - *back project the US signals according to the ToF of each transducer element;*
  - *back project the OA signals according to the ToF of each transducer element.*

8.2.5 Experimental settings

To validate the simulation framework, we performed experiments with an agar phantom which includes a polyester tube of inner diameter 3mm. The focus of our validation is the intensity of major structures (i.e. surface of the phantom, upper and lower wall of the tube) in the simulated and experimental ultrasound images.

In order to demonstrate the improvement introduced by the spatial-variant SoS and bent-ray propagation model, the reconstruction results using conventional single SoS, dual-SoS model (introduced in Chapter 5) are presented and compared. This part of demonstration has been enabled using numerical phantom and an experimental measurement from a volunteer. Procedures on human subjects were performed after obtaining their written informed consent.

The healthy volunteer was imaged over the upper arm after obtaining the written informed consent. The scanning system was a hybrid handheld OPUS system (Acuity 256; iThera Medical GmbH, Munich, Germany) introduced in Chapter 4. Figure 8.7(a) shows the imaging probe of the system. When it works in optoacoustic mode, the laser beam is triggered to

illuminate the sample and collect optoacoustic signals as Figure 8.7(b) shows. After reconstruction, an optoacoustic image is formed (Figure 8.7(c)). For optoacoustic imaging, the sample is scanned from wavelength 700 nm to 970 nm with 10 nm interval. In this study, the ultrasound mode is following the work scheme shows in Figure 8.7(d). After the ultrasound pulse being generated, reflected and acquired (Figure 8.7(e)), an ultrasound image is formed (Figure 8.7(f)) which is co-registered with the optoacoustic image in panel 8.7(c).

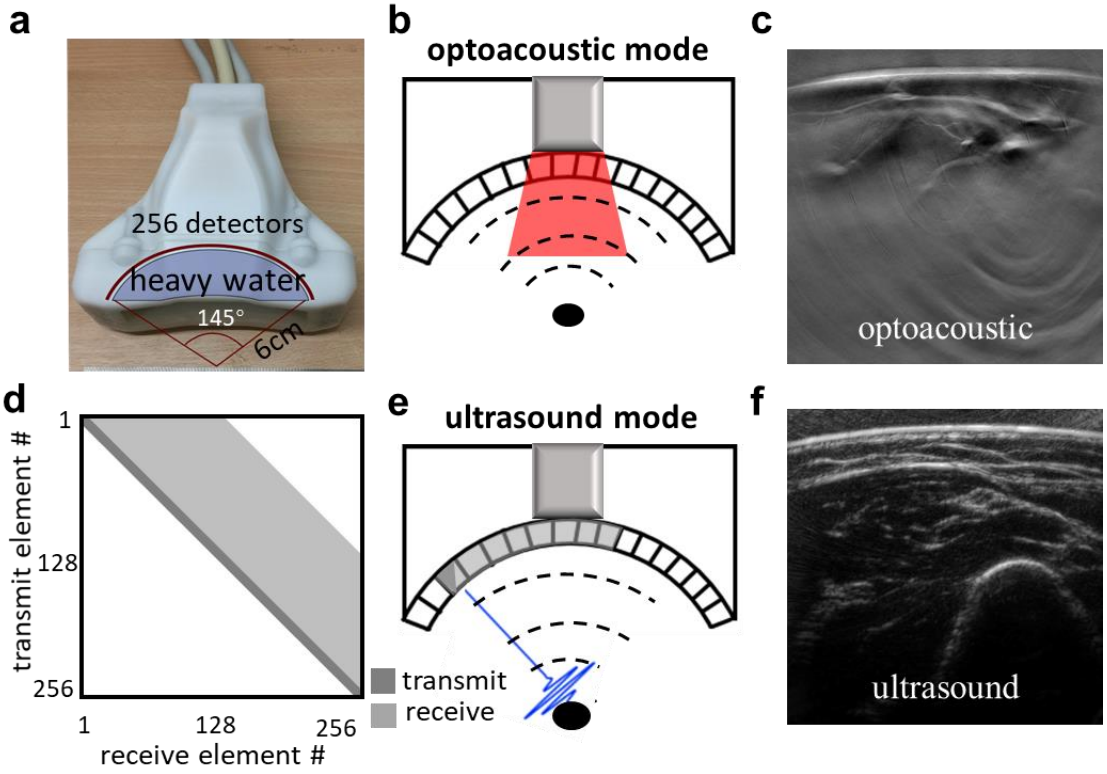

Figure 8.7. Experimental hybrid OPUS system. (a) The imaging probe; (b) optoacoustic mode; (c) an example of optoacoustic image from OPUS system; (d) working scheme of ultrasound modality; (e) ultrasound mode; (f) an example of ultrasound image from OPUS system.

8.3 Results

In this section, the validation of the ultrasound simulation using an agar phantom is presented. Then the reconstruction results using single SoS, dual-SoS and spatial-variant SoS model are compared based on a numerical phantom mimicking the tissue and an experimental dataset from forearm.

8.3.1 Ultrasound image model validation

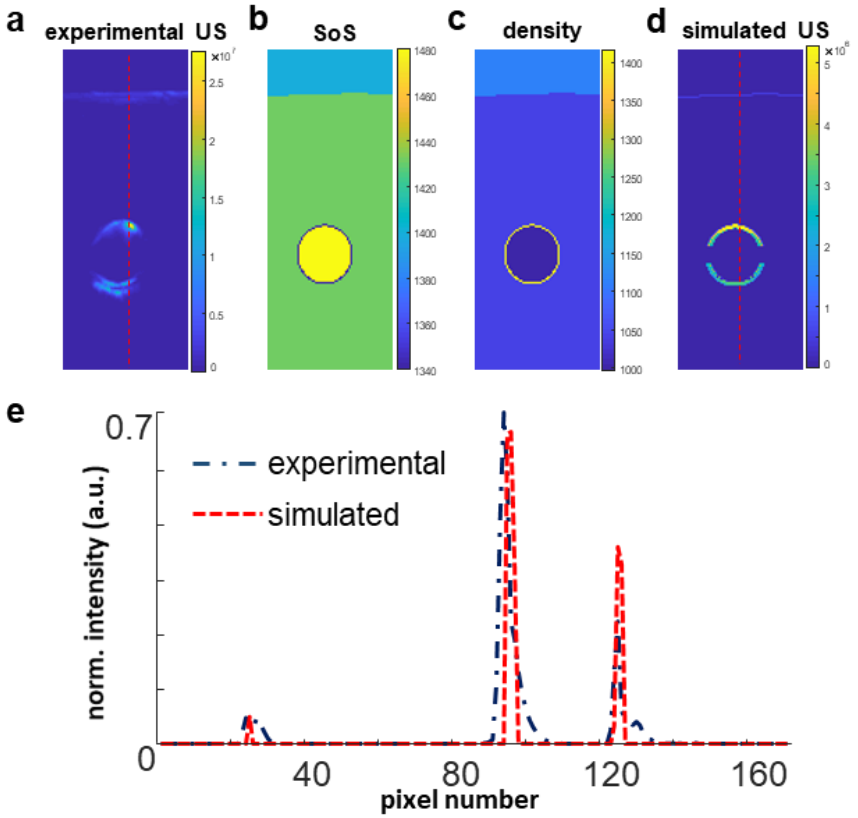

Figure 8.8. Spatial-variant SoS and ToF calculation from image region to the whole field. (a) SoS output from nonlinear optimization in the image region; (b) expand the SoS in image region to whole field; (c) ToF of element #256 in whole field; (d) ToF of element #256 in image region.

In order to validate the proposed ultrasound image simulation framework, an agar phantom with a tube insertion was imaged. Figure 8.8(a) presents the experimental ultrasound image which shows the surface of the phantom, the upper and lower walls of the tube. Due to the limited-view detection geometry, the boundary of the tube on the left and right is not visible in this image. Figure 8.8(b) is the initial SoS guess, i.e. the input of the simulation framework presented in Figure 8.4. The SoSs for the four different layers are 1397 m/s, 1430 m/s, 1340 m/s, and 1480 m/s (corresponding to the SoS of heavy water, fat, polymer and water reported in [190, 195]). Because this phantom is made with artificial materials, whose density and SoS does not follow the linear regression shown in Equation 8.1, we assigned the corresponding density of the above mentioned four material reported in literature as 1110 g/cm^3, 1040 g/cm^3, 1416 g/cm^3, and 997g/cm^3 [190, 195]. Figure 8.8(d) shows the simulated ultrasound image using the framework presented in Figure 8.4. It can be seen that the three interfaces and the limited-view effect are successfully simulated. In order to check whether the simulation framework is capable to simulate the reflection and attenuation properly, the line profile of these three interfaces are plotted in Figure 8.8(e). The normalized intensity of those three interfaces from experimental and simulated ultrasound images are compared. From panel 8.8(d), we can see that the location and relative intensity of the three interfaces in simulated ultrasound image are similar to the ones in experimental images,

which indicts that out ultrasound image simulation scheme considered the reflection, attenuation and limited-view detection properly and is capable to generate close-to-reality ultrasound images.

8.3.2 Reconstructed SoS in tissue

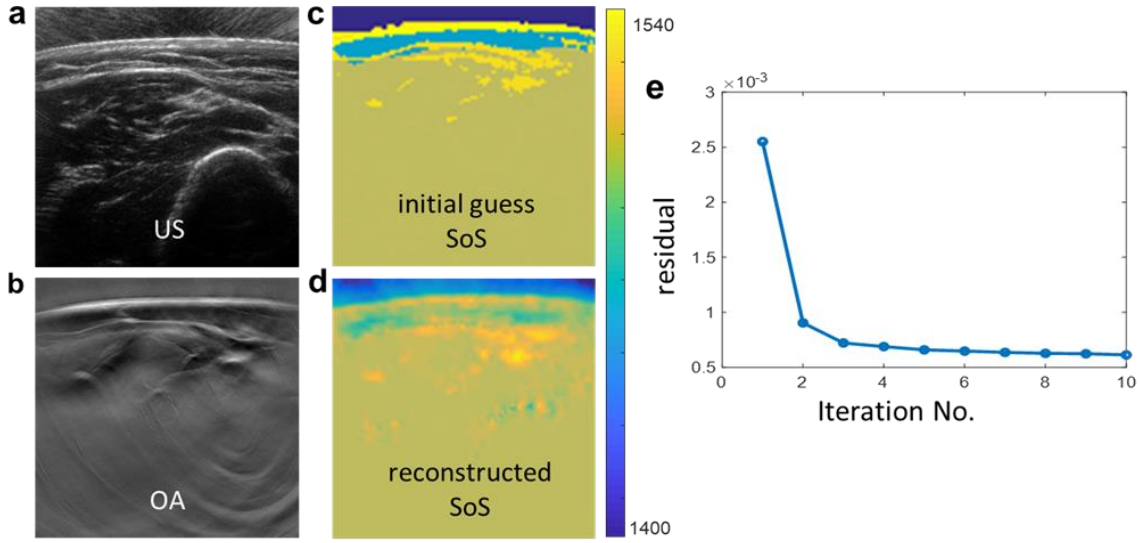

Figure 8.9. Convergence of the framework shown in Figure 8.2.

After the fidelity of the simulation scheme being demonstrated, we applied it to derive the spatial-variant SoS in the tissue measurement based on the iterative ultrasound-image-driven SoS reconstruction scheme shown in Figure 8.2. Figure 8.9(a) shows the ultrasound image of the upper forearm region, which includes multiple tissue layers such as skin, fat, muscle and bone. Figure 8.9(b) is the corresponding optoacoustic image at 750 nm. For one scan, 28 multispectral optoacoustic images are acquired. Then using the data-driven clustering method, the image is segmented into five classes, i.e. coupling medium (heavy water), skin, fat, blood and background (muscle). We assign the corresponding SoS to different tissue types to form the initial guess of the SoS as panel 8.9(c) shows. After ten iterations, the reconstructed SoS image is output and presented in Figure 8.9(d). In order to study the convergency of the algorithm, the norm of the residual between simulated ultrasound image and experimental image are plotted along with the iteration number in Figure 8.9(e). It can be seen that the algorithm converges fast from the first iteration to the second iteration. Then the converge speed decreases time by time. In order to have a balance about computational speed and result accuracy, 5 iteration is set as criteria in Figure 8.2, i.e. when the iteration is larger than 5, the iterative reconstruction of SoS distribution in Figure 8.2 stops and the derived SoS is output as the optimal SoS distribution for final optoacoustic and ultrasound image reconstruction.

8.3.3 Image reconstruction results with spatial-variant SoS

Using the criteria derived from last section, we use the derived spatial-variant SoS for image reconstruction. In order to demonstrate the improvement of image quality, the reconstruction results using spatial-variant SoS are showed and compared with the

reconstruction results using single SoS and dual-SoS models based on both simulations and experimental datasets.

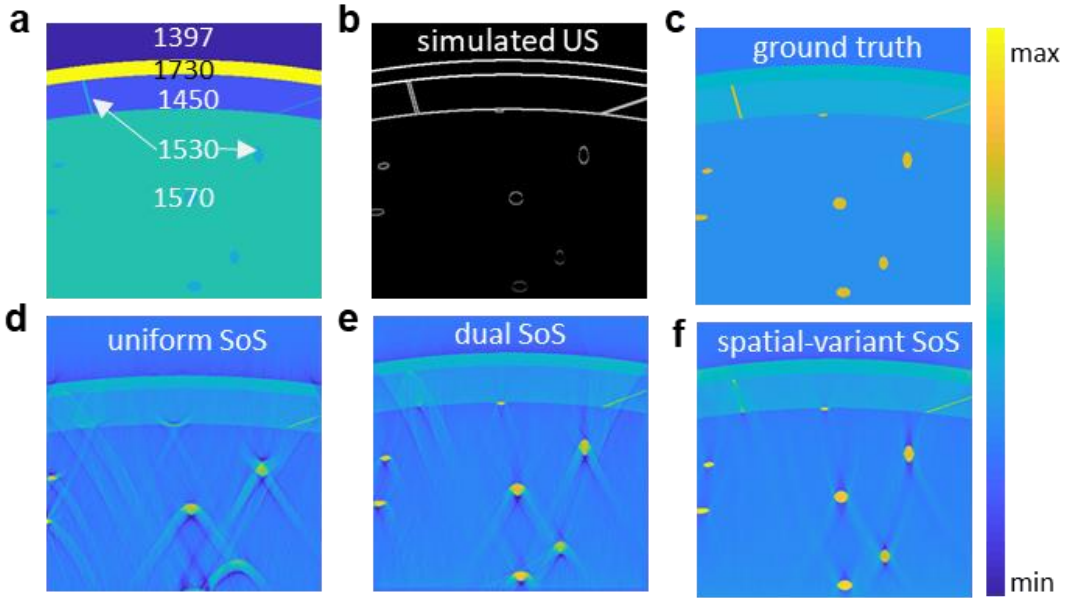

Figure 8.10. Reconstruction of phantom/simulations with dual-SoS and spatial-variant SoS model. (a) SoS distribution; (b) simulated US image; (c) ground truth of simulated optoacoustic image; (d) reconstruction with uniform-SoS; (e) reconstruction with spatial-variant-SoS.

Figure 8.10 shows the reconstruction results of the numerical simulation. Figure 8.10(a) is the SoS image of the numerical phantom, which forms a simulated ultrasound image as panel 8.10(b) shown. The simulated optoacoustic image (i.e. the ground truth of optoacoustic reconstruction) is presented in Figure 8.10(c) in which the skin, fat, muscle and blood vessels are simulated. Figure 8.10(d), 8.10(e) and 8.10(f) are the reconstructed optoacoustic images using single-SoS, dual-SoS and spatial-variant-SoS models, respectively. From panel 8.10(d), it can be seen that with single-SoS model, the superficial layers such as skin and fat layer are reconstructed successfully. But the blood vessels are deformed strongly, i.e. the deeper the blood vessel is, the stronger the deformation is. When dual-SoS model is used and the SoS mismatch between heavy water and tissue is considered, the deformation of blood vessels is largely reduced (as Figure 8.10(e) shown). However, when the imaging depth increases, strong deformation is still observed from panel 8.10(e). When the spatial-variant SoS close to reality is used, the blood vessels can be well reconstructed regardless of the depth as demonstrated in Figure 8.10(f). Although clear artifacts due to limited-view detection is still visible, the spatial-variant SoS model contributes to the best image quality among three reconstructions.

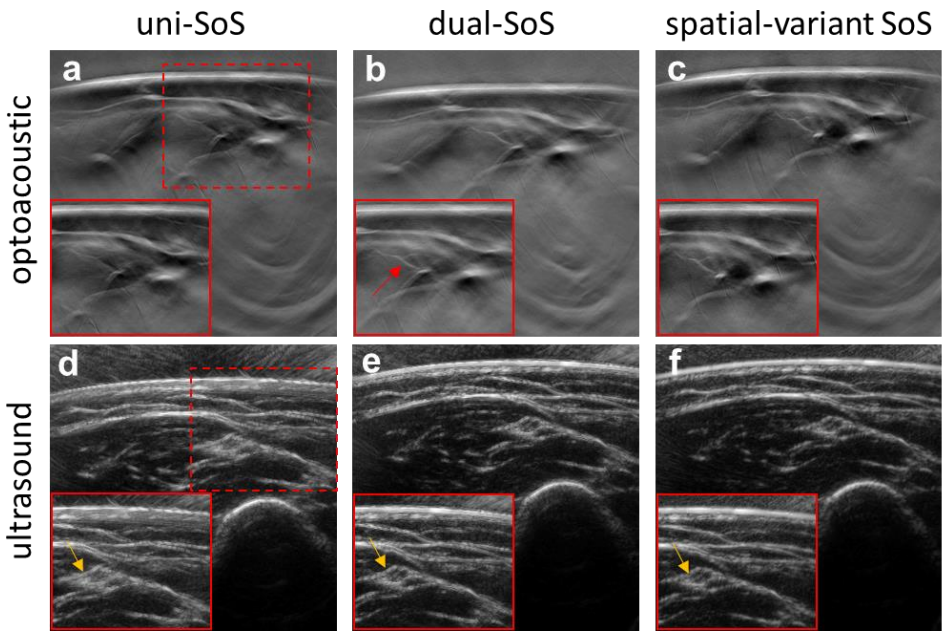

Figure 8.11. Reconstruction of an arm dataset with spatial-variant SoS and dual-SoS model. (a - b) Reconstructed US image with (a) dual-SoS model and (b) spatial-variant SoS model; (c) difference between (a) and (b); (d - e) Reconstructed OA image at 800 nm with (d) dual-SoS model and (e) spatial-variant SoS model; (f) difference between (d) and (e).

In addition to the numerical phantom, we also used the spatial-variant SoS model to reconstruct experimental tissue data and compared with the other two methods. Figure 8.11 shows the optoacoustic and ultrasound reconstruction results of the forearm. Figure 8.11 (a)-(c) are the reconstructed optoacoustic images using single-SoS, dual-SoS and spatial-variant SoS, respectively. Consistent with the numerical phantom's results, the blood vessels beneath the fat layer (in the zoomed-in views) are suffering strong deformation in uniform SoS reconstruction. With dual-SoS model, the deformation of the blood vessels is reduced and contribute to much sharper image and even unfold a new structure which was not visible in panel 8.11(a) (marked with red arrow). But still beside the vessels, there exist smearing artifacts. With spatial-variant SoS model, the blood vessels are better converged and much sharper than in the other two images. In addition, the smearing artifacts is eliminated.

The spatial-variant SoS reconstruction is helpful not only for optoacoustic images, but also for ultrasound images. Figure 8.11(d) – 8.11(f) are the reconstructed ultrasound images of the forearm using single-SoS, dual-SoS and spatial-variant SoS, respectively. In the zoomed-in view, there exist multiple structures e.g. the nerves marked with yellow arrows. It can be seen that from uniform SoS to spatial-variant SoS, the boundary of the nerves is sharper and shaper. The same phenomenon is observed with other structures. Among the three images, spatial-variant SoS reconstruction contributes to the best contrast and sharpness.

8.4 Discussion and conclusion

This chapter presents a pilot study i.e. an ultrasound-image-driven high-quality reconstruction framework, which is mainly based on an iterative model-based SoS reconstruction algorithm and a new multispectral optoacoustic-data driven clustering method. Moreover, in this reconstruction framework, bent ray propagation model is used to

consider the acoustic refraction on the interfaces of different tissues. Thanks to the spatial-variant SoS distribution and bent ray propagation model, the reconstructed images are of higher accuracy and better image quality for both optoacoustic and ultrasound images.

The proposed ultrasound-image-driven high-quality reconstruction framework is of several advantages over conventional approaches. First, it enables to derive high-resolution SoS distribution from reflection mode ultrasound imaging and make it possible to derive the SoS distribution inside imaged sample without the UTT measurements. The derived SoS distribution contributes to a more accurate reconstruction compared with the one assuming a constant SoS for both optoacoustic and ultrasound modalities. Second, our proposed framework takes into account ray refraction by solving the Eikonal equation, minimizing the reconstruction artifacts due to straight ray assumption. The use of bent-ray propagation model is more accurate than straight rays. This contributes to superior image quality compared with using straight rays as being demonstrated in simulation results in Figure 8.9 and experimental results in the forearm dataset (Figure 8.10).

The reconstruction of SoS distribution inside the tissue requires a quantitative ultrasound image whose intensity can be modeled by the acoustic reflectivity and attenuation. For commercial ultrasound systems, the generated ultrasound images have been applied signal processing e.g. time-gain amplification and post-processing, which makes the intensity values of an ultrasound image lose the quantitative meaning and can only be used for morphological interpretation. However, with the customized OPUS system introduced in Chapter 4 and the corresponding reconstruction method introduced in Chapter 6, the ultrasound images are quantitative and the intensity values can be fairly modeled by the acoustic reflectivity, attenuation and limited-view detection. In the cases where raw ultrasound images are not available, we need to either undo all processing or same processing procedures need to be simulated into the simulation model.

For the ToF calculation using MSFMM in this study, we set the distance between two grids the same as the image resolution of the ultrasound, but this is not necessary. If readers want to speed up the computation, coarser grid spacing is applicable. For example, the grid spacing in MSFMM can be 400 μm, i.e. 4 times coarser than image resolution in our case, and bicubic interpolation to obtain the ToF values at off grid points can generate similar results.

As a proof-of-concept study, our approach has some limitations. First, the imaging model employed simulate 2D imaging plane, while the 3D acoustic propagation occurs experimentally. Second, the same as most nonlinear optimization algorithms, our approach depends on the initial guess of SoS. A fair initial guess can lead to realistic estimation of the spatial-variant SoS distribution, meanwhile, a bad initial guess can trap the solution to the local minimum and diverse from the optimal solution. Third, the method involves some computational cost especially when the number of pixels is large. At the same time, in order to find an optimal solution, multiple outer iterations are necessary. Further optimization of the stopping criteria could help reduce the computational cost.

Most optoacoustic studies and reconstruction algorithms are based on the assumption of tissue homogeneity which justifies the use of a single SoS value and straight ray propagation for the region of interest. We have demonstrated numerically and experimentally that such an assumption in the presence of SoS heterogeneities leads to inaccurate reconstruction of

both optoacoustic and ultrasound images. We have also demonstrated that the ultrasound-image-driven SoS reconstruction can derive high resolution SoS and contribute to better optoacoustic and ultrasound image quality. The iterative reconstruction algorithm for retrieving SoS images, using the Eikonal equation to model refractive effects in the forward projection, yields accurate SoS images in the OPUS imaging. This approach shows the potential in obtaining high quality optoacoustic images. In addition to improving image quality in optoacoustics, knowledge of the spatial distribution of SoS can also potentially improve diagnostic value of clinical optoacoustic imaging.

9. Conclusion and outlook

In order to further improve the value of MSOT imaging, especially in clinical studies, three parts of work were done and presented in this dissertation. In the first part, as the preparation, the imaging chain of preclinical MSOT imaging was studied and a synthetic data framework was developed for better experimental designs. Based on the understanding gained from this study, the rest of dissertation extended the scope to clinical MSOT imaging, especially clinical hybrid MSOT and ultrasound imaging. In the second part, the image reconstruction of single-mode MSOT and ultrasound was developed and optimized separately. In the third part, the issue that how to optimize the value of such hybrid information was addressed. The ultrasound images were used as priors for optoacoustic image reconstruction, which was demonstrated to improve optoacoustic image quality, therefore, hopefully increase the clinical value of MSOT imaging.

In Chapter 2, readers were familiarized with the technical background of optoacoustic image reconstruction, including the wave equation, back-projection algorithm, and model-based reconstruction scheme. Besides, an analysis technique namely spectral unmixing was introduced, since it can largely increase the sensitivity of optoacoustic imaging and empower MSOT imaging.

In Chapter 3, the imaging chain of preclinical MSOT imaging, i.e. the formation of optoacoustic signal from an optical absorber to an electrical signal, was studied. Based on that, the optoacoustic signal from an absorber was successfully simulated, which enabled the development of the SDF. The SDF was demonstrated to generate realistic synthetic MSOT images which mimicked the experimental MSOT images in small animal studies with the application of extrinsic contrast agents. The simulated synthetic images are of comparable image intensity and molecular sensitivity to the experimental MSOT images, which validates the fidelity of the SDF simulator. The development of the SDF enables the molecular sensitivity studies of varied contrast agents without extensive animal studies. Moreover, the optoacoustic signal simulator in the SDF allows the analysis of the influence of each variable in the imaging chain on the optoacoustic image quality, such as the EIR, SIR and reconstruction algorithm and so on, which played an important role in the following research of improving clinical optoacoustic image quality.

In Chapter 4, the essential changes in hardware design (i.e. limited-view illumination and detection) for the portability of clinical MSOT and the corresponding challenges were introduced. Besides, the working protocol of a handheld hybrid MSOT and ultrasound system (i.e. OPUS) was indicted in detail to prepare the reader for the following two chapters, which are the reconstruction of optoacoustic and ultrasound reconstruction in OPUS imaging, respectively.

In Chapter 5, a dual-SoS optoacoustic reconstruction model was developed to take into account the SoS mismatch between coupling media (e.g. heavy water) and imaged sample (e.g. tissue). In clinical studies, some optical absorbers whose spectral signature is after 900 nm

(e.g. lipid) are of special clinical values for disease diagnosis. In order to enable the corresponding studies, some special coupling media such as heavy water is used to replace water or ultrasound gel as coupling medium used in preclinical studies to avoid the strong light absorption from water. But this introduces the SoS mismatch issues which fails the standard reconstruction algorithm with uniform SoS assumption. Therefore, a dual-SoS model was developed to optimize the optoacoustic image quality for standalone clinical MSOT imaging. With phantom and tissue data, the dual-SoS model was demonstrated to contribute to better optoacoustic image quality by largely reducing the spectral smearing artifacts and recovering the structures with more accurate shape.

In Chapter 6, three different signal processing methods, ultrasound image reconstruction, and three image Z-projection strategies were developed for the customized OPUS system. Moreover, in order to optimize the efficiency of imaging in both time and computational cost, some variations of defaulted synthetic aperture and their corresponding reconstruction results and efficiency improvements were studied and analyzed. According to the phantom and tissue datasets, spiking deconvolution and “AIP + MIP” contribute to the best ultrasound image quality

In Chapter 7, a new method to incorporate ultrasound information into optoacoustic reconstruction to reduce the limited-view artifacts and improve contrast of clinical optoacoustic images was developed. After the work presented in last two chapters being done, well co-registered optoacoustic and ultrasound images are accessible from each scan performed with hybrid OPUS systems. The structural information from ultrasound images was utilized to guide regional Laplacian regularization-based reconstruction of optoacoustic images. Using phantoms and data from OPUS scans of human radial and carotid arteries, it shows that ultrasound-driven optoacoustic inversion reduces limited-view artifacts and improves image contrast. The approach is shown to detect deep-seated blood vessels and to offer unique insights into atherosclerotic carotid plaques in humans, potentially paving the way for new abilities in vascular imaging and more generally in optoacoustic imaging.

In Chapter 8, another new method to incorporate ultrasound information and optoacoustic information available in hybrid OPUS system was developed. Comparing to the work in last chapter, instead of the structural information, the functional parameters in ultrasound images i.e. the SoS distribution was derived using an iterative nonlinear model-based method with the help of the spectral information offered by optoacoustic images. Based on the derived spatial-variant SoS distribution, FMM was used to consider the diffraction happening on the interfaces of different layers of different acoustic properties. The reconstruction results with this new model were compared to the results of single-SoS and dual-SoS model to demonstrate the improvement in accuracy.

Outlook

However, the development of clinical MSOT imaging is still far from ideal, given the numerous medical needs [196]. For example, for precise assessment of the plaque vulnerability, deeper penetration with higher signal-to-noise ratio signals is needed [196], especially for the deeper-seated internal carotid arteries which are more likely to cause strokes by carotid stenosis or thrombosis [196-198]. Thus, fundamental improvement in sensitivity of the ultrasound transducers and further improvement in image quality enabled by better signal

preprocessing or by incorporation of ultrasonographic priors to optoacoustic reconstruction will empower macroscopic optoacoustic imaging with deeper penetration and better image/spectral quality than the current state of the art.

Further improvement of the detection sensitivity and the concomitant increase in penetration depth of optoacoustic imaging devices can provide a long-awaited tool for addressing clinical needs for on-site real-time assessment of disease state or treatment efficacy especially in early stages [196]. Such an ultra-sensitive/deep optoacoustic imaging technique would enable novel theranostic approaches with earlier detection, diagnosis and treatment monitoring, also facilitating for example patient stratification in the era of personalized precision medicine [199]. Towards deeper penetration than just the dermis [200, 201], a more sensitive detection of the dimmed optoacoustic signal induced by low light fluence in deep tissue is of key importance [202-204]. However, simply tuning up laser energy is not an option as higher light fluence may damage the tissue. Therefore, the alternative would be to use ultrasound transducers of higher sensitivity. Given the radiation safety limit, the higher the detection sensitivity of the employed transducer/sensor the deeper the penetration capability of the optoacoustic device.

Ultrasound transducer convert mechanical waves into electrical signals based on the piezoelectric effect, and vice versa, which are widely used in most medical echography devices and adopted in sensors for optoacoustic signal detection. Given optimal optoacoustic signal generation using pulsed lasers, the detection sensitivity and bandwidth of ultrasound sensors determine the performance of any optoacoustic imaging system in an imaging application [205]. Transducer sensitivity is proportional to the piezoelectric coefficient, proportional to the square root of element area, speed of sound, dielectric constant and the electric capacity, and inversely proportional to the square root of ambient temperature, acoustic impedance and detection bandwidth [205-207]. Therefore, to maximize the area of transducer under the limitation of system integration requirements will increase the detection sensitivity of optoacoustic imaging. Besides, using active material with a high piezoelectric / electromechanical coupling coefficient [205, 208, 209] or with a high speed of sound as well as using optimal production techniques [210, 211] to match acoustic impedance of transducer to the impedance of coupling medium will also improve the detection sensitivity of ultrasound sensors at a given bandwidth for optoacoustic detection. Another way to improve the sensitivity of a given sensor is to integrate an on-chip amplifier and an electrical impedance matching circuit before coupling the captured signal along transmission line [212-216].

Along with the improvement in optoacoustic signal SNR enabled by high-sensitivity ultrasound transducer, better signal preprocessing methods should be applied to optoacoustic signals before image reconstruction. Nowadays, band-pass filter is usually used for preprocessing the optoacoustic signal according to the detection bandwidth of the ultrasound transducer. However, in order to improve the chances of recovering low-intensity information which would be lost in the reconstruction process, more advanced signal processing methods which can increase the SNR of signal should be applied. For example, matched filter is widely used in radar [217], ultrasound [218] and even frequency-domain optoacoustic imaging [219], which is of the ability to differentiate signal from noise by selecting signals consistent with the known excitation characteristics even with low SNR.

Besides improving the SNR with better sensors or signal preprocessing methods, the limitations related to limited-view geometry should be further addressed, since limited-view is inevitable for handheld probes. Our studies in Chapter7 and Chapter 8 have demonstrated that incorporating the structural and SoS information acquired from ultrasound images as priors into optoacoustic image reconstruction improves the image quality of optoacoustic images. In addition, a study has shown that the missing data from the missing detector elements can be estimated and compensated with a Gerchberg–Papoulis extrapolation-based method [220]. Deep learning has also been demonstrated to be potential to compensate the limited- view issue. Therefore, in the future, using machine learning to recover the missing information on the limited-view ultrasound image based on a training dataset of USCT images and ultrasound images from handheld probes, and then compensating for the missing information in limited-view optoacoustic images based on its corresponding co-registered ultrasound image might be a solution for the limited-view issue.

Acknowledgements

At the end of this dissertation, last but not the least, I want to thank everyone who helped me and supported me in my whole PhD journey. I would like to give my special thanks to the following people, because without their guidance or assistance and support in one way or another, this dissertation would not have been possible.

First of all, I am especially grateful to my advisor Prof. Dr. Vasilis Ntziachristos who accepted me as his PhD student and provided extraordinary resource and platform for my research. His deep insights in all fields of imaging guided my research direction and shaped my studies.

My deepest thanks also go to my supervisor Dr. Dominik Jüstel. His wisdom as a scientist, as a supervisor, and as a group leader casted intense light into the darkness in the last years of my PhD study. He supported me by offering profound insights in mathematics and endless patience in administration-related work. His guidance in the last two years of my PhD speeded up my research but most importantly speeded up my personal growth.

I am especially grateful to my other two supervisors during my PhD study. Dr. Stratis Tzoumas who came up with the idea of synthetic data framework study and assisted me with his expertise. The training I got under his supervision laid a good foundation for my later work. Dr. Jayaprakash Naidu who gave me support and offered generous help in the middle stage of my PhD. Special thanks also go to my two previous group leaders Dr. Nicolas Beziere and Dr. Josefine Reber, their support encouraged me to explore my interest without fear and concern when I was lost in the first year.

I would like to thank Dr. Chapin Rodriguez for all his insightful input about my work and generous training about my scientific writing and presentation skills, Dr. Hsiao-Chun Amy Lin, Lu Ding, Ivan Olefir, and Dr. Gael Diot who contributed in valuable discussions, offered generous help and support, and became valuable friends.

I would like to thank Dr. Paul Vetschera for being an excellent roommate by sharing his insights, giving me support and building a happy office. Many thanks to Dr. Murad Omar and Dr. Georg Wissmeyer who showed their caring and kindness and offered their advice in the rainy days of my PhD journey.

My special thanks go to Susanne Stern, Zsuzsanna Oszi, and Lidia Seidl in various aspects of administration and organization related to my PhD and my CSC scholarship. I also want to thank Sarah Glasl who assisted me for all animal experiments, Jan Kukačka who offered generous help in my ultrasound-image-driven SoS reconstruction project, and Dr. Angelos Karlas who supported me for clinical measurements.

Finally, I would not be able to start and accomplish my PhD journey without all the love my families gave me. I want to thank my father Rongfu Yang who gave me the core of who I am today and has always been the lighthouse of my life, my mother Lumei Yang who always offers endless love to accept everything about me, and my brother Tao Yang who always back up my decisions. Last but not least, I would like to give special thanks to my husband Yuanhui Huang. His scientific and personal support as well as his understanding and encouragement make the whole journey possible and wonderful.

Appendix A. List of publications

1. **Yang, H**, Olefir, I, Tzoumas, S, Ntziachristos, V, "Synthetic data framework to estimate the minimum detectable concentration of contrast agents for multispectral optoacoustic imaging of small animals". J. Biophotonics. 2019; 12: e201900021.
2. **Hong Yang**, Dominik Jüstel, Jaya Prakash, Vasilis Ntziachristos, "Modeling the variation in speed of sound between couplant and tissue improves the spectral accuracy of multispectral optoacoustic tomography," Proc. SPIE 10890, Label-free Biomedical Imaging and Sensing (LBIS) 2019, 1089027 (4 March 2019).
3. **Hong Yang**, Dominik Jüstel, Jaya Prakash, Angelos Karlas, Anne Helfen, Max Masthoff, Moritz Wildgruber, Vasilis Ntziachristos, "Soft Ultrasound Priors in Optoacoustic Reconstruction: Improving Clinical Vascular Imaging", Journal of Photoacoustics. 2020.
4. I. Olefir, S. Tzoumas, **H. Yang** and V. Ntziachristos, "A Bayesian Approach to Eigenspectra Optoacoustic Tomography," in IEEE Transactions on Medical Imaging, vol. 37, no. 9, pp. 2070-2079, Sept. 2018.
5. Ivan Olefir, Ara Ghazaryan, **Hong Yang**, Jaber Malekzadeh-Najafabadi, Sarah Glasl, Panagiotis Symvoulidis, Valerie B. O'Leary, George Sergiadis, Vasilis Ntziachristos, Saak V. Ovsepian, "Spatial and Spectral Mapping and Decomposition of Neural Dynamics and Organization of the Mouse Brain with Multispectral Optoacoustic Tomography", Cell Reports, vol. 26, issue 10, 2019.
6. Stephan Kellnberger, Dominik Soliman, George J. Tserevelakis, Markus Seeger, **Hong Yang**, Angelos Karlas, Ludwig Prade, Murad Omar & Vasilis Ntziachristos, "Optoacoustic microscopy at multiple discrete frequencies". Light Sci Appl 7, 109, 2018.

Appendix B. Permission to reuse content from publications

Chapter 3 contains adapted text passages and figures from the publication by Hong Yang et al. [75] © 1999-2019 John Wiley & Sons, Inc .

Chapter 5 contains adapted text passages and figures from the proceedings publications by Hong Yang et al. [102] © 2019 SPIE.

Chapter 7 contains adapted text passages and figures from a published paper in Journal of Photoacoustics by Hong Yang et al. [150] © 2020 Elsevier.

Written permission to reproduce text, figures, and tables have been obtained for all of the above mentioned publications in written form through the Copyright Clearance Center or through direct email contact to the editor. The written copyright and/or permission forms are available upon request.

Bibliography

[1] L. V. Wang, and S. Hu, "Photoacoustic Tomography: In Vivo Imaging from Organelles to Organs," *Science,* vol. 335, no. 6075, pp. 1458-1462, 2012.

[2] V. Ntziachristos, "Going deeper than microscopy: the optical imaging frontier in biology," *Nature Methods,* vol. 7, pp. 603, 07/30/online, 2010.

[3] L. V. Wang, "Multiscale photoacoustic microscopy and computed tomography," *Nature Photonics,* vol. 3, pp. 503, 08/28/online, 2009.

[4] P. Beard, "Biomedical photoacoustic imaging," *Interface focus,* vol. 1, no. 4, pp. 602-631, 2011.

[5] A. G. Bell, "On the production and reproduction of sound by light," *American Journal of Science*, no. 118, pp. 305-324, 1880.

[6] V. Ntziachristos, J. Ripoll, L. V. Wang, and R. Weissleder, "Looking and listening to light: the evolution of whole-body photonic imaging," *Nature biotechnology,* vol. 23, no. 3, pp. 313-320, 2005.

[7] L. V. Wang, "Tutorial on Photoacoustic Microscopy and Computed Tomography," *IEEE Journal of Selected Topics in Quantum Electronics,* vol. 14, no. 1, pp. 171-179, 2008.

[8] V. Ntziachristos, and D. Razansky, "Molecular imaging by means of multispectral optoacoustic tomography (MSOT)," *Chemical reviews,* vol. 110, no. 5, pp. 2783-2794, 2010.

[9] L. V. Wang, *Photoacoustic imaging and spectroscopy*: CRC press, 2009.

[10] A. Taruttis, and V. Ntziachristos, "Advances in real-time multispectral optoacoustic imaging and its applications," *Nature Photonics,* vol. 9, no. 4, pp. 219, 2015.

[11] L. V. Wang, and J. Yao, "A practical guide to photoacoustic tomography in the life sciences," *Nature Methods,* vol. 13, pp. 627, 07/28/online, 2016.

[12] S. A. Ermilov, T. Khamapirad, A. Conjusteau, M. H. Leonard, R. Lacewell, K. Mehta, T. Miller, and A. A. Oraevsky, *Laser optoacoustic imaging system for detection of breast cancer*: SPIE, 2009.

[13] X. L. Deán-Ben, D. Razansky, and V. Ntziachristos, "The effects of acoustic attenuation in optoacoustic signals," *Physics in Medicine & Biology,* vol. 56, no. 18, pp. 6129, 2011.

[14] M. Omar, D. Soliman, J. Gateau, and V. Ntziachristos, "Ultrawideband reflection-mode optoacoustic mesoscopy," *Optics letters,* vol. 39, no. 13, pp. 3911-3914, 2014.

[15] A. Mandelis, "Bioacoustophotonic depth-selective imaging of turbid media and tissues: instrumentation and measurements," *Phys. Can,* vol. 62, pp. 83-90, 2006.

[16] S. Telenkov, A. Mandelis, B. Lashkari, and M. Forcht, "Frequency-domain photothermoacoustics: Alternative imaging modality of biological tissues," *Journal of Applied Physics,* vol. 105, no. 10, pp. 102029, 2009.

[17] S. Kellnberger, N. C. Deliolanis, D. Queirós, G. Sergiadis, and V. Ntziachristos, "In vivo frequency domain optoacoustic tomography," *Optics letters,* vol. 37, no. 16, pp. 3423-3425, 2012.

[18] D. Razansky, C. Vinegoni, and V. Ntziachristos, "Multispectral photoacoustic imaging of fluorochromes in small animals," *Optics letters,* vol. 32, no. 19, pp. 2891-2893, 2007.

[19] R. Ma, A. Taruttis, V. Ntziachristos, and D. Razansky, "Multispectral optoacoustic tomography (MSOT) scanner for whole-body small animal imaging," *Optics Express,* vol. 17, no. 24, pp. 21414-21426, 2009/11/23, 2009.

[20] L. V. Wang, and H.-i. Wu, *Biomedical optics: principles and imaging*: John Wiley & Sons, 2012.

[21] L. A. Sordillo, S. Pratavieira, Y. Pu, K. Salas-Ramirez, L. Shi, L. Zhang, Y. Budansky, and R. R. Alfano, *Third therapeutic spectral window for deep tissue imaging*, p.^pp. PWB: SPIE, 2014.

[22] D. Razansky, N. J. Harlaar, J. L. Hillebrands, A. Taruttis, E. Herzog, C. J. Zeebregts, G. M. van Dam, and V. Ntziachristos, "Multispectral Optoacoustic Tomography of Matrix Metalloproteinase Activity in Vulnerable Human Carotid Plaques," *Molecular Imaging and Biology,* vol. 14, no. 3, pp. 277-285, 2012/06/01, 2012.

[23] S. Tzoumas, A. Nunes, I. Olefir, S. Stangl, P. Symvoulidis, S. Glasl, C. Bayer, G. Multhoff, and V. Ntziachristos, "Eigenspectra optoacoustic tomography achieves quantitative blood oxygenation imaging deep in tissues," *Nature Communications,* vol. 7, pp. 12121, 06/30/online, 2016.

[24] P. Kruizinga, A. F. W. v. d. Steen, N. d. Jong, G. Springeling, J. L. Robertus, A. v. d. Lugt, and G. v. Soest, "Photoacoustic imaging of carotid artery atherosclerosis," *Journal of Biomedical Optics,* vol. 19, no. 11, pp. 1-3, 3, 2014.

[25] T. J. Allen, P. C. Beard, A. Hall, A. P. Dhillon, and J. S. Owen, *Spectroscopic photoacoustic imaging of lipid-rich plaques in the human aorta in the 740 to 1400 nm wavelength range*: SPIE, 2012.

[26] N. C. Deliolanis, A. Ale, S. Morscher, N. C. Burton, K. Schaefer, K. Radrich, D. Razansky, and V. Ntziachristos, "Deep-tissue reporter-gene imaging with fluorescence and optoacoustic tomography: a performance overview," *Molecular Imaging and Biology,* vol. 16, no. 5, pp. 652-660, 2014.

[27] G. S. Filonov, A. Krumholz, J. Xia, J. Yao, L. V. Wang, and V. V. Verkhusha, "Deep-Tissue Photoacoustic Tomography of a Genetically Encoded Near-Infrared Fluorescent Probe," *Angewandte Chemie International Edition,* vol. 51, no. 6, pp. 1448-1451, 2012.

[28] M. Li, J. Oh, X. Xie, G. Ku, W. Wang, C. Li, G. Lungu, G. Stoica, and L. V. Wang, "Simultaneous molecular and hypoxia imaging of brain tumors in vivo using spectroscopic photoacoustic tomography," *Proceedings of the IEEE,* vol. 96, no. 3, pp. 481-489, 2008.

[29] N. Beziere, N. Lozano, A. Nunes, J. Salichs, D. Queiros, K. Kostarelos, and V. Ntziachristos, "Dynamic imaging of PEGylated indocyanine green (ICG) liposomes within the tumor microenvironment using multi-spectral optoacoustic tomography (MSOT)," *Biomaterials,* vol. 37, pp. 415-424, 1//, 2015.

[30] R. A. Kruger, W. L. Kiser, D. R. Reinecke, G. A. Kruger, and K. D. Miller, "Thermoacoustic molecular imaging of small animals," *Molecular Imaging,* vol. 2, no. 2, 2003.

[31] X. Wang, G. Ku, M. A. Wegiel, D. J. Bornhop, G. Stoica, and L. V. Wang, "Noninvasive photoacoustic angiography of animal brains in vivo with near-infrared light and an optical contrast agent," *Optics letters,* vol. 29, no. 7, pp. 730-732, 2004.

[32] G. Ku, and L. V. Wang, "Deeply penetrating photoacoustic tomography in biological tissues enhanced with an optical contrast agent," *Optics letters,* vol. 30, no. 5, pp. 507-509, 2005.

[33] R. Nagaoka, T. Tabata, S. Yoshizawa, S.-i. Umemura, and Y. Saijo, "Visualization of murine lymph vessels using photoacoustic imaging with contrast agents," *Photoacoustics,* vol. 9, pp. 39-48, 2018.

[34] A. De La Zerda, C. Zavaleta, S. Keren, S. Vaithilingam, S. Bodapati, Z. Liu, J. Levi, B. R. Smith, T.-J. Ma, and O. Oralkan, "Carbon nanotubes as photoacoustic molecular imaging agents in living mice," *Nature nanotechnology,* vol. 3, no. 9, pp. 557-562, 2008.

[35] H. Aoki, M. Nojiri, R. Mukai, and S. Ito, "Near-infrared absorbing polymer nano-particle as a sensitive contrast agent for photo-acoustic imaging," *Nanoscale,* vol. 7, no. 1, pp. 337-343, 2015.

[36] J. V. Jokerst, D. Van de Sompel, S. E. Bohndiek, and S. S. Gambhir, "Cellulose nanoparticles are a biodegradable photoacoustic contrast agent for use in living mice," *Photoacoustics,* vol. 2, no. 3, pp. 119-127, 2014.

[37] A. Taruttis, E. Herzog, D. Razansky, and V. Ntziachristos, "Real-time imaging of cardiovascular dynamics and circulating gold nanorods with multispectral optoacoustic tomography," *Optics Express,* vol. 18, no. 19, pp. 19592-19602, 2010/09/13, 2010.

[38] J. V. Jokerst, A. J. Cole, D. Van de Sompel, and S. S. Gambhir, "Gold nanorods for ovarian cancer detection with photoacoustic imaging and resection guidance via Raman imaging in living mice," *ACS nano,* vol. 6, no. 11, pp. 10366-10377, 2012.

[39] S. Tzoumas, A. Nunes, N. C. Deliolanis, and V. Ntziachristos, "Effects of multispectral excitation on the sensitivity of molecular optoacoustic imaging," *Journal of biophotonics,* vol. 8, no. 8, pp. 629-637, 2015.

[40] J. Xia, and L. V. Wang, "Small-Animal Whole-Body Photoacoustic Tomography: A Review," *IEEE Transactions on Biomedical Engineering,* vol. 61, no. 5, pp. 1380-1389, 2014.

[41] D. Razansky, A. Buehler, and V. Ntziachristos, "Volumetric real-time multispectral optoacoustic tomography of biomarkers," *Nature protocols,* vol. 6, no. 8, pp. 1121-1129, 2011.

[42] A. Dima, N. C. Burton, and V. Ntziachristos, "Multispectral optoacoustic tomography at 64, 128, and 256 channels," *Journal of biomedical optics,* vol. 19, no. 3, pp. 036021-036021, 2014.

[43] I. Stoffels, S. Morscher, I. Helfrich, U. Hillen, J. Leyh, N. C. Burton, T. C. Sardella, J. Claussen, T. D. Poeppel, and H. S. Bachmann, "Metastatic status of sentinel lymph nodes in melanoma determined noninvasively with multispectral optoacoustic imaging," *Science Translational Medicine,* vol. 7, no. 317, pp. 317ra199-317ra199, 2015.

[44] K. S. Valluru, and J. K. Willmann, "Clinical photoacoustic imaging of cancer," *Ultrasonography,* vol. 35, no. 4, pp. 267, 2016.

[45] K. S. Valluru, K. E. Wilson, and J. K. Willmann, “Photoacoustic Imaging in oncology: translational preclinical and early clinical experience,” *Radiology,* vol. 280, no. 2, pp. 332-349, 2016.

[46] A. Garcia-Uribe, T. N. Erpelding, A. Krumholz, H. Ke, K. Maslov, C. Appleton, J. A. Margenthaler, and L. V. Wang, “Dual-modality photoacoustic and ultrasound imaging system for noninvasive sentinel lymph node detection in patients with breast cancer,” *Scientific reports,* vol. 5, pp. 15748, 2015.

[47] F. Knieling, C. Neufert, A. Hartmann, J. Claussen, A. Urich, C. Egger, M. Vetter, S. Fischer, L. Pfeifer, and A. Hagel, “Multispectral Optoacoustic Tomography for Assessment of Crohn’s Disease Activity,” *N Engl J Med,* vol. 2017, no. 376, pp. 1292-1294, 2017.

[48] J. Jo, G. Xu, M. Cao, A. Marquardt, S. Francis, G. Gandikota, and X. Wang, “A Functional Study of Human Inflammatory Arthritis Using Photoacoustic Imaging,” *Scientific reports,* vol. 7, no. 1, pp. 15026, 2017.

[49] J. Reber, M. Willershäuser, A. Karlas, K. Paul-Yuan, G. Diot, D. Franz, T. Fromme, S. V. Ovsepian, N. Bézière, and E. Dubikovskaya, “Non-invasive measurement of brown fat metabolism based on optoacoustic imaging of hemoglobin gradients,” *Cell metabolism,* vol. 27, no. 3, pp. 689-701. e4, 2018.

[50] A. Chekkoury, A. Nunes, J. Gateau, P. Symvoulidis, A. Feuchtinger, N. Beziere, S. V. Ovsepian, A. Walch, and V. Ntziachristos, “High-Resolution Multispectral Optoacoustic Tomography of the Vascularization and Constitutive Hypoxemia of Cancerous Tumors,” *Neoplasia,* vol. 18, no. 8, pp. 459-467, 2016.

[51] A. Taruttis, A. C. Timmermans, P. C. Wouters, M. Kacprowicz, G. M. van Dam, and V. Ntziachristos, “Optoacoustic imaging of human vasculature: feasibility by using a handheld probe,” *Radiology,* vol. 281, no. 1, pp. 256-263, 2016.

[52] M. Toi, Y. Asao, Y. Matsumoto, H. Sekiguchi, A. Yoshikawa, M. Takada, M. Kataoka, T. Endo, N. Kawaguchi-Sakita, and M. Kawashima, “Visualization of tumor-related blood vessels in human breast by photoacoustic imaging system with a hemispherical detector array,” *Scientific reports,* vol. 7, pp. 41970, 2017.

[53] M. F. Kircher, A. De La Zerda, J. V. Jokerst, C. L. Zavaleta, P. J. Kempen, E. Mittra, K. Pitter, R. Huang, C. Campos, and F. Habte, “A brain tumor molecular imaging strategy using a new triple-modality MRI-photoacoustic-Raman nanoparticle,” *Nature medicine,* vol. 18, no. 5, pp. 829-834, 2012.

[54] B. Wang, J. L. Su, J. Amirian, S. H. Litovsky, R. Smalling, and S. Emelianov, “Detection of lipid in atherosclerotic vessels using ultrasound-guided spectroscopic intravascular photoacoustic imaging,” *Optics express,* vol. 18, no. 5, pp. 4889-4897, 2010.

[55] C. Kim, T. N. Erpelding, L. Jankovic, M. D. Pashley, and L. V. Wang, “Deeply penetrating in vivo photoacoustic imaging using a clinical ultrasound array system,” *Biomedical optics express,* vol. 1, no. 1, pp. 278-284, 2010.

[56] J. Jo, G. Xu, A. Marquardt, G. Girish, and X. Wang, "Photoacoustic evaluation of human inflammatory arthritis in human joints." pp. 1006409-1.

[57] J. Kima, M.-H. Kimb, K. Job, J. Hab, Y. Kima, D.-J. Limb, and C. Kima, "Photoacoustic analysis of thyroid cancer in vivo: A pilot study." pp. 1006408-1.

[58] P. J. van den Berg, R. Bansal, K. Daoudi, W. Steenbergen, and J. Prakash, “Preclinical detection of liver fibrosis using dual-modality photoacoustic/ultrasound system,” *Biomedical Optics Express,* vol. 7, no. 12, pp. 5081-5091, 2016.

[59] B. Cox, J. G. Laufer, S. R. Arridge, and P. C. Beard, “Quantitative spectroscopic photoacoustic imaging: a review,” *Journal of biomedical optics,* vol. 17, no. 6, pp. 0612021-06120222, 2012.

[60] A. D. Pierce, and R. T. Beyer, "Acoustics: An introduction to its physical principles and applications. 1989 Edition," ASA, 1990.

[61] S. I. Nikolov, “Synthetic aperture tissue and flow ultrasound imaging,” PhD thesis, Ørsted• DTU, Technical University of Denmark, 2800, Lyngby, Denmark, 2001.

[62] D. Queirós, “Image Reconstruction in Optoacoustics,” Technische Universität München, 2015.

[63] X. L. Dean-Ben, V. Ntziachristos, and D. Razansky, “Acceleration of optoacoustic model-based reconstruction using angular image discretization,” *IEEE Transactions on medical imaging,* vol. 31, no. 5, pp. 1154-1162, 2012.

[64] M. Xu, and L. V. Wang, “Universal back-projection algorithm for photoacoustic computed tomography,” *Physical Review E,* vol. 71, no. 1, pp. 016706, 2005.

[65] A. Rosenthal, D. Razansky, and V. Ntziachristos, “Fast semi-analytical model-based acoustic inversion for quantitative optoacoustic tomography,” *IEEE transactions on medical imaging,* vol. 29, no. 6, pp. 1275-1285, 2010.

[66] K. P. Köstli, M. Frenz, H. Bebie, and H. P. Weber, “Temporal backward projection of optoacoustic pressure transients using Fourier transform methods,” *Physics in medicine and biology,* vol. 46, no. 7, pp. 1863, 2001.

[67] A. Buehler, A. Rosenthal, T. Jetzfellner, A. Dima, D. Razansky, and V. Ntziachristos, "Model-based optoacoustic inversions with incomplete projection data," *Medical physics,* vol. 38, no. 3, pp. 1694-1704, 2011.

[68] A. Rosenthal, “Algebraic determination of back-projection operators for optoacoustic tomography,” *Biomedical Optics Express,* vol. 9, no. 11, pp. 5173-5193, 2018/11/01, 2018.

[69] X. L. Deán-Ben, V. Ntziachristos, and D. Razansky, “Acceleration of optoacoustic model-based reconstruction using angular image discretization,” *IEEE Transactions on medical imaging,* vol. 31, no. 5, pp. 1154-1162, 2012.

[70] P. C. Hansen, “Analysis of discrete ill-posed problems by means of the L-curve,” *SIAM review,* vol. 34, no. 4, pp. 561-580, 1992.

[71] S. Tzoumas, A. Kravtsiv, Y. Gao, A. Buehler, and V. Ntziachristos, “Statistical Molecular Target Detection Framework for Multispectral Optoacoustic Tomography,” *IEEE Transactions on Medical Imaging,* vol. 35, no. 12, pp. 2534-2545, 2016.

[72] S. Tzoumas, A. Nunes, I. Olefir, S. Stangl, P. Symvoulidis, S. Glasl, C. Bayer, G. Multhoff, and V. Ntziachristos, “Eigenspectra optoacoustic tomography achieves quantitative blood oxygenation imaging deep in tissues,” *Nature communications,* vol. 7, 2016.

[73] E. W. Stein, K. I. Maslov, and L. V. Wang, “Noninvasive, in vivo imaging of blood-oxygenation dynamics within the mouse brain using photoacoustic microscopy,” *Journal of biomedical optics,* vol. 14, no. 2, pp. 020502, 2009.

[74] S. Tzoumas, N. Deliolanis, S. Morscher, and V. Ntziachristos, "Unmixing molecular agents from absorbing tissue in multispectral optoacoustic tomography," *IEEE Transactions on Medical Imaging,* vol. 33, no. 1, pp. 48-60, 2014.

[75] H. Yang, I. Olefir, S. Tzoumas, and V. Ntziachristos, "Synthetic data framework to estimate the minimum detectable concentration of contrast agents for multispectral optoacoustic imaging of small animals," *Journal of Biophotonics,* vol. 0, no. ja, pp. e201900021.

[76] T. F. Massoud, and S. S. Gambhir, "Molecular imaging in living subjects: seeing fundamental biological processes in a new light," *Genes & development,* vol. 17, no. 5, pp. 545-580, 2003.

[77] S. S. Gambhir, "Molecular imaging of cancer with positron emission tomography," *Nature Reviews Cancer,* vol. 2, no. 9, pp. 683, 2002.

[78] D. Razansky, J. Baeten, and V. Ntziachristos, "Sensitivity of molecular target detection by multispectral optoacoustic tomography (MSOT)," *Medical physics,* vol. 36, no. 3, pp. 939-945, 2009.

[79] A. Hariri, J. Lemaster, J. Wang, A. S. Jeevarathinam, D. L. Chao, and J. V. Jokerst, "The characterization of an economic and portable LED-based photoacoustic imaging system to facilitate molecular imaging," *Photoacoustics,* vol. 9, pp. 10-20, 2018.

[80] D. Queirós, X. L. Déan-Ben, A. Buehler, D. Razansky, A. Rosenthal, and V. Ntziachristos, "Modeling the shape of cylindrically focused transducers in three-dimensional optoacoustic tomography," *Journal of biomedical optics,* vol. 18, no. 7, pp. 076014-076014, 2013.

[81] X. L. Deán-Ben, D. Razansky, and V. Ntziachristos, "The effects of acoustic attenuation in optoacoustic signals," *Physics in medicine and biology,* vol. 56, no. 18, pp. 6129, 2011.

[82] T. L. Szabo, *Diagnostic ultrasound imaging: inside out*: Academic Press, 2004.

[83] A. Rosenthal, V. Ntziachristos, and D. Razansky, "Model-based optoacoustic inversion with arbitrary-shape detectors," *Medical physics,* vol. 38, no. 7, pp. 4285-4295, 2011.

[84] D. Hyde, R. Schulz, D. Brooks, E. Miller, and V. Ntziachristos, "Performance dependence of hybrid x-ray computed tomography/fluorescence molecular tomography on the optical forward problem," *JOSA A,* vol. 26, no. 4, pp. 919-923, 2009.

[85] J. P. Ritz, A. Roggan, C. T. Germer, C. Isbert, G. Müller, and H. J. Buhr, "Continuous changes in the optical properties of liver tissue during laser-induced interstitial thermotherapy," *Lasers in Surgery and Medicine: The Official Journal of the American Society for Laser Medicine and Surgery,* vol. 28, no. 4, pp. 307-312, 2001.

[86] S. L. Jacques, "Optical properties of biological tissues: a review," *Physics in medicine and biology,* vol. 58, no. 11, pp. R37, 2013.

[87] A. Tsaroucha, A. Paraskeva, and A. Fassoulaki, "Measurements of oxygen saturation of brain, liver and heart areas in the supine and sitting position using near infrared spectrophotometry," *Romanian journal of anaesthesia and intensive care,* vol. 24, no. 2, pp. 101, 2017.

[88] J. Levi, A. Sathirachinda, and S. S. Gambhir, "A high affinity, high stability photoacoustic agent for imaging gastrin releasing peptide receptor in prostate cancer," *Clinical Cancer Research*, pp. clincanres. 3405.2013, 2014.

[89] R. Su, A. Liopo, S. A. Ermilov, and A. A. Oraevsky, "Small animal optoacoustic tomography system for molecular imaging of contrast agents." p. 97081S.

[90] C. Liu, Y. Yang, Z. Qiu, Y. Huang, and L. Sun, "In vivo assessment of protease activity in colorectal cancer by using activatable molecular photoacoustic imaging." pp. 1-4.

[91] A. Agarwal, X. Shao, J. R. Rajian, H. Zhang, D. L. Chamberland, N. A. Kotov, and X. Wang, "Dual-mode imaging with radiolabeled gold nanorods," *Journal of biomedical optics,* vol. 16, no. 5, pp. 051307-051307-7, 2011.

[92] W. Xia, M. Kuniyil Ajith Singh, E. Maneas, N. Sato, Y. Shigeta, T. Agano, S. Ourselin, S. J. West, and A. E. Desjardins, "Handheld Real-Time LED-Based Photoacoustic and Ultrasound Imaging System for Accurate Visualization of Clinical Metal Needles and Superficial Vasculature to Guide Minimally Invasive Procedures," *Sensors,* vol. 18, no. 5, pp. 1394, 2018.

[93] P. J. v. d. Berg, K. Daoudi, and W. Steenbergen, *Pulsed photoacoustic flow imaging with a handheld system*: SPIE, 2016.

[94] A. Horiguchi, K. Tsujita, K. Irisawa, T. Kasamatsu, K. Hirota, M. Kawaguchi, M. Shinchi, K. Ito, T. Asano, H. Shinmoto, H. Tsuda, and M. Ishihara, "A pilot study of photoacoustic imaging system for improved real-time visualization of neurovascular bundle during radical prostatectomy," *The Prostate,* vol. 76, no. 3, pp. 307-315, 2016.

[95] Y. Uchimoto, T. Namita, K. Kondo, M. Yamakawa, and T. Shiina, *Feasibility evaluation of 3D photoacoustic imaging of blood vessel structure using multiple wavelengths with a handheld probe*, p.^pp. PWB: SPIE, 2018.

[96] E. Merčep, X. L. Deán-Ben, and D. Razansky, "Combined pulse-echo ultrasound and multispectral optoacoustic tomography with a multi-segment detector array," *IEEE transactions on medical imaging,* vol. 36, no. 10, pp. 2129-2137, 2017.

[97] E. Mercep, G. Jeng, S. Morscher, P.-C. Li, and D. Razansky, "Hybrid optoacoustic tomography and pulse-echo ultrasonography using concave arrays," *IEEE transactions on ultrasonics, ferroelectrics, and frequency control,* vol. 62, no. 9, pp. 1651-1661, 2015.

[98] A. V. Oppenheim, *Discrete-time signal processing*: Pearson Education India, 1999.

[99] A. Bychkov, V. Simonova, V. Zarubin, E. Cherepetskaya, and A. Karabutov, "The Progress in Photoacoustic and Laser Ultrasonic Tomographic Imaging for Biomedicine and Industry: A Review," *Applied Sciences,* vol. 8, no. 10, pp. 1931, 2018.

[100] J. Gateau, M. Á. A. Caballero, A. Dima, and V. Ntziachristos, "Three‐dimensional optoacoustic tomography using a conventional ultrasound linear detector array: Whole‐body tomographic system for small animals," *Medical physics,* vol. 40, no. 1, 2013.

[101] X. Wang, J. B. Fowlkes, J. M. Cannata, C. Hu, and P. L. Carson, "Photoacoustic Imaging With a Commercial Ultrasound System and a Custom Probe," *Ultrasound in Medicine & Biology,* vol. 37, no. 3, pp. 484-492, 2011/03/01/, 2011.

[102] H. Yang, D. Jüstel, J. Prakash, and V. Ntziachristos, *Modeling the variation in speed of sound between couplant and tissue improves the spectral accuracy of multispectral optoacoustic tomography*, p.^pp. PWB: SPIE, 2019.

[103] X. L. Deán‐Ben, V. Ntziachristos, and D. Razansky, "Effects of small variations of speed of sound in optoacoustic tomographic imaging," *Medical physics,* vol. 41, no. 7, 2014.

[104] A. Buehler, G. Diot, T. Volz, J. Kohlmeyer, and V. Ntziachristos, “Imaging of fatty tumors: appearance of subcutaneous lipomas in optoacoustic images,” *Journal of Biophotonics*, 2017.

[105] H. Azhari, “Typical acoustic properties of tissues,” *Basics of Biomedical Ultrasound for Engineers*, pp. 313-314, 2010.

[106] J. Bayly, V. Kartha, and W. Stevens, “The absorption spectra of liquid phase H2O, HDO and D2O from 0· 7 μm to 10 μm,” *Infrared Physics,* vol. 3, no. 4, pp. 211-222, 1963.

[107] A. E. Zavodni, B. A. Wasserman, R. L. McClelland, A. S. Gomes, A. R. Folsom, J. F. Polak, J. A. Lima, and D. A. Bluemke, “Carotid artery plaque morphology and composition in relation to incident cardiovascular events: the Multi-Ethnic Study of Atherosclerosis (MESA),” *Radiology,* vol. 271, no. 2, pp. 381-389, 2014.

[108] J. Wang, B. W. Pogue, S. Jiang, and K. D. Paulsen, “Near-infrared tomography of breast cancer hemoglobin, water, lipid, and scattering using combined frequency domain and cw measurement,” *Optics letters,* vol. 35, no. 1, pp. 82-84, 2010.

[109] J. Jose, R. G. Willemink, W. Steenbergen, C. H. Slump, T. G. van Leeuwen, and S. Manohar, “Speed‐of‐sound compensated photoacoustic tomography for accurate imaging,” *Medical physics,* vol. 39, no. 12, pp. 7262-7271, 2012.

[110] L. Li, L. Zhu, C. Ma, L. Lin, J. Yao, L. Wang, K. Maslov, R. Zhang, W. Chen, and J. Shi, “Single-impulse panoramic photoacoustic computed tomography of small-animal whole-body dynamics at high spatiotemporal resolution,” *Nature Biomedical Engineering,* vol. 1, no. 5, pp. Art. No. 0071, 2017.

[111] B. J. Frey, and D. Dueck, “Clustering by passing messages between data points,” *science,* vol. 315, no. 5814, pp. 972-976, 2007.

[112] Oregon Medical Laser Center. "Optical Spectra," 27 Sep., 2017; http://omlc.org/spectra/index.html.

[113] A. Carovac, F. Smajlovic, and D. Junuzovic, “Application of ultrasound in medicine,” *Acta Informatica Medica,* vol. 19, no. 3, pp. 168, 2011.

[114] P. Cinquin, S. Lavallee, F. Dubois, L. Brunie, J. Troccaz, O. Peria, and B. Mazier, "Method for determining the position of an organ," Google Patents, 1995.

[115] P. A. Dayton, and K. W. Ferrara, “Targeted imaging using ultrasound,” *Journal of Magnetic Resonance Imaging: An Official Journal of the International Society for Magnetic Resonance in Medicine,* vol. 16, no. 4, pp. 362-377, 2002.

[116] C. M. Sehgal, S. P. Weinstein, P. H. Arger, and E. F. Conant, “A review of breast ultrasound,” *Journal of mammary gland biology and neoplasia,* vol. 11, no. 2, pp. 113-123, 2006.

[117] D. Hiller, and H. Ermert, "Ultrasound computerized tomography using transmission and reflection mode: Application to medical diagnosis," *Acoustical imaging*, pp. 553-563: Springer, 1982.

[118] K. J. Opieliński, P. Pruchnicki, T. Gudra, P. Podgórski, T. Kraśnicki, J. Kurcz, and M. Sąsiadek, “Ultrasound transmission tomography imaging of structure of breast elastography phantom compared to US, CT and MRI,” *Archives of Acoustics,* vol. 38, no. 3, pp. 321-334, 2013.

[119] S. W. Flax, N. J. Pelc, G. H. Glover, F. D. Gutmann, and M. McLachlan, "Spectral characterization and attenuation measurements in ultrasound," *Ultrasonic Imaging,* vol. 5, no. 2, pp. 95-116, 1983.

[120] E. L. Madsen, F. Dong, G. R. Frank, B. S. Garra, K. A. Wear, T. Wilson, J. A. Zagzebski, H. L. Miller, K. K. Shung, and S. Wang, "Interlaboratory comparison of ultrasonic backscatter, attenuation, and speed measurements," *Journal of ultrasound in medicine,* vol. 18, no. 9, pp. 615-631, 1999.

[121] C. Pintavirooj, A. Romputtal, A. Ngamlamiad, W. Withayachumnankul, and K. Hamamoto, "Ultrasonic refractive index tomography," 2004.

[122] P. W. Callen, "Ultrasonography in obstetrics and gynecology," 1988.

[123] B. B. Goldberg, and H. M. Pollack, "Differentiation of renal masses using A-mode ultrasound," *The Journal of urology,* vol. 105, no. 6, pp. 765-771, 1971.

[124] C. Adam, F. Eckstein, S. Milz, E. Schulte, C. Becker, and R. Putz, "The distribution of cartilage thickness in the knee-joints of old-aged individuals—measurement by A-mode ultrasound," *Clinical Biomechanics,* vol. 13, no. 1, pp. 1-10, 1998.

[125] A. Mozes, T. C. Chang, L. Arata, and W. Zhao, "Three-dimensional A-mode ultrasound calibration and registration for robotic orthopaedic knee surgery," *The international journal of medical robotics and computer assisted surgery,* vol. 6, no. 1, pp. 91-101, 2010.

[126] B. Buckrell, B. Bonnett, and W. Johnson, "The use of real-time ultrasound rectally for early pregnancy diagnosis in sheep," *Theriogenology,* vol. 25, no. 5, pp. 665-673, 1986.

[127] F. A. Chervenak, R. L. Berkowitz, R. Romero, M. Tortora, K. Mayden, C. Duncan, M. J. Mahoney, and J. C. Hobbins, "The diagnosis of fetal hydrocephalus," *American journal of obstetrics and gynecology,* vol. 147, no. 6, pp. 703-716, 1983.

[128] S. S. Kang, N. Labropoulos, M. A. Mansour, M. Michelini, D. Filliung, M. P. Baubly, and W. H. Baker, "Expanded indications for ultrasound-guided thrombin injection of pseudoaneurysms," *Journal of vascular surgery,* vol. 31, no. 2, pp. 289-298, 2000.

[129] H. Zhi, B. Ou, B.-M. Luo, X. Feng, Y.-L. Wen, and H.-Y. Yang, "Comparison of ultrasound elastography, mammography, and sonography in the diagnosis of solid breast lesions," *Journal of ultrasound in medicine,* vol. 26, no. 6, pp. 807-815, 2007.

[130] G. Heiss, A. R. Sharrett, R. Barnes, L. Chambless, M. Szklo, C. Alzola, and A. Investigators, "Carotid atherosclerosis measured by B-mode ultrasound in populations: associations with cardiovascular risk factors in the ARIC study," *American journal of epidemiology,* vol. 134, no. 3, pp. 250-256, 1991.

[131] C. Kasai, K. Namekawa, A. Koyano, and R. Omoto, "Real-time two-dimensional blood flow imaging using an autocorrelation technique," *IEEE Transactions on sonics and ultrasonics,* vol. 32, no. 3, pp. 458-464, 1985.

[132] A. Fenster, D. B. Downey, and H. N. Cardinal, "Three-dimensional ultrasound imaging," *Physics in medicine & biology,* vol. 46, no. 5, pp. R67, 2001.

[133] A. C. Kak, "Computerized tomography with X-ray, emission, and ultrasound sources," *Proceedings of the IEEE,* vol. 67, no. 9, pp. 1245-1272, 1979.

[134] D. A. Feinberg, D. Giese, D. A. Bongers, S. Ramanna, M. Zaitsev, M. Markl, and M. Günther, "Hybrid ultrasound MRI for improved cardiac imaging and real-time respiration control,"

Magnetic Resonance in Medicine: An Official Journal of the International Society for Magnetic Resonance in Medicine, vol. 63, no. 2, pp. 290-296, 2010.

[135] B. Hwangbo, S. K. Kim, H.-S. Lee, H. S. Lee, M. S. Kim, J. M. Lee, H.-Y. Kim, G.-K. Lee, B.-H. Nam, and J. I. Zo, "Application of endobronchial ultrasound-guided transbronchial needle aspiration following integrated PET/CT in mediastinal staging of potentially operable non-small cell lung cancer," *Chest,* vol. 135, no. 5, pp. 1280-1287, 2009.

[136] R. Pani, R. Pellegrini, M. Cinti, P. Bennati, A. Fabbri, S. Ridolfi, R. Scafè, G. De Vincentis, E. Di Castro, and N. Polli, "Dual modality ultrasound-SPET detector for molecular imaging," *Nuclear Physics B-Proceedings Supplements,* vol. 215, no. 1, pp. 319-323, 2011.

[137] L. E. Kinsler, A. R. Frey, A. B. Coppens, and J. V. Sanders, "Fundamentals of acoustics," *Fundamentals of Acoustics, 4th Edition, by Lawrence E. Kinsler, Austin R. Frey, Alan B. Coppens, James V. Sanders, pp. 560. ISBN 0-471-84789-5. Wiley-VCH, December 1999.*, pp. 560, 1999.

[138] K. E. Thomenius, "Evolution of ultrasound beamformers." pp. 1615-1622.

[139] N. C. Dalrymple, S. R. Prasad, M. W. Freckleton, and K. N. Chintapalli, "Introduction to the language of three-dimensional imaging with multidetector CT," *Radiographics,* vol. 25, no. 5, pp. 1409-1428, 2005.

[140] M. Heijblom, W. Steenbergen, and S. Manohar, "Clinical photoacoustic breast imaging: the twente experience," *IEEE pulse,* vol. 6, no. 3, pp. 42-46, 2015.

[141] S. Napel, M. Marks, G. Rubin, M. Dake, C. McDonnell, S. Song, D. Enzmann, and R. Jeffrey Jr, "CT angiography with spiral CT and maximum intensity projection," *Radiology,* vol. 185, no. 2, pp. 607-610, 1992.

[142] C. M. Anderson, D. Saloner, J. S. Tsuruda, L. G. Shapeero, and R. E. Lee, "Artifacts in maximum-intensity-projection display of MR angiograms," *AJR. American journal of roentgenology,* vol. 154, no. 3, pp. 623-629, 1990.

[143] J. J. Kaufman, and T. A. Einhorn, "Perspectives: Ultrasound assessment of bone," *Journal of Bone and Mineral Research,* vol. 8, no. 5, pp. 517-525, 1993.

[144] J. Kirkhorn, "Introduction to IQ-demodulation of RF-data," *IFBT, NTNU,* vol. 15, 1999.

[145] D. Benitez, P. Gaydecki, A. Zaidi, and A. Fitzpatrick, "The use of the Hilbert transform in ECG signal analysis," *Computers in biology and medicine,* vol. 31, no. 5, pp. 399-406, 2001.

[146] R. Stotzka, N. V. Ruiter, T. O. Müller, R. Liu, and H. Gemmeke, "High resolution image reconstruction in ultrasound computer tomography using deconvolution." pp. 315-326.

[147] S. I. Nikolov, and J. A. Jensen, "Application of different spatial sampling patterns for sparse array transducer design," *Ultrasonics,* vol. 37, no. 10, pp. 667-671, 2000.

[148] G. R. Lockwood, P.-C. Li, M. O'Donnell, and F. S. Foster, "Optimizing the radiation pattern of sparse periodic linear arrays," *IEEE Transactions on Ultrasonics, Ferroelectrics, and frequency control,* vol. 43, no. 1, pp. 7-14, 1996.

[149] G. Lockwood, and F. S. Foster, "Optimizing sparse two-dimensional transducer arrays using an effective aperture approach." pp. 1497-1501.

[150] H. Yang, D. Jüstel, J. Prakash, A. Karlas, A. Helfen, M. Masthoff, M. Wildgruber, and V. Ntziachristos, "Soft Ultrasound Priors in Optoacoustic Reconstruction: Improving Clinical Vascular Imaging," *Photoacoustics*, pp. 100172, 2020/03/10/, 2020.

[151] A. Rosenthal, V. Ntziachristos, and D. Razansky, “Acoustic inversion in optoacoustic tomography: A review,” *Current medical imaging reviews,* vol. 9, no. 4, pp. 318, 2013.

[152] J. r. Frikel, and E. T. Quinto, “Artifacts in incomplete data tomography with applications to photoacoustic tomography and sonar,” *SIAM Journal on Applied Mathematics,* vol. 75, no. 2, pp. 703-725, 2015.

[153] X. L. Deán-Ben, and D. Razansky, “On the link between the speckle free nature of optoacoustics and visibility of structures in limited-view tomography,” *Photoacoustics,* vol. 4, no. 4, pp. 133-140, 2016.

[154] Y. Xu, L. V. Wang, G. Ambartsoumian, and P. Kuchment, "Reconstructions in limited-view thermoacoustic tomography," *Medical physics,* vol. 31, no. 4, pp. 724-733, 2004.

[155] W. Dan, T. Chao, L. Xiao-Jun, and W. Xue-Ding, “Influence of limited-view scanning on depth imaging of photoacoustic tomography,” *Chinese Physics B,* vol. 21, no. 1, pp. 014301, 2012.

[156] L. Yao, and H. Jiang, “Photoacoustic image reconstruction from few-detector and limited-angle data,” *Biomedical optics express,* vol. 2, no. 9, pp. 2649-2654, 2011.

[157] J. Frikel, and M. Haltmeier, “Efficient regularization with wavelet sparsity constraints in PAT,” *arXiv preprint arXiv:1703.08240*, 2017.

[158] A. Rosenthal, T. Jetzfellner, D. Razansky, and V. Ntziachristos, “Efficient framework for model-based tomographic image reconstruction using wavelet packets,” *IEEE transactions on medical imaging,* vol. 31, no. 7, pp. 1346-1357, 2012.

[159] J. Kim, S. Park, Y. Jung, S. Chang, J. Park, Y. Zhang, J. F. Lovell, and C. Kim, “Programmable real-time clinical photoacoustic and ultrasound imaging system,” *Scientific reports,* vol. 6, 2016.

[160] K. Sivasubramanian, and M. Pramanik, “High frame rate photoacoustic imaging at 7000 frames per second using clinical ultrasound system,” *Biomedical optics express,* vol. 7, no. 2, pp. 312-323, 2016.

[161] C. Kim, T. N. Erpelding, L. Jankovic, and L. V. Wang, “Performance benchmarks of an array-based hand-held photoacoustic probe adapted from a clinical ultrasound system for non-invasive sentinel lymph node imaging,” *Philosophical Transactions of the Royal Society of London A: Mathematical, Physical and Engineering Sciences,* vol. 369, no. 1955, pp. 4644-4650, 2011.

[162] C.-W. Wei, T.-M. Nguyen, J. Xia, B. Arnal, E. Y. Wong, I. M. Pelivanov, and M. O'Donnell, “Real-time integrated photoacoustic and ultrasound (PAUS) imaging system to guide interventional procedures: ex vivo study,” *IEEE transactions on ultrasonics, ferroelectrics, and frequency control,* vol. 62, no. 2, pp. 319-328, 2015.

[163] M. K. A. Singh, W. Steenbergen, and S. Manohar, "Handheld probe-based dual mode ultrasound/photoacoustics for biomedical imaging," *Frontiers in Biophotonics for Translational Medicine*, pp. 209-247: Springer, 2016.

[164] M. K. A. Singh, and W. Steenbergen, “Photoacoustic-guided focused ultrasound (PAFUSion) for identifying reflection artifacts in photoacoustic imaging,” *Photoacoustics,* vol. 3, no. 4, pp. 123-131, 2015.

[165] J. Xia, C. Huang, K. Maslov, M. A. Anastasio, and L. V. Wang, "Enhancement of photoacoustic tomography by ultrasonic computed tomography based on optical excitation of elements of a full-ring transducer array," *Optics letters,* vol. 38, no. 16, pp. 3140-3143, 2013.

[166] P. K. Yalavarthy, B. W. Pogue, H. Dehghani, and K. D. Paulsen, "Weight-matrix structured regularization provides optimal generalized least-squares estimate in diffuse optical tomography," *Medical physics,* vol. 34, no. 6Part1, pp. 2085-2098, 2007.

[167] P. K. Yalavarthy, B. W. Pogue, H. Dehghani, C. M. Carpenter, S. Jiang, and K. D. Paulsen, "Structural information within regularization matrices improves near infrared diffuse optical tomography," *Optics Express,* vol. 15, no. 13, pp. 8043-8058, 2007.

[168] Y. Han, S. Tzoumas, A. Nunes, V. Ntziachristos, and A. Rosenthal, "Sparsity-based acoustic inversion in cross-sectional multiscale optoacoustic imaging," *Medical physics,* vol. 42, no. 9, pp. 5444-5452, 2015.

[169] A. C. Bovik, *Handbook of image and video processing*: Academic press, 2010.

[170] D. Hyde, E. L. Miller, D. H. Brooks, and V. Ntziachristos, "Data specific spatially varying regularization for multimodal fluorescence molecular tomography," *IEEE transactions on medical imaging,* vol. 29, no. 2, pp. 365-374, 2010.

[171] F. Timischl, "The contrast-to-noise ratio for image quality evaluation in scanning electron microscopy," *Scanning,* vol. 37, no. 1, pp. 54-62, 2015.

[172] Z. Wang, A. C. Bovik, H. R. Sheikh, and E. P. Simoncelli, "Image quality assessment: from error visibility to structural similarity," *IEEE transactions on image processing,* vol. 13, no. 4, pp. 600-612, 2004.

[173] J. P. Peruga, J. Z. Peruga, J. D. Kasprzak, R. Kręcki, Ł. Jankowski, P. Zając, and M. Plewka, "Ultrasound evaluation of forearm arteries in patients undergoing percutaneous coronary intervention via radial artery access: results of one-year follow-up," *Kardiologia Polska (Polish Heart Journal),* vol. 73, no. 7, pp. 502-510, 2015.

[174] M. W. Lorenz, H. S. Markus, M. L. Bots, M. Rosvall, and M. Sitzer, "Prediction of clinical cardiovascular events with carotid intima-media thickness: a systematic review and meta-analysis," *Circulation,* vol. 115, no. 4, pp. 459-467, 2007.

[175] P. E. Kinahan, B. H. Hasegawa, and T. Beyer, "X-ray-based attenuation correction for positron emission tomography/computed tomography scanners." pp. 166-179.

[176] R. P. Woods, J. C. Mazziotta, and S. R. Cherry, "MRI-PET registration with automated algorithm," *Journal of computer assisted tomography,* vol. 17, no. 4, pp. 536-546, 1993.

[177] A. Ale, V. Ermolayev, E. Herzog, C. Cohrs, M. H. De Angelis, and V. Ntziachristos, "FMT-XCT: in vivo animal studies with hybrid fluorescence molecular tomography-X-ray computed tomography," *Nature methods,* vol. 9, no. 6, pp. 615-620, 2012.

[178] R. B. Schulz, A. Ale, A. Sarantopoulos, M. Freyer, E. Soehngen, M. Zientkowska, and V. Ntziachristos, "Hybrid system for simultaneous fluorescence and x-ray computed tomography," *IEEE transactions on medical imaging,* vol. 29, no. 2, pp. 465-473, 2010.

[179] J. Prakash, and P. K. Yalavarthy, "Data-resolution based optimal choice of minimum required measurements for image-guided diffuse optical tomography," *Optics letters,* vol. 38, no. 2, pp. 88-90, 2013.

[180] X. Ren, and J. Malik, "Learning a classification model for segmentation." p. 10.

[181] S. Ramani, Z. Liu, J. Rosen, J.-F. Nielsen, and J. A. Fessler, "Regularization parameter selection for nonlinear iterative image restoration and MRI reconstruction using GCV and SURE-based methods," *IEEE Transactions on Image Processing,* vol. 21, no. 8, pp. 3659-3672, 2012.

[182] L. Li, L. Zhu, C. Ma, L. Lin, J. Yao, L. Wang, K. Maslov, R. Zhang, W. Chen, J. Shi, and L. V. Wang, "Single-impulse Panoramic Photoacoustic Computed Tomography of Small-animal Whole-body Dynamics at High Spatiotemporal Resolution," *Nature biomedical engineering,* vol. 1, no. 5, pp. 0071, 2017.

[183] J. Jose, R. G. H. Willemink, W. Steenbergen, C. H. Slump, T. G. van Leeuwen, and S. Manohar, "Speed-of-sound compensated photoacoustic tomography for accurate imaging," *Medical Physics,* vol. 39, no. 12, pp. 7262-7271, 2012.

[184] T. P. Matthews, and M. A. Anastasio, "Joint reconstruction of the initial pressure and speed of sound distributions from combined photoacoustic and ultrasound tomography measurements," *Inverse problems,* vol. 33, no. 12, pp. 124002, 2017.

[185] J. Nebeker, and T. R. Nelson, "Imaging of Sound Speed Using Reflection Ultrasound Tomography," *Journal of Ultrasound in Medicine,* vol. 31, no. 9, pp. 1389-1404, 2012.

[186] M. Jaeger, G. Held, S. Peeters, S. Preisser, M. Grünig, and M. Frenz, "Computed Ultrasound Tomography in Echo Mode for Imaging Speed of Sound Using Pulse-Echo Sonography: Proof of Principle," *Ultrasound in Medicine & Biology,* vol. 41, no. 1, pp. 235-250, 2015/01/01/, 2015.

[187] R. G. M. Kolkman, W. Steenbergen, and T. G. v. Leeuwen, "Reflection mode photoacoustic measurement of speed of sound," *Optics Express,* vol. 15, no. 6, pp. 3291-3300, 2007/03/19, 2007.

[188] M. E. Anderson, and G. E. Trahey, "The direct estimation of sound speed using pulse–echo ultrasound," *The Journal of the Acoustical Society of America,* vol. 104, no. 5, pp. 3099-3106, 1998.

[189] S. J. Sanabria, and O. Goksel, "Hand-held sound-speed imaging based on ultrasound reflector delineation." pp. 568-576.

[190] H. Azhari, "Appendix A: typical acoustic properties of tissues," 2010.

[191] K. P. Murphy, *Machine learning: a probabilistic perspective*: MIT press, 2012.

[192] V. Pereyra, "Ray tracing methods for inverse problems," *Inverse Problems,* vol. 16, no. 6, pp. R1-R35, 2000/11/21, 2000.

[193] M. S. Hassouna, and A. A. Farag, "MultiStencils Fast Marching Methods: A Highly Accurate Solution to the Eikonal Equation on Cartesian Domains," *IEEE Transactions on Pattern Analysis and Machine Intelligence,* vol. 29, no. 9, pp. 1563-1574, 2007.

[194] S. Li, K. Mueller, M. Jackowski, D. P. Dione, and L. H. Staib, "Fast marching method to correct for refraction in ultrasound computed tomography." pp. 896-899.

[195] M. Sinha, and D. J. Buckley, "Acoustic properties of polymers," *Physical properties of polymers handbook*, pp. 1021-1031: Springer, 2007.

[196] J. Vigne, J. Thackeray, J. Essers, M. Makowski, Z. Varasteh, A. Curaj, A. Karlas, E. Canet-Soulas, W. Mulder, F. Kiessling, M. Schäfers, R. Botnar, M. Wildgruber, F. Hyafil, and I. on

behalf of the Cardiovascular study group of the European Society of Molecular, "Current and Emerging Preclinical Approaches for Imaging-Based Characterization of Atherosclerosis," *Molecular Imaging and Biology,* vol. 20, no. 6, pp. 869-887, 2018/12/01, 2018.

[197] I. Ivankovic, E. Merčep, C.-G. Schmedt, X. L. Deán-Ben, and D. Razansky, "Real-time Volumetric Assessment of the Human Carotid Artery: Handheld Multispectral Optoacoustic Tomography," *Radiology*, pp. 181325, 2019.

[198] M. Naghavi, P. Libby, E. Falk, S. W. Casscells, S. Litovsky, J. Rumberger, J. Badimon Juan, C. Stefanadis, P. Moreno, G. Pasterkamp, Z. Fayad, H. Stone Peter, S. Waxman, P. Raggi, M. Madjid, A. Zarrabi, A. Burke, C. Yuan, J. Fitzgerald Peter, S. Siscovick David, L. de Korte Chris, M. Aikawa, K. E. Juhani Airaksinen, G. Assmann, R. Becker Christoph, H. Chesebro James, A. Farb, S. Galis Zorina, C. Jackson, I.-K. Jang, W. Koenig, A. Lodder Robert, K. March, J. Demirovic, M. Navab, G. Priori Silvia, D. Rekhter Mark, R. Bahr, M. Grundy Scott, R. Mehran, A. Colombo, E. Boerwinkle, C. Ballantyne, W. Insull, S. Schwartz Robert, R. Vogel, W. Serruys Patrick, K. Hansson Goran, P. Faxon David, S. Kaul, H. Drexler, P. Greenland, E. Muller James, R. Virmani, M. Ridker Paul, P. Zipes Douglas, K. Shah Prediman, and T. Willerson James, "From Vulnerable Plaque to Vulnerable Patient," *Circulation,* vol. 108, no. 14, pp. 1664-1672, 2003/10/07, 2003.

[199] A. A. Friedman, A. Letai, D. E. Fisher, and K. T. Flaherty, "Precision medicine for cancer with next-generation functional diagnostics," *Nat Rev Cancer,* vol. 15, no. 12, pp. 747-56, Dec, 2015.

[200] J. Aguirre, M. Schwarz, N. Garzorz, M. Omar, A. Buehler, K. Eyerich, and V. Ntziachristos, "Precision assessment of label-free psoriasis biomarkers with ultra-broadband optoacoustic mesoscopy," *Nature Biomedical Engineering,* vol. 1, no. 5, pp. 0068, May, 2017.

[201] J. Aguirre, B. Hindelang, A. Berezhnoi, U. Darsow, F. Lauffer, K. Eyerich, T. Biedermann, and V. Ntziachristos, "Assessing nailfold microvascular structure with ultra-wideband raster-scan optoacoustic mesoscopy," *Photoacoustics,* vol. 10, pp. 31-37, Jun, 2018.

[202] V. Ntziachristos, "Going deeper than microscopy: the optical imaging frontier in biology," *Nature Methods,* vol. 7, no. 8, pp. 603-614, Aug, 2010.

[203] S. V. Ovsepian, I. Olefir, G. Westmeyer, D. Razansky, and V. Ntziachristos, "Pushing the Boundaries of Neuroimaging with Optoacoustics," *Neuron,* vol. 96, no. 5, pp. 966-988, 2017.

[204] A. Taruttis, and V. Ntziachristos, "Advances in real-time multispectral optoacoustic imaging and its applications," *Nature Photonics,* vol. 9, no. 4, pp. 219-227, Apr, 2015.

[205] A. A. Oraevsky, and A. A. Karabutov, *Ultimate sensitivity of time-resolved optoacoustic detection*, p.^pp. PWB: SPIE, 2000.

[206] J. Yao, and L. V. Wang, "Sensitivity of photoacoustic microscopy," *Photoacoustics,* vol. 2, no. 2, pp. 87-101, 2014/06/01/, 2014.

[207] A. M. Winkler, K. Maslov, and L. V. Wang, "Noise-equivalent sensitivity of photoacoustics," *Journal of biomedical optics,* vol. 18, no. 9, pp. 097003-097003, 2013.

[208] W. Jiang, R. Zhang, B. Jiang, and W. Cao, “Characterization of piezoelectric materials with large piezoelectric and electromechanical coupling coefficients,” *Ultrasonics,* vol. 41, no. 2, pp. 55-63, Mar, 2003.

[209] A. Safari, and E. K. Akdogan, *Piezoelectric and acoustic materials for transducer applications*: Springer Science & Business Media, 2008.

[210] X. Jian, Z. Han, P. Liu, J. Xu, Z. Li, P. Li, W. Shao, and Y. Cui, “A High Frequency Geometric Focusing Transducer Based on 1-3 Piezocomposite for Intravascular Ultrasound Imaging,” *Biomed Res Int,* vol. 2017, pp. 9327270, 2017.

[211] X. Jian, H. Zhile, X. Yongjia, L. Zhangjian, and C. Yaoyao, "Micromachined self-focusing piezoelectric composite ultrasonic transducer." pp. 2611-2614.

[212] C. Chao, V. Daeichin, D. Qing, G. v. Soest, G. Springeling, T. v. d. Steen, M. Pertijs, and N. d. Jong, "A single-cable PVDF transducer readout IC for intravascular photoacoustic imaging." pp. 1-4.

[213] V. Daeichin, C. Chen, Q. Ding, M. Wu, R. Beurskens, G. Springeling, E. Noothout, M. D. Verweij, K. W. van Dongen, J. G. Bosch, A. F. van der Steen, N. de Jong, M. Pertijs, and G. van Soest, “A Broadband Polyvinylidene Difluoride-Based Hydrophone with Integrated Readout Circuit for Intravascular Photoacoustic Imaging,” *Ultrasound Med Biol,* vol. 42, no. 5, pp. 1239-43, May, 2016.

[214] C. Chen, S. B. Raghunathan, Z. Yu, M. Shabanimotlagh, Z. Chen, Z. Y. Chang, S. Blaak, C. Prins, J. Ponte, E. Noothout, H. J. Vos, J. G. Bosch, M. D. Verweij, N. de Jong, and M. A. Pertijs, “A Prototype PZT Matrix Transducer With Low-Power Integrated Receive ASIC for 3-D Transesophageal Echocardiography,” *IEEE Trans Ultrason Ferroelectr Freq Control,* vol. 63, no. 1, pp. 47-59, Jan, 2016.

[215] G. Gurun, P. Hasler, and F. L. Degertekin, "A 1.5-mm diameter single-chip CMOS front-end system with transmit-receive capability for CMUT-on-CMOS forward-looking IVUS." pp. 478-481.

[216] D. Wildes, W. Lee, B. Haider, S. Cogan, K. Sundaresan, D. M. Mills, C. Yetter, P. H. Hart, C. R. Haun, M. Concepcion, J. Kirkhorn, and M. Bitoun, “4-D ICE: A 2-D Array Transducer With Integrated ASIC in a 10-Fr Catheter for Real-Time 3-D Intracardiac Echocardiography,” *IEEE Trans Ultrason Ferroelectr Freq Control,* vol. 63, no. 12, pp. 2159-2173, Dec, 2016.

[217] W. L. Melvin, “A stap overview,” *IEEE Aerospace and Electronic Systems Magazine,* vol. 19, no. 1, pp. 19-35, 2004.

[218] T. Misaridis, and J. A. Jensen, “Use of modulated excitation signals in medical ultrasound. Part II: Design and performance for medical imaging applications,” *IEEE transactions on ultrasonics, ferroelectrics, and frequency control,* vol. 52, no. 2, pp. 192-207, 2005.

[219] S. Telenkov, and A. Mandelis, “Signal-to-noise analysis of biomedical photoacoustic measurements in time and frequency domains,” *Review of Scientific Instruments,* vol. 81, no. 12, pp. 124901, 2010.

[220] J. Wang, and Y. Wang, “An Efficient Compensation Method for Limited-View Photoacoustic Imaging Reconstruction Based on Gerchberg–Papoulis Extrapolation,” *Applied Sciences,* vol. 7, no. 5, pp. 505, 2017.